EXTRUSION-BASED, THREE-DIMENSIONAL PRINTING OF CALCIUM-PHOSPHATE SCAFFOLDS

By

LUKASZ WITEK

Bachelor of Science in Biology
Temple University
Philadelphia, Pennsylvania
2008

Master of Science in Biomaterials and Biomimetics
New York University
New York, New York
2011

Submitted to the Faculty of the
Graduate College of the
Oklahoma State University
in partial fulfillment of
the requirements for
the Degree of
DOCTOR OF PHILOSOPHY
December, 2015

EXTRUSION-BASED, THREE-DIMENSIONAL

PRINTING OF CALCIUM-PHOSPHATE SCAFFOLDS

Dissertation Approved:

Dr. James E. Smay

Dissertation Adviser

Dr. R. Russell Rhinehart

Dr. Joshua D. Ramsey

Dr. Pankaj Sarin

Dr. Jay Hanan

ACKNOWLEDGMENT

First and foremost I would like to thank my advisor Dr. James Smay, for his guidance, patience, support, and advice throughout my time at Oklahoma State University, and back to my days at New York University (NYU). He set high standards and forced me to work and strive to do the best work possible. I enjoyed my time here in Stillwater, OK as well as the move over to a new department and facility in Tulsa, OK during my tenure as his Ph.D. student. I greatly appreciate all of his time and energy he has put into my course work and research, along with the countless hours of spending his free time explaining and mentoring me. I look forward to future collaborations not only with Dr. Smay, but his future students in his new position in the Materials Science and Engineering Department at Oklahoma State University-Tulsa.

Secondly, I would like to acknowledge the advice and guidance of my first advisor, Dr. Paulo G. Coelho, from New York University (NYU). During my time at NYU and OSU, he was always there to give advice, or extra input on work. Dr. Coelho has definitely been a major part of my graduate career, without him I do not think I would be where I am today, both as a person and professional. His selfless attitude and constant encouragement has helped me, finish two stints of graduate school. I am grateful for his presence not only as an advisor, colleague, but additionally as a close friend.

Additionally, I would like to thank Dr. Jousha Ramsey, Dr. Jay Hanan, Dr. Russell Rhinehart, and Dr. Pankaj Sarin for their advice, help, input, and effort. I want to express to them my gratitude for accepting to be part of this work and serving as members on my dissertation committee. Thank you all!

Finally, with as much gratitude that can be expressed in words and on paper, I would like to thank my parents (Lucyna and Tadeusz Witek), my brother (Thad), and my sister (Sylvia) for their support and constant inspiration and praise, not only during my time as a graduate student from New York until my time here at Oklahoma, but through my entire life. They have always been there for me, and supported all my endeavors, I know it wasn't easy, but dziękuje (Thank you).

Name: LUKASZ WITEK

Date of Degree: December, 2015

Title of Study: EXTRUSION-BASED, THREE-DIMENSIONAL PRINTING OF CALCIUM-PHOSPHATE SCAFFOLDS

Major Field: CHEMICAL ENGINEERING

Abstract: Small or large bone defects, can occur due to a variety of reasons: congenital disorders, infections, tumors, or traumas which can lead to significant disabilities. There is an assortment of bone grafting procedures, each having their own respective advantages and disadvantages and exhibiting certain essential characteristics. Among the available grafts, autogenous (autograft), allograft, xenograft, and alloplasts, all exhibit a minimum of two-thirds of the essential characteristics and have been proven useful in fully or partially repairing skeletal defects. However, different host-to-grafting material responses have been reported and should be taken into consideration when determining treatment options. A large range of physical and chemical properties can be achieved with calcium phosphate based materials, which possess two of the ideal characteristics for grafting procedures: osteoconduction and osseointegration. Calcium phosphate based scaffolds composed of hydroxyapatite (HA), β-tri-calcium phosphate (β-TCP), or a combination of both (HA/β-TCP) were investigated as materials for three-dimensional printing process to create layer-by-layer structures for use as bone regeneration scaffolds. Different calcium-phosphate phases will result in different degrees of *in vivo* dissolution and/or cell-mediated resorption. There has been a growing interest in BCP because it has been shown that this material improves the formation of new bone inside the implanted scaffold. The literature indicates that the faster dissolution rate of β-TCP would be greatly responsible of this enhancement. However, *in vitro* tests indicate that fast dissolution can decrease the mechanical strength of BCP scaffolds. Furthermore, studies reported that HA has higher mechanical strength and lower degradation rate than β-TCP. Therefore, the HA/β-TCP ratio is a key parameter controlling the performance of the scaffold for bone repair applications, since it determines degradation rate, calcium (Ca^{2+}) and phosphate (PO_4) release and mechanical properties of the material.

TABLE OF CONTENTS

TABLE OF FIGURES

INDEX OF TABLES

CHAPTER 1
INTRODUCTION

1.1 Overview

The motivation for this research was to advance a new technology, 3D printing of ceramics, to improve artificial bone scaffolds used in the repair of critical sized bone trauma or defects. When a healthy bone is simply fractured, immobilizing with a cast allows the osteocytes to naturally mend the fracture. However, when trauma, bone loss, or disease destroys a large section of bone, one must consider technologies that serve the triple purpose of supporting mechanical load, providing a physical scaffold for rapid and long-term bone formation and gracefully dissolving over time to allow natural bone to resume its function. 3D printing of ceramics offers significant fabrication advantages over the traditional forming techniques in that spatial variation of composition can now be controlled at a length-scale commensurate with the bone cell microenvironment.

The human skeleton is a complex, living structure and bone wound healing is understood to include reconstruction of a collagen-mineral nanocomposite, porous, vascularized, spatially varied, hierarchical structure; the main work being done by osteoblasts, osteoclasts and chondrocytes, and the circulatory system. For small bone defects (i.e., sub-critical) simple bone graft substitutes such as porous ceramic sponge materials with poor mechanical strength can significantly speed the bone repair process by providing a structure on which mesenchymal cells can operate. For critical and super-critical defects (i.e., those where the osteyocytes will not heal the wound), there is a need to provide a scaffold that rapidly directs osteyocyte activity across the wound and begins the healing process. The future of bone grafting will be a combination of materials, which have specific desirable properties (i.e. dissolution kinetics, pore size, surface area) and thus will compensate for the disadvantages of each separate material.

This dissertation summarizes efforts to, design, fabricate, and characterize biphasic calcium phosphate (BCP) scaffolds for inducing bone regeneration across critical defects using a direct-write (DW), colloidal gel extrusion process. A biphasic ceramic mixture consisting of hydroxyapatite (HA) and beta-tricalcium phosphate (β-TCP) was investigated for this research project. The three main research questions were:

- *Is the composition and spatial distribution of the materials in the sintered ceramic scaffold able to be controlled?*

  Synthetic HA and β-TCP are bone substitute materials approved by the United States Food and Drug Administration (FDA). Implant manufacturers typically use these ceramics to make a porous scaffold by casting and sintering processes. In addition to poor strength of scaffolds fabricated in this way, the implant manufacturer often faces the dilemma of choosing HA, which is virtually insoluble or β-TCP, which is too soluble. Legeros et al, addressed the solubility issue by synthesizing so-called bi-phasic calcium phosphate (BCP) by simply blending and co-sintering powders of HA and β-TCP. The BCP has intermediate solubility; however, the impact of secondary phases, such as calcium pyrophosphate ($Ca_2P_2O_7$), on solubility has not been fully understood. In the new aqueous processing method studied here, the question of retaining the chemistry of the input ceramics in the final fabricated implant is important for understanding if the scaffold can be fabricated with the desired intermediate solubility.

- *Do the details of printing (i.e., pre-mixed composition ink, two-tip deposition of different ink compositions or blending inks with a mixing chamber while printing) affect the in vitro response of the scaffold on the macroscopic scal*e?

  Here, the term "ink" refers to the colloidal gel that is synthesized by dispersing and then controllably flocculating, high-concentration, aqueous ceramic slurries to create pseudo-plastic with yield stress rheology suitable for 3D printing. The ink composition can be controlled by pre-selecting the composition (i.e., ratio of HA to β-TCP) in the dispersing step of the colloidal slurry synthesis or by controlling the deposition of separate HA and β-TCP inks from independent reservoirs. Two-tip printing can create a binary OR filament (i.e., HA/β-TCP), while the mixing chamber method creates a binary AND filament (i.e., HA & β-TCP). The mixing chamber method has the further advantage of controlling the HA:β-TCP ratio in the filament by simply controlling the flow rate of each stream. This research question explores the effects of the printing process on dissolution and ion release behavior of scaffolds fabricate by these different methods.

- *Can 3D printing be used to tailor the scaffold to induce bone healing in long-bone defects, in addition to control of dissolution kinetics?*

  Long cylindrical shaped scaffolds have been successfully fabricated and tested in vivo. Although these scaffolds were successful, they were only done on a uniform

material composition throughout scaffold (i.e. 100% HA, 100% β-TCP, or some ratio of HA/β-TCP). With improved tools/methods such as two-tip or mixing chambers, 3D printing will allow for further tailoring of the scaffold. In this case, one can tailor the cylindrical scaffold varying composition as a function of the radius, with having the more soluble material (β-TCP) concentrated on the inner radius and grading out to the outside shell composed of the slower resorbing 100% HA. This may be ideal for the long bone design parameter or in a case where initial mechanical properties are desired as well as allowing for better control of dissolution/resorption.

1.2 Project Overview

The dissertation is divided into the following main areas of work: (a) beneficiation and characterization of commercial HA and β-TCP and synthesis of the colloidal gel ink with compositions of (i) 100% HA, (ii) 100% β-TCP, (iii) 15/85% HA/β-TCP, and (iv) 15/85% HA/β-TCP (design mix), to verify their chemical properties and *in vitro* responses, (b) design the individual scaffolds in a innovative way (interchanging material on micro-scale level or create functionally graded structure to control their respective dissolution kinetics), (c) qualitatively investigate the Ca^{2+} and PO_4 release in the initial implantation (via *in vitro*) times to better understand the kinetics to further incorporate into design process, and (d) ultimately creating a novel cylindrical scaffold for long bone regeneration.

1.3 Dissertation Scope

The dissertation is organized into six chapters: Chapter 1 states the overview and main thesis of this project and its work. Chapter 2 is a review of literature pertinent to bone repair techniques and materials with specific emphasis on the allograph approach (i.e., using artificial bone scaffolds to aid bone repair). Chapter 3 addresses the first research question regarding ink formulation and observation of the printed scaffold quality in light of process variables. Chapter 4 addresses the second research question regarding the agile placement of HA, HA/β-TCP, or β-TCP within a functionally graded scaffold by way of multiple deposition nozzles or an active mixing chamber. Chapter 5 focuses on the third research question regarding how functionally graded long bone scaffolds in an in vitro environment behave and the subsequent qualitative analysis of the scaffolds. Chapters 3, 4, and 5 all are organized to give a brief introduction, experimental section, results, discussion and conclusion. Chapter 6 is the summarization from the entire work with its conclusions and additionally states a few recommendations for future work. Chapter 7 provides a list of references for this document.

CHAPTER 2
REVIEW OF LITERATURE

2.1 Bone

2.1.1 Introduction

Bone, composed primarily (Table 2.1) of osseous tissue, is a dynamic living organ, which is a complex, porous bio-composite that creates an environment for osteogenesis, osteolysis, hematopoiesis, while serving as a calcium reservoir for the body [1].

• Collagen, mainly Type I
• Hydroxyapatite
• Non-collagenous proteins
• Proteoglycans
• Water
• Blood vessels
• Lymphatic vessels
• Nerve Tissue

Table 2.1: Primary components of the make up of bone.

Bone is not a uniformly solid material, but organized according to location and function in the overall structure. Some medical terms to refer to sections of bone will serve us in this literature review are listed and briefly described in (Table 2.2). Broadly, bone can be classified into two types: cancellous and cortical (Table 2.3). Cancellous bone is also called spongy or trabecular bone due to the high porosity. For example, in a cross sectional view of a limb bone, one observes a marrow space surrounded by cancellous bone composed of 50-90% volume porosity, and spongy in composition. Surrounding the cancellous bone is cortical bone compromises the outer layer, which is more dense and contains c.a. 10% porosity by volume [2]. Regardless of the bone type, cancellous or cortical, both undergo some extent of differentiation, remodeling, and resportion, which are controlled by various interactions between cells: osteocyte, osteoblast, and osteoclast [3, 4]. The intricate design of bone is further composed of trabeculae,

which range from 130 - 350 μm in diameter; the open porosity provides a route for vascularization and nutrient flow.

Term	Definition
Superior (Cranial)	Toward the head end or upper part of the structure or body; above
Inferior (Caudal)	Away from the head end or toward the lower part of a structure or the body; below
Ventral (Anterior)	Toward or at the front of the body; in front of
Dorsal (Posterior)	Toward or at the back of the body; behind
Medial	Toward or at the midline of the body; or the inner side
Lateral	Away from the midline of the body; or the outer side of
Intermediate	Between a more medial and more lateral structure
Proximal	Closer to the origin of the body part or the point of attachment of a limb to the body trunk
Distal	Farther from the origin of a body part or the point of attachment to the body trunk
Superficial (External)	Toward or at the body surface
Deep (Internal)	Away from the body surface; more internal

Table 2.2: Orientation and directional terms commonly used in the medical field.

- Cortical Bone = Compact Bone (80%)
    - Osteon
        - Type I collagen, very organized, longitudinal
        - Mineral deposits, hydroxyapatite
        - Very dense and strong, reinforced concrete
- Cancellous Bone = Spongy Bone (20%)
        - Type I Collagen, less organized
        - Mineral deposits, hydroxyapatite
        - Less strong, more forgiving, shock absorber

Table 2.3: Summary of the two primary bone types.

Cells with a single nucleus, osteoblasts, are responsible for bone formation, these cells are differentiated and derived from mesenchymal stem cells. These cells produce a mineralized osteoid, which is composed mainly of Type I collagen. These osteoblasts are metabolically active cells that express soluble signaling factors such as bone morphogenetic proteins (BMPs), platelet-derived growth factor (PDGF), transforming growth factor (TGF) or insulin-like growth factors

(IGFs) [5]. Osteoblasts trapped in the secreted mineralized matrix, either differentiate into osteocytes or result in apoptosis. Osteocytes are networked together with long cytoplasmic extensions called canaliculi that occupy tiny canals in bone, which are used to connect the lacuna. In addition, osteocyte metabolic activity is important to maintain bone viability and homeostasis [5]. While the osteoclast is a large multinucleated cell associated with removal of bone (often referred to as bone resorption) [6]. Bone remodeling process involves osteoblasts (form bone) and osteoclasts (re-absorb bone), are in control of new bone formation and resorption of the old bone, respectively. While bone is a resilient vital organ of the body, which due to the presence of both the osteoblasts and osteoclasts are two of the many factors in maintaining healthy bones [7], also the reason it has a great self-healing abilities with respect to small scales/length spans. However, trauma to the skeletal system due to: accident, osteoporosis, surgical removal of tumors or other diseases often overwhelm the ability of bone to self-heal at which an external intervention is necessary to facilitate the bone healing process [8, 9].

2.1.2 Bone Defects and Abnormalities

Bone defects, whether large or small, occur due because of congenital disorders infections, tumors, or traumas [10]. For instance, more than 2000 people are diagnosed with a bone tumor each year in the United States, while approximately 1 million skeletal defects are observed worldwide [11]. Irrespective of bone loss defect, an ideal rehabilitation would be full tissue regeneration; however, depending on location and size of the defect, full tissue regeneration may not be achievable [12]. While it is estimated that more than half a million bone-grafting procedures are performed annually in the United States alone, these numbers double on a world wide basis and indicating a shortage in the availability of musculoskeletal donor tissue traditionally used in these reconstructions (Figure 2.1).

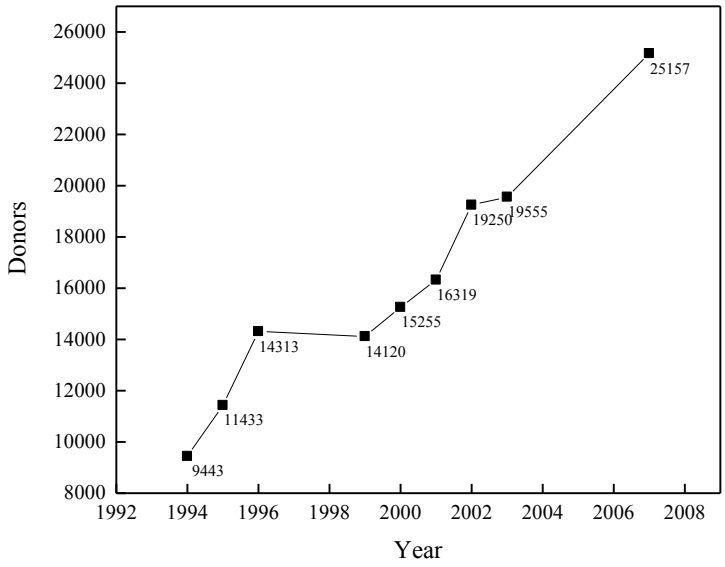

Figure 2.1: U.S. trends in musculoskeletal tissue donors (Source: AATB Annual Survey).

Trauma is a major contributing factor for large bone defects/fractures. The leading causes of the majority blunt force trauma are automobile accidents, while others can be caused by work related accidents, recreational activities, or a simple fall [10]. Trauma may result in fractures with varied morphology and complexity degrees (Figure 2.2), ultimately requiring varied treatment approaches. A fracture can heal naturally or with the help of supplemental procedures, as each patient will have a different response to a bone fracture. For example, a young patient who is still in the process of growing will probably have fewer complications to repair/heal a fracture compared to an older individual as ones bone modeling/remodeling kinetics or quantity may have changed due to the aging process.

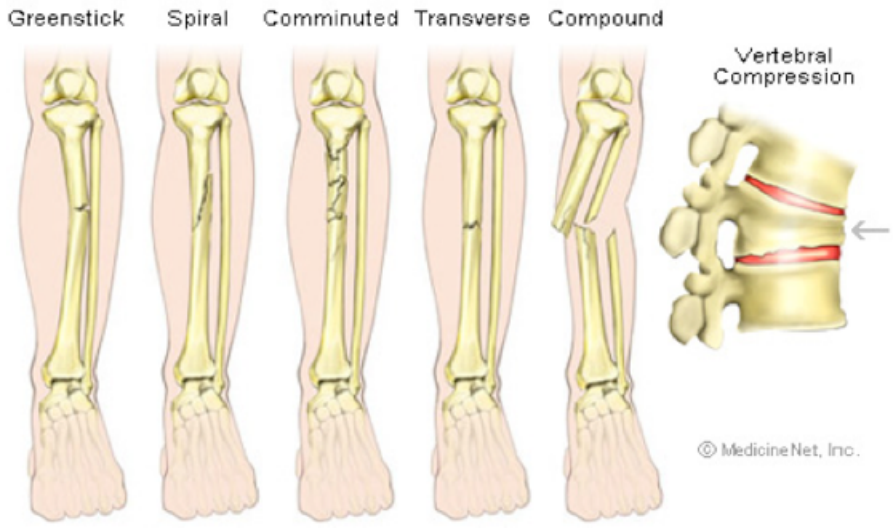

Figure 2.2: Schematic representation of various bone fractures of human tibia and spinal cord [13].

Different treatment options are currently available such as autografts and allografts. These options have proven successful but at times have their own respective limitations and drawbacks such as second surgical site or infection and viral transmission, respectively, hence focusing on a bone tissue engineering method to fabricate and/or regenerate bone, which in turn would restore and maintain its function [2, 11]. Scaffolds, which are three-dimensional (3D) biocompatible structures, are a pivotal element in bone tissue engineering. These scaffolds have the ability to mimic extracellular matrix (ECM) properties such as mechanical support, cellular activity, and protein production while simultaneously providing a guide for cell adhesion and stimulation for bone tissue formation *in vivo* [11].

Structurally, primary bone formation, or direct formation of new bone from damaged bone, without a cartilaginous intermediate (as in the endochondral bone formation seen in embryology and long bone fractures) is what is observed to grow into most scaffolds, and is the type of bone formation which is trying to be controlled. This type of bone ingrowth into a defect or wound site occurs as directional growth of new immature trabeculae, from the endosteal or periosteal layers of damaged cortical and cancellous bone into the wound site. When an appropriate scaffold is present, these new trabeculae, as part of a phenomenon described as osteoconduction, will attach to and follow along the mesostructural elements of the scaffold. This will only occur if the scaffold has suitable surface chemistry and microtexture. Hydroxyapatite scaffolds, used in various forms such as packed synthetic particles, processed bone, or processed coral skeletons, have consistently had the proper surface chemistry and microstructure to show strong bone conduction.

2.2 Graft Materials

Among the available grafts, autologous (autograft), allograft, xenograft, and alloplastic, all exhibit the essential characteristics and have been proven useful in fully or partially repairing skeletal defects. However, different host-to-grafting material responses have been reported and should be taken into consideration while determining treatment options.

2.2.1 Natural grafting materials

There is an assortment of natural bone grafting procedures, each having their own advantages and disadvantages. Bone grafts should at least have these essential characteristics: osteoconduction - the capability to support the growth of bone over its surface; osteogenesis - the process of extra cellular matrix deposition and subsequent minerializtion by osteoblasts,and osseointegration - the ability to intimately interact with bone without an extra layer of soft tissue.

The autologous graft is the only one that is osteoinductive and provides the highest biocompatibility with the host compared to other grafting treatment options since it comes from the same patient. A disadvantage in this procedure is that it requires at least two operating sites, lengthening surgical time and is often associated with moderate levels of pain for the patient [14-16]. The autologous graft is often considered the "gold standard" for bone defect rehabilitation [11, 15]. Additionally, many patients may suffer from osteoporosis, weakened immune systems, etc. and autologous grafting is not a viable option.

Allografting is similar to the autograft method but it is harvested from a cadaver. The allograft has the same distinctiveness as the autograft with the omission of osteogenic cells [16]. Allograft includes advantages such as availability and avoidance of a second morbidity site [10, 16]. However, disadvantages of the allograft include but are not limited to fracture, non-union, infection, and viral transmission, which could possibly lead to lower degrees of biocompatibility and treatment success [14, 16].

Another type of grafting is the xenograft, which is taken from species other than human (in most cases of bovine origin). Concerns related to this type of grafting include disease transmission between the animal and patient [14].

2.2.2 Synthetic grafting materials

Another grafting material group comprises of synthetic materials. These grafts are/can be typically composed of a variety of materials such as polymers, metals, bioactive glasses, and bioactive ceramics such as hydroxyapatite (HA) and β tri-calcium phosphate (β-TCP), or a combination/mixture of materials [16]. As expected, each of these synthetic grafts has specific advantages and disadvantages.

Polymers have been used as scaffolds for bone defect regeneration. Polymers like collagen, fibrin, chitosan, and starch, which are natural biodegradable polymers, have been shown to present acceptable biocompatibility but minimal osteoconductive properties [15]. These types of scaffolds have been widely used because of their versatility, as process dependent physicochemical properties ranging in size and shape and degradation rates which can be controlled [11]. The benefit of degradable implants is the fact that they eliminate an extra surgical procedure for device removal and allow for a slow transfer of the load to the healing bone [17]. However, a major disadvantage polymer-based scaffolds is their low mechanical stability [15, 18], rationalizing the utilization of other classes of materials in load bearing skeletal defects.

Metals have also been utilized as an alternative solution to skeletal defects. While metals provide instant mechanical strength at the defect site, they generally show poor integration with the tissue at the implant location (exceptions include Ti-based alloys among others) [11]. Metals have also been shown to fail due to infections or eventually fatigue loading [11]. Along with all of the disadvantages, metals do not show any resorption and from a biomechanical perspective often times lead to bone resorption due to stress shielding. Thus, a limitation in the temporal physicochemical properties of polymer and metal-based materials has led to a large number of investigations on ceramic-based materials.

Since the type of bonding at the material–bone interface depends on the nature of the material the interfacial strength between bone and implant material, is determined from push-out tests, it has been determined to be higher for the bioactive implant materials compared to materials such as titanium, zirconia or alumina (Table 2.4). With respect to bioactive materials, fractures occur either within the material or bone but not at the interface; however with inert materials, the separation occurs at the interface. This feature is attributed to the “bonding osteogenesis” occurring at the interface between bone and the bioactive materials, which is not present within non-bioactive materials. This interface has been referred to as the “bonding zone”, described as being electron dense, having a mineralized organic structure.

Materials	Fracture Strength	Bone Contact	Fracture
Bioglass®*	28.9 MPa	92.9%	Cohesive
Hydroxyapatite*	19.6 MPa	95.4%	Cohesive
Titanium**	1.9 MPa	59.5%	Interfacial
Zirconia**	1.3 MPa	33.3%	Interfacial

*Strengths per unit area after 24 weeks; *Bioactive; **Non-bioactive*

Table 2.4: Comparative Properties of Biomaterials [19].

Therefore a large range of physical and chemical properties can be achieved with ceramic-based materials. For instance, introduced in the early 70's, bioactive glasses present osteoconductive properties along with rapid *in vivo* dissolution rates [16, 20]. These materials have been used as pre-formed implants and have shown considerably greater mechanical strength in comparison to other bioceramics used for grafting purposes (Table 2.5) [16]. However, their utilization fell from favor compared to other materials, as bioactive glasses do not always attach to the skeleton and their low resistance to drilling and shaping due to their brittle nature [11, 16]. Alternative to bioglasses, calcium phosphate (CaP) based bioceramics possess two of the ideal characteristics for grafting procedures: (1) osteoconduction and (2) osseointegration [16].

	Cancellous bone	Cortical bone	HA	Bioglass	A/W glass ceramic	Bioglass PS modified
Bioactivity (A)	13	13	3.0	13	6.0	13
Fracture Toughness K1c (B)	0.1	6.0	1.0	0.6	2.0	1.2
Elastic Modulus GPa (C)	1.0	15	85	35	118	5.0
Tensile Strength MPa (D)	3.0	151	80	42	215	103
Quality Index = (A×B×D)/C	4.0	500	3.0	9.0	20	303

HA, hydroxyapatite; A/W, apatite-wollastonite; PS, polysulfone.

Strength MPa	Cancellous bone	Coralline POP	POP	Porous HA	PMMA	Porous alumina ceramic	Bioglass	A/W glass ceramic	Bioglass PS modified	Cortical bone
Compressive	5.5	9.3	23	55	60	90	-	-	-	162
Tensile	3.0	2.8	4.1	2.5	6.9	15	42	215	103	151

HA, hydroxyapatite; POP, plaster of paris; PMMA, polymethacrylate; A/W, apatite-wollastonite; PS, polysulfone.

Table 2.5: The table compares the properties of synthetic grafting materials to cancellous and cortical bone in addition to giving information on other materials being used currently for tissue regeneration [11, 16].

2.2.2.1 Calcium Phosphates

Calcium phosphate (CaP) consists of minerals that contain calcium (Ca^{2+}) combined with phosphate group (PO_4^{3-}) (Table 2.6). Calcium found in bovine milk and blood is primarily constituted from calcium phosphate. Two of the primary CaP groups make up our bioceramics which will be focused on stoichiometric (1) hydroxyapatite (HA), $Ca_{10}(PO_4)_6(OH)_6$ which is also the principle mineral component of bone and (2) tri-calcium phosphate (TCP), $Ca_3(PO_4)_2$, which occurs in alpha (α) and beta (β) phases. Hydroxyapatite accounts for almost seventy percent of

bone and nearly ninety percent of tooth enamel. The Ca to P ratio of bone ranges from approximately 1 to 1.67, while HA and TCP have ratios of 1.67 and 1.5, respectively. In terms of dissolution among the CaP groups each have their own respective solubility and their rate of dissolution with respect to Ca is in the order of TTCP>α-TCP> β-TCP>HA. While regarding dissolution of the phosphate the order was as follows: α-TCP>β-TCP>HA.

Until recently, pure hydroxyapatite has been used as a graft primarily that it has outstanding osteoconductive properties in addition to chemical composition comparable to the inorganic component of bone [9, 21]. The advantage of HA is its high initial compressive strength while a disadvantage is its low dissolution kinetics *in vivo* (with rates of 1-2% per year or no evidence of change after more than five years of implantation) [10, 16]. Hydroxyapatite with a solubility product (K_{sp}) of ~$2.4x10^{-59}$ mol/kg resorbs slowly under physiological conditions due to its biochemical stability, it will slowly remodel when placed in a bony area

As a result of the slow degradation rates of HA, β-TCP ceramics were developed [22]. While it has been shown that β-TCP (K_{sp}=$2.8x10^{-30}$ mol/kg) goes through resorption over a 6 to 18 month period, it can be argued that it may have too rapid of a biodegradation/dissolution [16, 22]. Therefore, numerous research projects have attempted blending HA and β-TCP in various ratios, coining the new product a biphasic calcium phosphate (BCP) in order to better control the bioactive ceramic material degradation/dissolution properties [10].

HA and β-TCP are both biocompatible and bioactive. They each possess the excellent properties of a nontoxic, biocompatible, osteoconductive, bioactive, nonimmunogenic agent while having the ability to form a direct chemical bond with living tissue [23]. These particular CaP bioceramics are bioactive (directly bonding with bone) and osteoconductive, but innately not osteoinductive, ability to form bone in non-bony sites, although there have been instance reported of this happening for both the HA and β-TCP [24, 25]. Specifically sintered HA is very important not only for tooth root replacement, bone reparation, augmentation of alveolar ridges and maxillofacial reconstruction [26]. In the past researchers have pointed out that the trend in the bioceramic field will be focused on solving the limitations of CaP materials, specifically HA and β-TCP ceramics, to improve their biological properties and applications [27]. Due to their well-researched and studied properties, both are approved as biomaterials by the USFDA. Various products that contain either HA, β-TCP, or a combination of both are readily found on the market in various forms.

2.2.2.2 Biphasic Calcium Phosphate

The preparation of BCP ceramics which was described in 1986 by R. LeGeros consists of a ratio mixture of HA and β-TCP [28]. The sintering of the mixture is carried out at temperature where the diffusion of Ca from rich to poor regions is slow and the two phases remain distinct. The *in vivo* properties of the BCP ceramic were characterized by G. Daculsi, and colleagues [29, 30]. According to these studies, BCPs as biomaterials have controlled dissolution, and due to the material's chemical composition, the bone ingrowth is done at the expense of ceramic. BCPs are obtained when a quantity of biological calcium deficient apatite is sintered at temperatures above 700°C. The BCPs' reactivity is determined by the HA/β-TCP ratio: the lower the ratio the higher the reactivity [31]. Degradation and resportion along with its respective mechanical/physiological properties will be dependent on ratio of HA/β-TCP, the higher the amount of HA the lower the dissolution. As HA ratio decreases, the BCP ceramic will have more bone bonding, β-TCP will resorb facilitating bone formation. The BCP materials *in vitro* and *in vivo* have the ability to produce responses from bone cells that are the same as bone material: cell attachment and proliferation [32].

Irrespective of the ratio of HA to β-TCP, the bone to tissue reaction proceeds in a similar healing pattern, which is observed in the typical fracture healing. In this process, first is the formation of the hematoma, followed by inflammation, vascularization, resorption of osteoclasts and ultimately new bone formation. This is a natural occurring process in bone, therefore permitting the bone remodeling process [33].

Name and Chemical Formula	Abbreviation	Structural characteristics (unit-cell dimensions in angstrom(Å))	Density (g/cm^3)
β-tricalcium phosphate ($Ca_3(PO_4)_2$)	β-TCP	Trigonal R3c[a] <u>a</u> = 10.439; <u>b</u> 37.375	3.07
α-tricalcium phosphate ($Ca_3(PO_4)_2$)	α-TCP	Monoclinic $P2_1/a$ <u>a</u> = 12.887; <u>b</u> = 27.280; <u>c</u> = 15.219; β = 126.20	2.86
Tetracalcium phosphate ($Ca_3(PO_4)_2O$)	TTCP	Monoclinic $P2_1$ <u>a</u> = 7.023; <u>b</u> = 11.986; <u>c</u> = 9.473; β = 90,90	3.05
Phospho-calcium hydroxyapatite ($Ca_{10}(PO_4)_6(OH)_6$)	HA	Hexagonal $P6_3/m$[c] <u>a</u> = 9.418; <u>b</u> 6.881	3.16

Table 2.6: Main calcium phosphate compounds. [a]Hexagonal settings, [c]The structure of pure HA at room temperature is monoclinic, while in biomaterials the hexagonal form is primarily seen [34, 35].

Composition (wt%)	Enamel	Dentin	Bone	HA	β-TCP
Calcium	36.5	35.1	34.8	39.6	38.8
Phosphorus	17.7	16.9	15.2	18.5	19.9
Ca/P (molar ratio)	1.63	1.61	1.71	1.67	1.5
Sodium	0.50	0.60	0.9	-	-
Magnesium	0.44	1.23	0.72	-	-
Potassium	0.08	0.05	0.03	-	-
Carbonate (CO_3^{2-})	3.5	4.6	7.4	-	-
Fluoride	0.01	0.06	0.03	-	-
Chloride	0.30	0.01	0.13	-	-
Crystallographic properties: lattice parameters					
a-axis (Å)	9.441	9.421	9.410	9.430	10.439
c-axis (Å)	6.880	6.887	6.890	6.981	34.375

Table 2.7: Concentration of the inorganic components of enamel, dentin, bone, and stoichiometric HA and β-TCP [36]. The lattice parameters are the mean ±0.003Å.

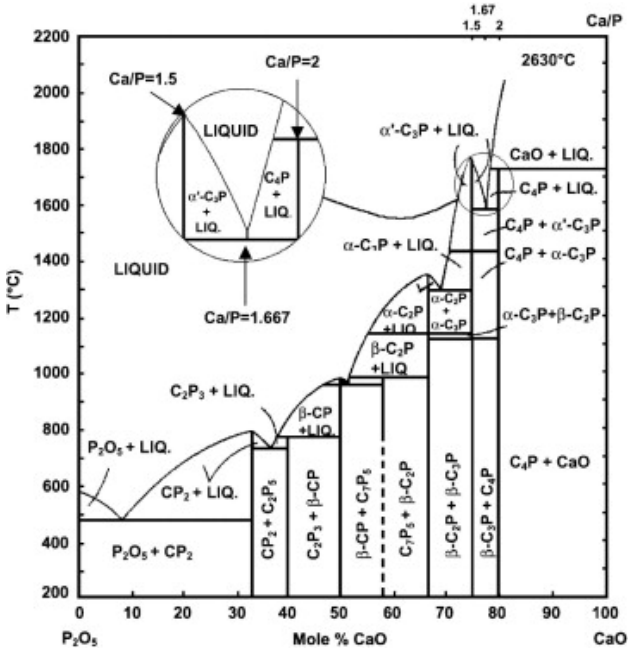

Figure 2.3: Partial calcium oxide phosphorus pentoxide (CaO – P_2O_5) phase diagram [37-39].

2.3 Scaffold Fabrication Technology

Due to recent improvements in bioactive ceramics processing as well as their structure-property relationship, a substantial increase in their utilization has been observed over the last decade [15].

Numerous techniques have been developed for the production of bioactive ceramics for tissue engineering and bone grafts [40]. However, these fabrication technologies had limitations as to the material composition and achievable physical dimensions [40]. Among the first techniques were fiber bonding, solvent casting, and melt molding [11, 41]. However, complex designs/geometries could not be created using these standard-manufacturing procedures.

2.3.1 Conventional Scaffold Fabrication Techniques

Currently there are various fabrication techniques to assemble porous scaffolds, with some of the most common ones being: electrospin casting, foam-gel technique, particulate leaching, emulsion freeze drying, thermal phase separation, fiber bonding, membrane lamination, melt molding, fused deposition modeling (FDM), and solid freeform fabrication (SFF) [41-46]. Each technique has its own limitations such as but not limited to poor meso-pore size control, limited structure composition design capabilities, and uncertain pore interconnectivity to name a few.

For example FDM assembles three-dimensional (3D) models by extrusion, patterning, and solidification of a molten polymeric filament. The deposition speeds are fairly slow and 3D pore architecture is difficult to control. Furthermore the large polymer content quantity requires extended binder burnout steps especially when producing structures composed of ceramic oxide. While another considerable disadvantage of FDM is the fact the process requires high operating temperatures. Thus the fabrication of certain biological materials is impeded [17, 47-49].

While stereolithography is not suitable for use with sensitive materials, such as growth factors, due to the use of UV laser to crosslink the scaffold, it is still feasible to fabricate a ceramic scaffold [50]. Although it requires an extra step, such as making a mold from a polymer, making a ‘negative’, with this extra step, not only is that a factor but also extra cost, time, and reproducibility. Aside from the cost and extra step, the reproducibility and resolution, makes this method undesirable.

2.3.2 Three-dimensional printing - Direct Write (DW) - Robocasting

In an attempt to improve on processing and design, the utilization of computer-aided programs for materials design has gained popularity. From computer-aided design (CAD) and computer-aided manufacturing (CAM), technological advancements of 3D-printing in the form of robocasting. Among different 3D production methods, ‘robocasting’ allows for the building of

ceramic-based scaffolds without the need for a mold. Direct-write or robocasting is grouped as a SFF method, which utilizes a colloidal gel to fabricate an intricate 3D structure through deposition without the need for a cast or mold [37, 38, 51, 52]. According to the ink flow behavior, direct-write (DW) techniques can be categorized into two different categories: (1) droplet-based, and (2) filament-based ink approach [53]. In droplet-based, the ink is delivered in the form of droplets to fabricate a 3D structure while the filament-based direct-write technique is favorable due to their material flexibility, low cost, and capability for self-supporting features [54-57]. The filament-based technique allows for the creating of advanced composites with the utilization of single or multi-material colloidal gels. It has shown to be a useful tool for tissue engineering to fabricate bone scaffolds for bone regeneration.

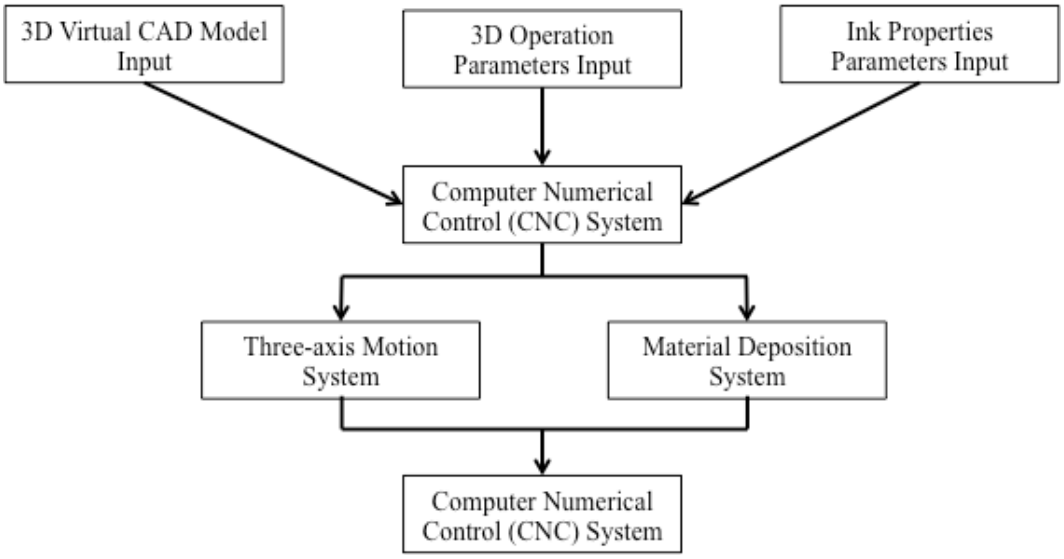

Figure 2.4: Flow diagram representing the DW process based on filament extrusion technique [53].

The flow diagram of filament-based direct-write procedure for SFF of 3D structures is presented in Figure 2.4. First, 3D virtual structures are generated through computer aided design (CAD) model tools. Then, the operation parameters, such as deposition speed, applied pressure, nozzle diameter, and spacing height, should be specified. Next, process relevant ink properties, like material types and composition, should be determined. The computer numerical control (CNC) software processes the designed CAD model, operation conditions and ink properties, and conveys them to three-axis motion system and ink delivery system simultaneously. Three-axis motion system controls the accurate tool path for the deposition process. The ink delivery system supplies appropriate volumetric flow rate of inks along the tool-path lines. Based on the cooperation of these two systems, the real 3D structures can be created.

The ink delivery system is the most important component in the whole filament-based DW process. It depends on the ink properties, and desired 3D structures and determines the quality of the final products. It commonly consists of three components, propeller, reservoir, and deposition head. The feedstock colloidal gels are stored in reservoirs; the displacement part extrudes inks through a deposition head at desired volumetric flow rate (Figure 2.5). For example, in robocasting, the plunger can be mechanically displaced on the ink reservoir at the constant speed to drive the ink out of the nozzle. Figure 2.6 illustrates the schematics of the robocasting machine and multi-nozzle arrays for parallel printing of discrete ink materials and mixing nozzle system for multi-material mixture printing [52, 58].

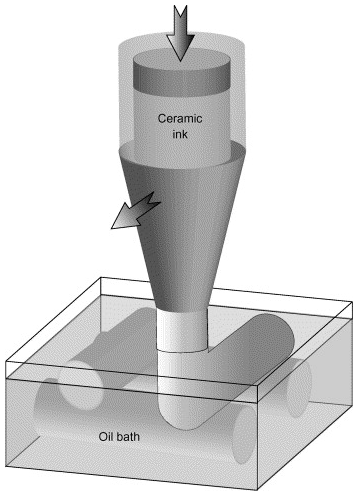

Figure 2.5: Schematic of robocasting fabrication process (Dimensions not to scale). The ceramic part is built layer-by-layer from a computer design. A three-axis robotic arm moves the injection syringe while pressing the ceramic ink through the conical deposition nozzles, immersed in an oil bath, to create a self-supporting 3-D network [38].

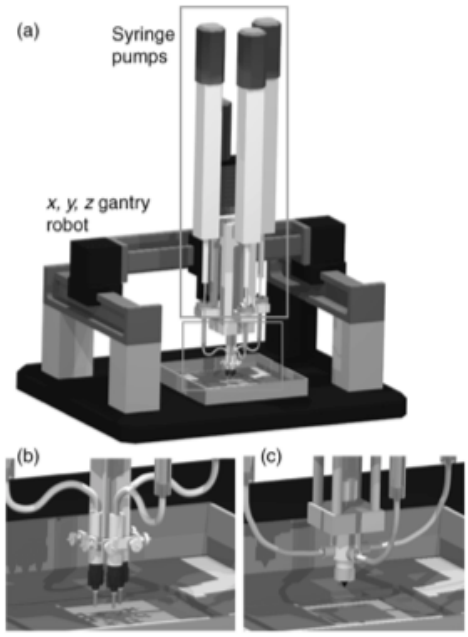

Figure 2.6: Representation of the robocasting machine used for the fabrication of scaffolds (a) represents the entire gantry and setup of robocasting machine, (b) representation of a multi-tip arrangement so allow for permitting with various materials, and (c) image of mixing nozzle attached to mixing motor and chamber [52].

Even though DW techniques have indicated their potential advantages allowing the ability to 'print' a variety of designs (Figure 2.7), there are still some challenges. Firstly, the challenges in identifying new ink materials and their potential functions. Further advances require science-based ink design method, instead of empirically formulating new inks by trial and error adjustments of inks composition. Secondly the machine requires manufacturing precise and quality parts using these materials. Ultimately with respect to the DW scaffolds the shape and/or deformation of structures during deposition, drying, and sintering is another important area to pay keen attention to, to further advance this technology. Lastly is to how to apply these techniques from prototyping to large-scale production, and to shorten production time and lower cost for these parts [53].

In summary, for the robocasting process the following criteria, with respect to the colloidal gel, must be satisfied to successfully fabricate a scaffold [59]:

1) The mixture must be homogenously mixed because the presence of agglomerates may lead to clogging, especially when working with smaller diameter tips.

2) The colloidal gels should be extruded through 100 – 500 μm diameter nozzle, while avoiding filter pressing as this would change the solids loading content and in turn have a negative affect on the shrinkage.

3) The colloidal gel should have the ability to retain its shape as extruded, cylindrical, along with the ability to have shape retention once new lines are printed on top of each other in the subsequent layers.

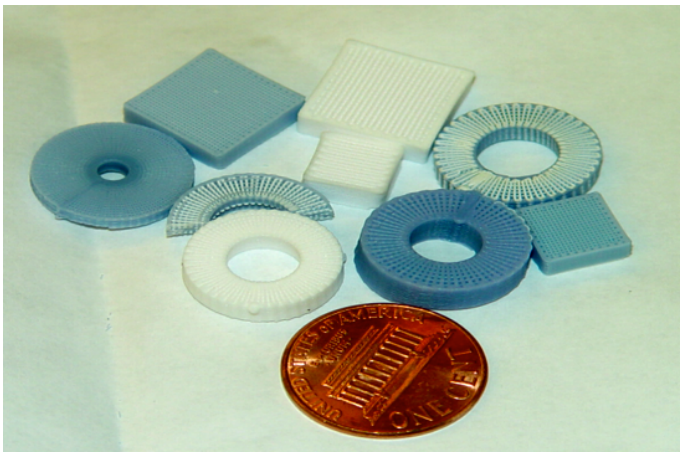

Figure 2.7: This image depicts various designs of scaffolds, compared to a penny, produced on a robocasting machine (3D Inks LLC, Tulsa, OK USA) [10, 54].

2.4 Scaffolds for bone regeneration

Bone tissue-engineering (BTE) strategies can be broken down into three primary components: (a) the extracellular matrix/scaffold, (b) the cells within that matrix/scaffold and (c) the environment within which the cells reside. These principals can be manipulated in order to improve bony healing and regeneration.

Bone extracellular matrix (ECM) sequesters and preserves osteogenic growth factors, and provides a malleable scaffold upon which cells may migrate, adhere, proliferate and differentiate. Many factors can impair successful bony re-ossification. Information on bone development and repair mechanisms has been used to create artificial ECMs designed to overcome obstacles and guide bone regeneration. Many materials have been used clinically (e.g., autologous bone grafts, allogeneic banked bone, ceramic scaffolds composed of calcium-phosphates, demineralized matrix pastes and polymers are reported in the literature.

Tissue engineered scaffolds can be made up of natural or synthetic scaffolds and/or biologic tissue, which may be grown *in vitro* and *in vivo*. A scaffold's macro and micro-structural property is essential for cell signaling, propagation, tissue response, and regeneration.

These properties affect cell survival, cell shape (which may affect differentiation status) and the rate of cell growth.

The essential properties necessary for cell growth include: (1) macro-structure: the scaffold matrix should mimic the physiological functions of the extra cellular matrix (ECM) in order to maintain cell differentiation, (2) pore interconnectivity: and open-pore structure with highly porous surface and micro-structure that allows for cell in-growth. Scaffold porosity provides adequate space for cells to infiltrate and attach to the scaffold and also facilitates ECM formation. Additionally, high permeability of the scaffolds allows for the inflow of nutrients required for cell growth and the excretion of metabolic waste, (3) pore size: the optimal pore size needed for bone ingrowth is believed a range of c.a. 300 μm is optimal but pores as small as 20 μm have resulted in bone ingrowth, (4) surface texture: studies have shown that smooth surface implants exhibited fibrous tissue growth and roughened surfaces displayed bone apposition, and (5) mechanical properties: the scaffold design should exhibit adequate mechanical properties which are needed to support and promote cell growth.

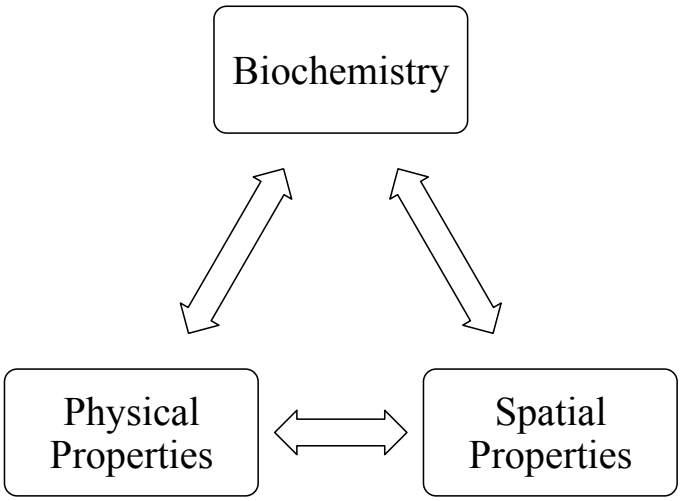

Figure 2.8: Factors influencing cell adhesion in 3D scaffolds [19, 60].

Scaffolds require interconnected pore networks to not only stimulate osteoblast migration and osteoconduction, but also to permit sufficient nutrient support to the cells within the scaffold. With an open weave porous scaffold, trapped blood coagulates to produce a blood clot that can induce inflammation, potentially house an infection, and possibly result in rejection of the scaffold [61].

The structural pore size influences vascularization and cellular content within the material component of the scaffold and also mechanical strength. Previous studies have shown that when constructing a scaffold, the minimum pore size can range from 20 to 200μm for the

osteoconduction and bone maintenance over time. The conventional scaffold fabrication methods, such as solvent casting, particulate leaching, fiber meshing, melt molding have been unable to precisely control pore size and geometry. This is mainly due to their inconsistent and inflexible processing procedures, such as molding to cast scaffolds. Scaffolds require interconnected pore networks to not only stimulate osteoblast migration and osteoconduction [62] but also to permit sufficient nutrient support to the cells within the scaffold. Ripamonte et al. [63] compared bone formation in porous hydroxyapatite (HA) lithomorphs and HA in granular form. Despite the use of "powerful" protein inducers of bone formation (bone morphogenic (BMP) and osteogenic proteins), morphogenesis is "partially controlled by, if not overruled by, the geometry of the scaffold" [63]. In grafted bone, the porosity, not the inherent properties of the graft, determine its survival [13].

Initial matrix mineralization leading to endosseous integration of implants occurs more rapidly (noticeable different by 8 days) with porous surfaced implants than with plasma-sprayed surfaces fabricated with the same materials [13]. A porous surface created by sintering Ti6A14V particles of 45 to 150 μm onto a machined substrate, resulted in a surface with pore size of 50 - 200 μm, pore volume porosity of ~37%, and with three-dimensional interconnectivity between pores. An alternate surface was created from the same material using plasma-spray, creating more irregularity and with lower porosity (5-10%) with little if any inter-pore interconnectivity. Bone response to the two surfaces was compared (in rabbit medial femoral condyles). As early as 8 days post implantation, substantially more mineralized tissue was formed within the pores and adjacent to the sintered particles of the porous-surfaced region than in the plasma-sprayed surface. Certainly, controlled porosity and uniform pore or channel size play and important role not yet well understood.

Healing around an implant is dependent, in part, on the pore size [64], and endosseous integration can be promoted through porous structures that provide large areas that are "strain protected" [65]. An interconnecting porous architecture is one prerequisite for osteoinductivity but, by itself, may not be sufficient to influence bone response [66]. That, in turn, has lead to disagreement in "optimal" pore size with reported values ranging from 200 - 400 μm [67-69]. Over long distances, porosity alone may not be sufficient for diffusion of nutrients.

The influence on tissue response of the relationship between pore size, volume, and interconnectivity and the material, from which a substrate is fabricated, has yet to be established. "The relationship between geometry of biomaterials and host tissue response should be designed by principle rather than empiricism" [63]. One of the long-term objectives has been to clarify the interactions between the material, on the micro-, meso-, and macro-architecture scale of a

scaffold on bone response, leading to rational design of effective tissue-specific scaffolds so that we can ultimately predict combinations of material and scaffold on the micro- (1-20μm), meso- (20-1000μm), and macro- (1-100mm) scales with architectural features that will form fundamental building blocks to create structures for controllable bone response (Figure 2.9 and Table 2.8).

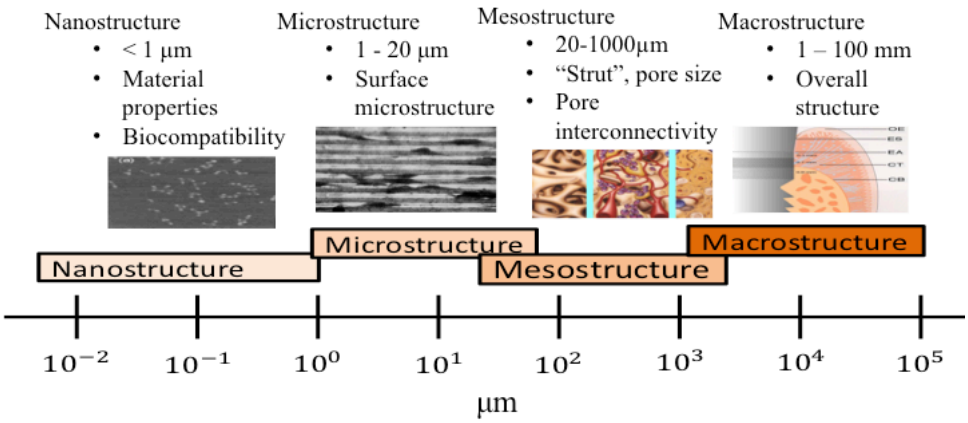

Figure 2.9: This image shows the various scales (nano-, micro-, meso-, and macro-) the scaffolds are associated with along with their corresponding measurements [10].

Pore Size	Biochemical effect/Function
> 1μm	Interaction with proteins
	Responsible for bioactivity
	Type of cells attracted
1 – 20 μm	Cellular development
	Orientation and directionality of cellular ingrowth
	Cellular growth
100 – 1000 μm	Bone ingrowth
	Predominant function in the mechanical strength
	Scaffold functionality
> 1000 μm	Scaffold shape
	Scaffold esthestics

Table 2.8: Hierarchical pore size that an ideal scaffold should mimic to be successful.

CHAPTER 3
QUALITATIVE ANALYSIS OF BIPHASIC CALCIUM PHOSPHATE (BCP) MATERIAL FOR SUBSEQUENT PHASES DURING DEGRADATION PROCESS

3.1 Overview

This chapter details the analysis of the starting materials as well as the finished ceramic product for bone scaffolds which was fabricated via 3D printing. A brief review is given, followed by the materials and methods, with regards to the characterization steps followed for chemical characterization and *in vitro* analysis. The results and conclusion are followed up for this section, with some expected results and the ability to be confident of the process and materials.

3.2 Introduction

Using these specific bioactive materials, HA, β-TCP or a ratio of the two (e.g., 15/85% HA/β-TCP), to achieve a wide range of physical and chemical properties can be achieved. These specific materials have been used as not only as fillers but also as pre-fabricated implants and have shown promising results with respect to mechanical strength in comparison to other available calcium-phosphate (CaP) based ceramics used for grafting (Table 2.4).

With regards to HA, it has proven to be useful due to its high initial compressive strength but its low dissolution kinetics (with a resorption rate of 1-2% per year or no evidence) [16] lead to the investigation and development of a β-TCP ceramic [22]. While β-TCP can resorb in as little as a 6 to 18 month period, this may be considered too rapid to act as a viable scaffold for bone regeneration [16, 22]. Scaffolds fabricated from a ratio of 15% HA and 85% β-TCP has been proven to provide enough initial strength while at the same time allowing resorption in an acceptable time frame [16, 22].

Aim #1 focuses on qualitatively analyzing the calcium-phosphate (CaP) based ceramic powders/materials for their phases during the degradation process. The hypothesis in regards to degradation characteristics is that the scaffolds will degrade *in vivo* and *in vitro* as a function of the two primary phases: (1) HA and (2) β-TCP. Intuition indicates that scaffolds with a higher β-TCP content will dissolve faster. Scaffolds with a higher fraction of the β-TCP phase will most

certainly give a faster time to resorb. The experimental groups in this aim will include HA, β-TCP, or a combination of the two and are as follows: (1) 100% HA, (2) 100% β-TCP, (3) 15/85% HA/β-TCP and (4) 15/85% HA/β-TCP (model) (percentages based on volume fraction). The dissolution characteristics of the structures will be analyzed *in vitro* to observe the effect on the scaffolds, and additionally verify that no secondary or subsequent phases form during the process. Phases such as CPP ($Ca_2P_2O_7$), calcium oxide (CaO), or α-TCP, to name a few are possibilities, which can be derived from the main ceramic components in the scaffold composition.

The XRD spectrum collection of all the groups, including the individual raw materials that were used to fabricate the colloidal gels will be done to do an analysis for the phases. The as-received materials prior to calcination (HA and β-TCP) have shown crystalline phases for the their respective primary phases. However, in previous phase quantification analyses along with Rietveld refinement, small amounts of β-TCP, CPP, and calcium oxide (CaO) exist in for the as-received HA material. Also, minor fractions, <1%, of HA, CPP, and CaO can exist in the β-TCP starting material. Given that the colloidal gels are primarily fabricated without considering the presence of minor quantities of other calcium-phosphate based phases, the beginning compositions of HA, β-TCP, or HA/β-TCP may not necessarily be the same in the final product [10].

The presence of $Ca_2P_2O_7$ prior to calcination has previously been demonstrated to be possible following different HA and β-TCP synthesis routes:

$$2CaHPO_4 + 2H_2O + Ca_{10}(PO_4)_6(OH)_2 \rightarrow 2Ca_3(PO_4)_2 + 2Ca_2P_2O_7 + 2CaO + 6H_2O$$

or

$$Ca_{10-x}(HPO_4)_x(PO_4)_{6-x}(OH)_{2-x}\ (Ca/P=1.5) \rightarrow 2Ca_3(PO_4)_2 + 2Ca_2P_2O_7 + CaO + H_2O$$

[10, 70, 71]. Additionally, the presence of $Ca_2P_2O_7$ following high temperature preparation at long dwell times has been previously identified and quantified through Rietveld refinement [10, 70]. The presence of the rapidly dissolving low stoichiometry phases such, CaO or $Ca_2P_2O_7$, is usually not harmful with respect to the response of host to grafting material. In previous studies [70], it was concluded that the secondary phase, might actually permit initially for rapid dissolution, which in turn may enable further opening of the pore network, allowing the release of Ca and P to the wound-healing site. This would be beneficial because of enhanced transport of nutrients and oxygen; making conditions favorable for osseoconduction. Alternatively, the release of considerable quantities of ions within a quick time frame may prove to be harmful or unfavorable to the continuously changing cells populating the wound-grafting area [19, 70]. Thus

making the chemical properties of the materials and its subsequent phases an important factor for grafting material purposes.

In consideration of the nucleation and formation of an apatite or apatite layer on bioactive materials, an international standard (ISO) was published to evaluate the apatite-forming ability on the surface of biomaterials in a model solution: simulated body fluids (SBF). The SBF solution, proposed by Kokubo et al. contains mineral ions at concentrations comparable to that of human blood plasma (Table 3.6) [72-74]. It has been well documented that the apatite layer can be reproduced on the surfaces of material in SBF and the nanocrystalline apatite formed is quite analogous to the mineral found in bone. This technique has been used to estimate the potential biological activity of a biomaterial and is useful for evaluating in a quantitative manner bone-bonding ability of a biomaterial prior to an *in vivo* experimentation.

Two important factors, (1) biodeterioration and (2) biodegradation of bioceramic materials determine its durability. Biodeterioration signifies when the modification of the implant is not essentially wanted while biodegradation is one of its advantages. There are a few routes that contribute to biodeterioration and biodegradation: mechanical wear, spontaneous reactions of the implant materials with body fluids, and cell-mediated alterations. Mechanical wear is of course occurring at the interface between mobile parts of a scaffold but it is also observed at the tissue–scaffold interface, and is primarily related to micromovements which results in wear residues along with possibility of an inflammatory reaction. This is limited when there is a strong bond between the tissue and bioceramic scaffold.

The *in vivo* biodegradation rate is directly associated to the solubility behavior of the materials constituting the bioceramic [29]. The different CaP mixtures demonstrate solubility behaviors that vary from one another. Several physical–chemical factors affecting biodegradation can be accounted for with one of the common ones being the de-cohesion of the material related to material with the higher solubility, thus leading to the release of crystals or particulates of the least soluble, more stable, phase. This has been the case of HA plasma-sprayed coatings, and can be translated to the biphasic HA/β-TCP ceramics. The size of these particles can prompt different body responses. When the particles, which released are small enough, they can enter the process of phagocytosis eventually being eliminated. However, if elimination is not possible, they may initiate an inflammatory response, which can possibly be harmful. For example, if a material is not fully sintered or when a CaP bioceramic is combined with a rapidly absorbed matrix. Recent CaP compounds developed can be modified by manipulating their respective component phase ratios. As is seen in BCP compound, HA/β-TCP ceramics, where the degradation rate can be

specifically tailored by modifying the proportion of the β-TCP, more soluble phase, which degraded preferentially to HA upon cellular activity.

Comparably other physiochemical features have been known to influence the degradation rate of bioceramics *in vivo* (e.g., porosity and crystallinity). Macroporosity (pore diameter in the range ~350μm) seems to be a key; especially in the case of ceramics made of insoluble CaP in body fluids. The macropores permit cell invasion, in-turn, increasing the number of dissolution sites. The effect of microporosity is difficult because initially the effect seems related to a lesser content in material while a resultant effect is related to the increase of the surface area and it relation to the dissolution rate. So when considering the composition, highly microporous ceramics are faster absorbed in comparison to those of less porosity. Additionally, crystallinity has been shown to be an important factor with the possibility of being related not only to the increase of the surface area but dissolution rate as well.

3.3 Experimental Section

3.3.1 Material Processing

Commercially available powders of hydroxyapatite (HA) (Honeywell, Reidel-de Haën, Germany) $Ca_{10}(PO_4)_6(OH)_2$ and beta tri-calcium phosphate (β-TCP) (Sigma-Aldrich, St. Louis, MO) $Ca_3(PO_4)_2$ are used as ceramic materials in this study. The as-received powders were calcined in seperate alumina crucibles at 800°C for 11 hours. After cooling, each powder was attrition milled (1.0 mm zirconia milling media, Union Process, Akron, Ohio) in distilled water (DI-H_2O) for 30 minutes (Model L001 Attritor System, Union Process, Akron, Ohio). The water-ceramic suspensions were then separated from the milling media. The ceramic slurries were placed in a low temperature oven (~80°C) for approximately 8 hours to allow the water to separate/evaporate and leaving the dried solid material. The resulting solid materials were then transferred into a Nalgene bottles [10] charged with ~15 pieces of zirconia milling media (10mm diameter) which were then violently agitated for ~15 minutes in a paint shaker (1400 Classic Shaker, Red Devil Equipment Company, Plymouth, MN). The powders were then stored in a in a dedicated containers in a desiccator cabinet.

3.3.2 Colloidal Gel Preparation

The previously calcined and milled ceramic powders were used for the colloidal gel formulation. Concentrated HA, β-TCP, and HA/β-TCP suspensions for the four experimental groups (Table 3.1), where volume fraction ($\phi_{ceramics}$) of ceramic was $\phi_{ceramics}$= 0.42 to 0.5, were produced by mixing a pre-calculated (Equations (3.3.1-(3.3.7)) amount of ceramic powder and

ammonium polyacrylate dispersant (Darvan 821A®; RT Vanderbilt, Norwalk, CT) to stabilize the ceramic particles in DI-H_2O. Darvan 821A is a 40% aqueous solution of ammonium polyacrylate. The dispersant proportion per gram of ceramics was ~15 mg [10, 75]. First, about 25 g of milling media was added to the DI-H_2O, then the dispersant, and then the ceramic powder in 3 parts (33.3% + 33.3% + 33.3%). After each addition of powder, the suspension is mixed in the planetary mixer (Thinky AR-250; Thinky, Tokyo, Japan) for 1 minute. Next, hydroxypropylmethylcellulose, also referred to as F4M, (Methocel F4M; Dow Chemical Company, Midland, MI) was added as the viscosifying agent. The F4M is used in a 5% by weight aqueous solution with a proportion of 7 mg per milliliter of liquid phase (Table 3.2). The suspension was then mixed for 1 minute followed by a defoaming step for 1 minute in the planetary mixer. Finally, the suspension was gelled by adding ~150 mg per 30 mL of ink of polyethyleneimine (PEI) (Sigma-Aldrich, St. Louis, MO) 10% by weight solution. Mixing and defoaming (1 minute and 30 seconds, respectively) after the final addition completed the ink preparation procedure. An example of the necessary components and their corresponding calculations is presented below in Table 3.2 and Table 3.3. The resulting colloidal gel needed to be printable through the desired size of the nozzle, which meant the paste needed to be not only stiff enough to maintain the shape of the extruded filament after deposition, but also soft enough to be extruded through the nozzle by applying pressure.

Group	Description	Abbreviation
1	100% HA	HA
2	100% β-TCP	β-TCP
3	15/85% HA/β-TCP	BCP
4	15/85% HA/β-TCP (mixed model)	BCP (deisgn)

Table 3.1: Experimental groups of colloidal gels/scaffolds for testing for Specific Aim #1.

Substance	**Quantity (g)**
DI-water (H_2O)	19.40
Darvan 821A®	1.025
β-TCP	54.55
HA	9.45
F4M (5%)	3.90
PEI (10%)	1.25

Table 3.2: ϕ_{solids}=0.46 - HA(15%)/β-TCP(85%)

15/85% HA/β-TCP		
$\phi_{ceramic}=0.46$	$\rho_{\beta\text{-}TCP}=3.1\frac{g}{mL}$	
$V_{total}=45mL$	$\rho_{HA}=3.04\frac{g}{mL}$	
$V_{solid}=(V_{total})\cdot\phi_{ceramic}=20.7mL$		(3.3.1)
$V_{liquid}=(V_{total})-V_{solid}=24.3mL$		(3.3.2)
$V_{\beta\text{-}TCP}=(0.85)\cdot(V_{solid})=17.595mL\cdot\left(\rho_{\beta\text{-}TCP}\right)=54.545g$		(3.3.3)
$V_{HA}=(0.15)\cdot(V_{solid})=3.105mL\cdot(\rho_{HA})=9.439g$		(3.3.4)
$M_{821A}=(0.016)\cdot(V_{\beta\text{-}TCP}+V_{HA})=1.024g$		(3.3.5)
$M_{F4M}=\left[\left(8\frac{mg}{mL}\right)\cdot\left(10^{-3}\right)\frac{g}{mg}\cdot(V_{liquid})\Big/\left(0.05\frac{g\cdot mol}{g\cdot stock\ solution}\right)\right]=3.888g$		(3.3.6)
$M_{H_2O}=(V_{liquid}-M_{F4M}-M_{821A})\approx19.4g$		(3.3.7)

Table 3.3: Example calculation for colloidal gel formulation

3.3.3 Fabrication of the 3D Scaffold

The three-dimensional direct-write printer used a gantry robot with affixed syringe pumps to extrude the colloidal inks (Table 3.1) through a fine nozzle to build the three-dimensional scaffold (Figure 3.1) [58, 75]. The three-dimensional disc-shaped scaffolds (10-mm diameter, 1-mm thickness, 330 μm struts, and 500μm pore size) (Figure 3.1) were designed on a computer-aided design (CAD) software (RoboCAD 4.1, 3D Inks, Tulsa, OK), which outputs x-y-z motion commands along with the necessary coordination of syringe pumping commands to extrude the proper volume flow rate of ink. The resulting machine code is suitable to be read by a U500 motion controller (Aerotech Inc, Pittsburgh, PA). The syringe pumps are constant volume ram extruders rather than air pressure driven. The ink layers are deposited sequentially, starting with the bottom layer. The three-dimensional disc-shaped scaffolds were printed layer-by-layer at 10 mm/s deposition rate onto a flat ceramic substrate (ADS-96R, Coors Tek, Grand Junction, CO) in low-viscosity paraffin oil (Ultra-Pure lamp oil, Lamplight Farms Inc., Menomonee Falls, WI) to prevent drying of the structure during assembly. Once a layer was finished, the nozzle was translated upward by $\Delta z = \left(\pi/4\right)\cdot D$, (D = inner diameter of the nozzle) and another layer was begun. This was repeated until the desired height of the structure (i.e., 1 mm) was reached. Cylindrical nozzles (EFD Inc, Nordson, Westlake, OH) of 330 μm diameter (23 gauge, Part # 7018314) are used for extrusion because the post-sintering diameter for bone scaffolds was designed to be ~267(±2) μm (Figure 3.2) [10]. The difference between the initial and final

dimension of the struts is known as shrinkage and occurs when the water and binder is lost and sintering occurs.

$$\text{Designed porosity} = \left(\frac{(RW \cdot D_{tip}) - \left(\frac{\pi}{4} \cdot D_{tip}^2\right)}{(RW \cdot D)}\right) = 1 - \frac{\pi \cdot D}{4 \cdot RW} \tag{3.3.8}$$

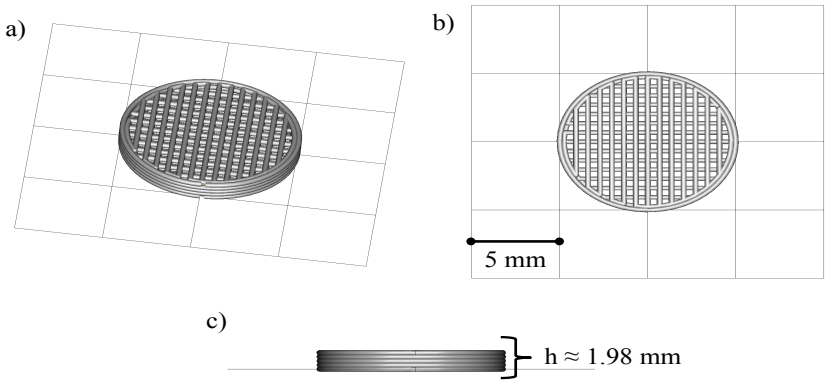

Figure 3.1: Schematic of scaffold designed in RoboCAD 4.1 (3D Inks LLC, Tulsa, OK) (a) Iso view, (b) top and (c) front/side view.

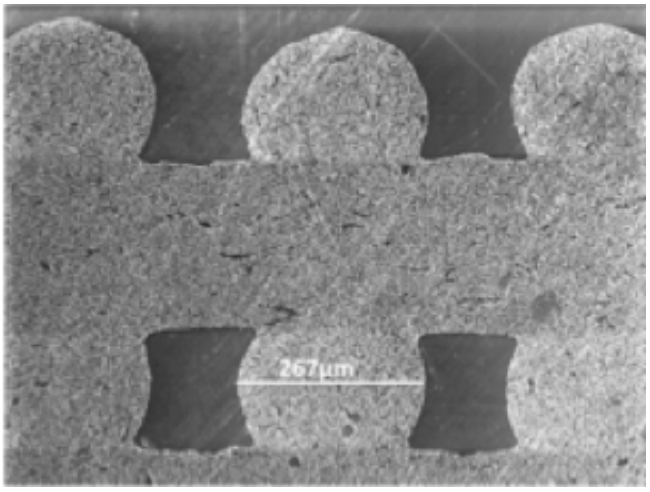

Figure 3.2: This SEM image displays the size of the rods as well as pore size and road width between each layer [10].

3.3.4 Heat treatment of fabricated scaffolds

After the scaffolds were fabricated, the substrate was removed from the oil bath and allowed to dry in air for ~12 hours prior to the sintering process. Heat treatment of the scaffolds

was performed utilizing an electric furnace (Model LHT 02/17, Nabertherm GmbH, Lilienthal, Germany) to enhance the mechanical strength for handling during the experiments (e.g., *in vitro* dissolution study) [75]. During the sintering processing, the green body ceramic was densified, and organic components were burned off. The firing protocol began by heating at 2°C/min until 400°C, dwell at 400°C for 2 hour, then heating until 900°C (~8°C/min), dwelling for 2 hours at 900°C, heating at 3.3°C/min to ultimate temperature of 1100°C, dwelling at 1100°C for 4 hours, and finally a cooling at ~8.0°C/min until the samples cooled to room temperature (~30°C) (Figure 3.3). The binder burnout during the sintering process results in a predictable volumetric shrinkage (~20%) and can result in defects such as cracking and warping [76]. The sintering shrinkage of ceramics is an unavoidable step, and all dimensions of the designed geometric structure must be enlarged to account for this phenomena and to ultimately attain the final desired dimensions.

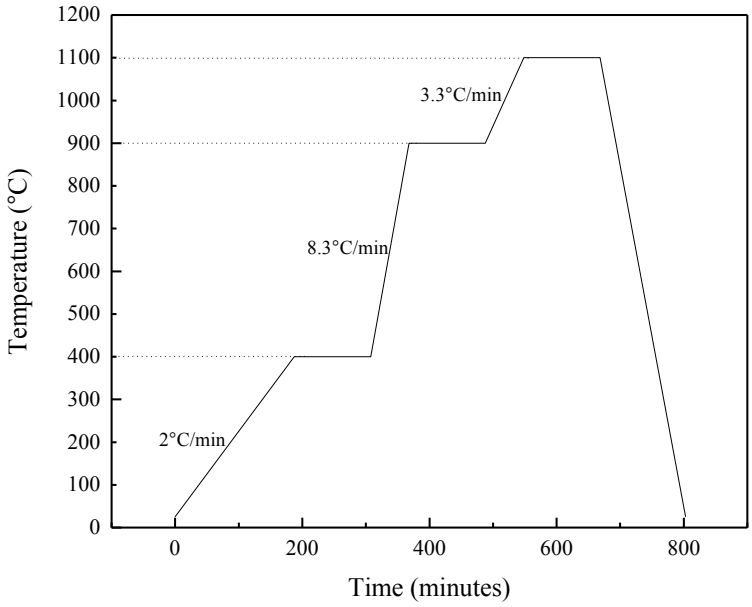

Figure 3.3: Sintering temperature regime for the four experimental groups, with a ultimate sintering temperature equal to 1100°C.

3.3.5 Density and Porosity Measurements

The density and porosity of the experimental ceramic scaffolds was characterized using helium pycnometry (Accupyc 1340, Norcross, GA) to measure the true solid volume of the sample (V_{solid}) by averaging across 10 independent measures per specimen (n=10 per group). The length and diameter of each sample was determined by averaging three independent

measurements to calculate the volume of the bounding cylinder ($V_{cylinder}$). This allowed computation of porosity as the void volume fraction as [10, 77].

$$\text{Void Volume Fraction}=\left(1-\left(\frac{V_{solid}}{V_{cylinder}}\right)\right) \tag{3.3.9}$$

$$W_{solid}=\varrho_{ceramic}\cdot h\cdot\pi\cdot\frac{D^2}{4} \tag{3.3.10}$$

$$W_{porous}=(1-\phi_{pore})\rho_{ceramic}\cdot h\cdot\pi\cdot\frac{D^2}{4} \tag{3.3.11}$$

$$\phi_{pore}=1-\frac{W_{porous}}{\rho_{ceramic}\cdot V_{cylinder}} \tag{3.3.12}$$

3.3.6 Inductive Coupled Plasma (ICP)

Calcium (Ca) and phosphrous (P) concentrations were determined using ICP (Thermo Jarell Ash, Trace Advantage). For this purpose, 10 milligrams of powder from each of the groups listed in Table 3.4 were dissolved in 1:1 HCl (35%) and made up to 100mL of double distilled water in a volumetric flask. Suitable standard solutions for Ca (0, 20, and 40ppm) and P (0, 10, and 40ppm) and were prepared from 100 ppm standard solutions of the respective elements (Fisher Scientific, Pittsburgh, PA, USA). Each specimen in solution and standard solutions was pumped through argon plasma, which was excited by 2kW, 27.12 MHz radio frequency generator [78].

Group	State
100% HA	Raw
	Calcined – 800°C
	Sintered – 1100°C
100% β-TCP	Raw
	Calcined – 800°C
	Sintered – 1100°C

Table 3.4: The above table lists the six experimental groups, which were subjected to ICP analysis for Ca/P verification.

3.3.7 Powder Characterization X-ray Diffraction

The XRD (Bruker AXS D8 Discover, Madison, WI) was used to determine the crystalline phases present within the raw material and various experimental groups. Three different spectra from each testing group were obtained (n=3 per group). The diffractometer, using a curved crystal monochromator, operating at 45mA and 45kV, and scanned in the 2θ with a range from 20-65° [10], with a step size of 0.02° at 3 seconds per step.

Rietveld refinement analysis used the data collected from X-Ray diffractometer, which subsequently converted data to "*.xy*" format. The raw data was then input into, Material Analysis Using Diffraction (MAUD) software for quantitative analysis. Rietveld analysis utilized the samples from previous XRD spectra (i.e., peak, heights, widths and positions). This refinement method was used to quantify the percentage of each phase (HA, β-TCP, and other commonly observed phases in calcium- and phosphate-based materials such as calcium oxide, CaO) present in different calcination temperatures and sintering groups. A least square fit approach was utilized to measured scans until replicating a theoretical scan (based on the structure in Inorganic Crystal Structure Data Base-(ICSD)) [79, 80]. The background, cell parameters, preferred orientation; peak asymmetry, atomic positions, site occupancy factors and global vibrational parameters were refined. The calculated and observed patterns were plotted by least squares method until a minimum was reached. Five iterations were utilized and the integrated intensities and the peaks heights were related to a scale factor. The fraction of each phase was determined by

$$W_i = \frac{S_i (ZMV)_j}{\sum S_j \left(ZMV_j\right)} \tag{3.3.13}$$

where, W_i is the weight fraction of the phase, S is the scale factor, Z is the number of formulas per unit cell, M is the mass of the formula unit, V the unit cell volume, and i and j are the phase under analysis and j all phases in the system [10, 70].

3.3.8 Fourier Transform Infrared Spectrometer (FT-IR)

The FT-IR (Varian 680, Agilent Technologies, Santa Clara, CA) analyses were made for the different experimental groups (n=3 per group). Pellets were fabricated by mixing 1 milligram of the desired specimen with 250 milligrams KBr (IR grade, Thermo Scienctific). A range of 4000 to 400 cm^{-1} was scanned [10].

	HA		β-TCP	
Pattern Number	09-0432	74-0566	09-0169	70-2065
Crystal System	Hexagonal	Hexagonal	Rhombohedral	Rhombohedral
Space Group	$P6_3/m$	$P6_3/m$	R-3C	R3C
a (Å) (=b)	9.418	9.424	10.429	10.439
c (Å)	6.884	6.879	37.38	37.375
RIR	None	1.06	None	1.25

Table 3.5: The parameters utilized for reference patterns for XRD analysis, retrieved from PDF-2® [81].

3.3.9 Differential scanning calorimetry (DSC) and Thermogravimetric analysis (TGA)

After drying, the colloidal gels were individually heated in a differential scanning calorimetry/thermogravimetric analyzer (TGA) (STA 449 F1 Jupiter®, Burlington, MA) to characterize possible dehydration of Ca^{2+} and burnout behavior as a function of temperature. The heating profile from 40°C to 1250°C was carried out with a ramp rate of 2.5°C/min in zero hydrocarbon air composed of 80/20 N_2/O_2 ratio (ZHCAir, Airgas USA, Radnor, PA) with flow rate set to 150mL/min.

3.3.10 Dissolution analysis

Degradation of scaffolds was evaluated by determining the scaffold weight loss as a function of the immersion time in simulated body fluid (SBF) with a starting pH of ~7.2 at 37°C, to mimic body conditions with ion concentrations approxiametly equal to those of the inorganic constituents of human blood plasma (Table 3.6). The fluids were changed regularly, for time periods up 28 days (4 weeks). Weight loss was measured regularly, and samples were fully characterized as weekly time points [82]. The composition of the SBF corresponds to the

corrected SBF solution previously published by Kokubo and Takadamaa [73]. A ratio of 1 g of scaffold to 50 mL of SBF was used for each test. After removal from the SBF at selected times, the scaffolds were dried at ~70°C for 24 hours and weighed (XS Analytical, Mettler Toledo, Columbus, OH). The weight loss was defined as:

$$\Delta W_t = \left(\frac{W_0 - W_t}{W_0}\right) \cdot 100\% \quad (3.3.14)$$

where W_0 is the initial mass of the scaffolds and W_t is the mass at time (t) (t=1, 7, 14, 21, and 28 days). An initial dry weight of the scaffolds was recorded, and then samples are immersed in SBF for ~1 hour, blotted dry and weighed. This value is considered the initial wet weight that is taken in consideration as W_0 [76].

	Concentration ($mmol/dm^3$)	
	Simulated Body Fluid (SBF)	Human Blood Plasma
Na^+	142.0	142.0
K^+	5.0	5.0
Mg^{2+}	1.5	1.5
Ca^{2+}	2.5	2.5
Cl^-	147.8	103.0
HCO_3^-	4.2	27.0
HPO_4^{2-}	1.0	1.0
SO_4^{2-}	0.5	0.5

Table 3.6: Ion concentrations of the SBF solution compared to that of human blood plasma.

3.3.11 Scanning Electron Microscopy (SEM)

A field emission scanning electron microscope (FE-SEM) (Hitachi S-4800, Santa Clara, CA) was used to observe the porosity and surface of the scaffolds. Scaffolds from the four experimental groups and selected *in vitro* time points were mounted onto standard SEM pin stub mounts, (Product #: 16111, Ø12.7mm x 8mm pin height) (Ted Pella, Inc. Redding, CA), grounded with Graphite Conductive Adhesive 154 (Electron Microscopy Sciences, Fort Washington, PA), and mounted to a multi holder for 8 pin stubs (Product #: 15310-8) (Ted Pella, Inc. Redding, CA). The multi holder was placed into the sputter coater (Edwards S150B Sputter Coater, Sanborn, NY) and coated with a thin layer gold for one minute and thirty seconds.

3.3.12 Statistical analysis

For statistical evaluation, analysis of variance (ANOVA) at 95.0% confidence interval using IBM SPSS Statistics *ver.* 22 (IBM Corporation Armonk, NY) was utilized considering

materials as independent variables. Multiple comparisons between groups were performed by the Tukey's post-hoc test.

3.4 Results and Discussion

The results for specific aim #1 are presented in the following sections, beginning with density/porosity results followed by the powder and scaffold characterization sections. Additionally, DSC and TGA data is presented in the following subchapter along with FTI-IR to give added value and characterization of the scaffolds and their respective material composition.

3.4.1 Density and Porosity Measurements

The theoretical densities of the ceramics used for ink formulations (i.e., 100% HA, 100% β-TCP, and 15/85% HA/β-TCP)are 3.16 g/cm^3, 3.07 g/cm^3, and 3.08 g/cm^3, respectively. The mixture of HA/β-TCP in both experimental groups (15/85% HA/β-TCP and 15/85% HA/β-TCP (design)) has a density based on a volume fraction of the weighted average of the individual HA and β-TCP densities. The density measurement by He pycnometry match literature values for pure (100%) HA and β-TCP. The as-sintered scaffold trend observed in Figure 3.6 indicated the amount of micro-porosity in the scaffolds decreases as sintering temperature increases. Porosity decreases from 23.52% in the rods at 1100°C to 8.32% at 1125°C and disappears entirely at 1250°C. A parallel trend is followed by the total porosity while the meso-porosity remained relatively constant from 28.23% to 22.85% (within respective error limits).

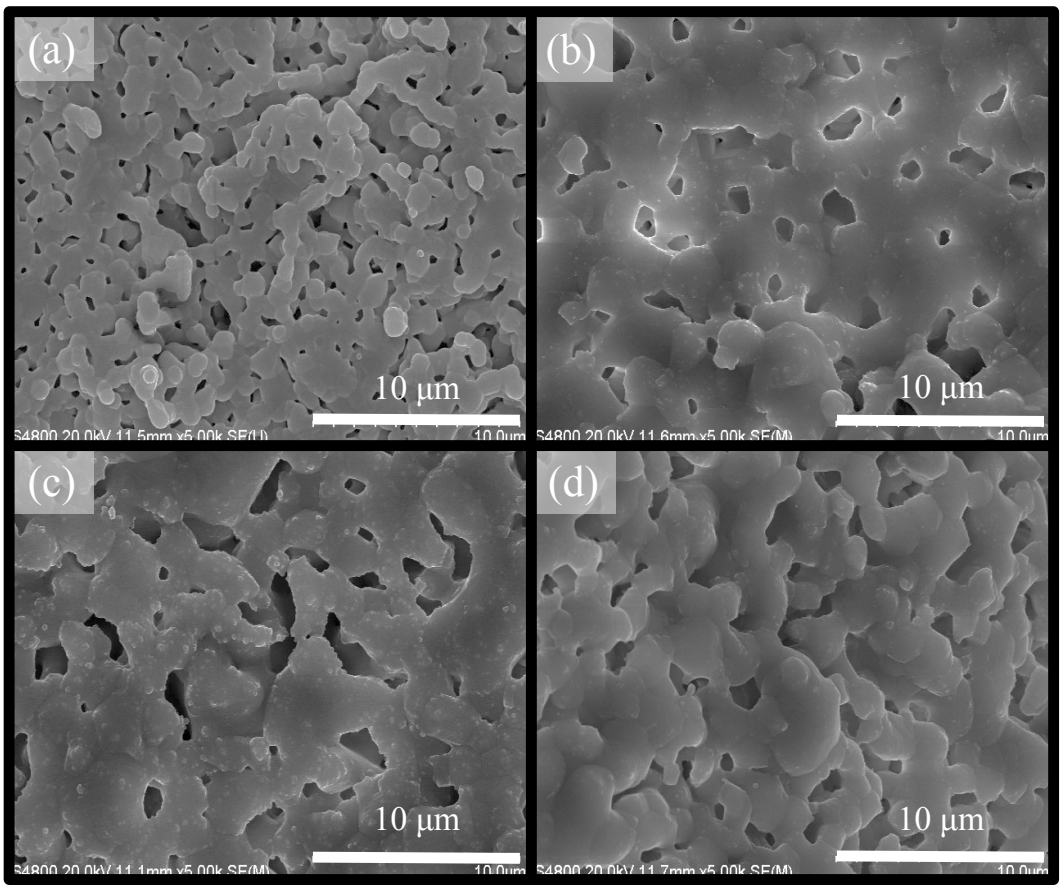

Figure 3.4: SEM micrographs of the four experimental groups: (a) 100% HA, (b) 100% β-TCP, (c) 15/85% HA/β-TCP, and (d) 15/85% HA/β-TCP (design). These images are taken post heat treatment to 1100°C for 4 hours. The images were taken at 20kV and 5000x.

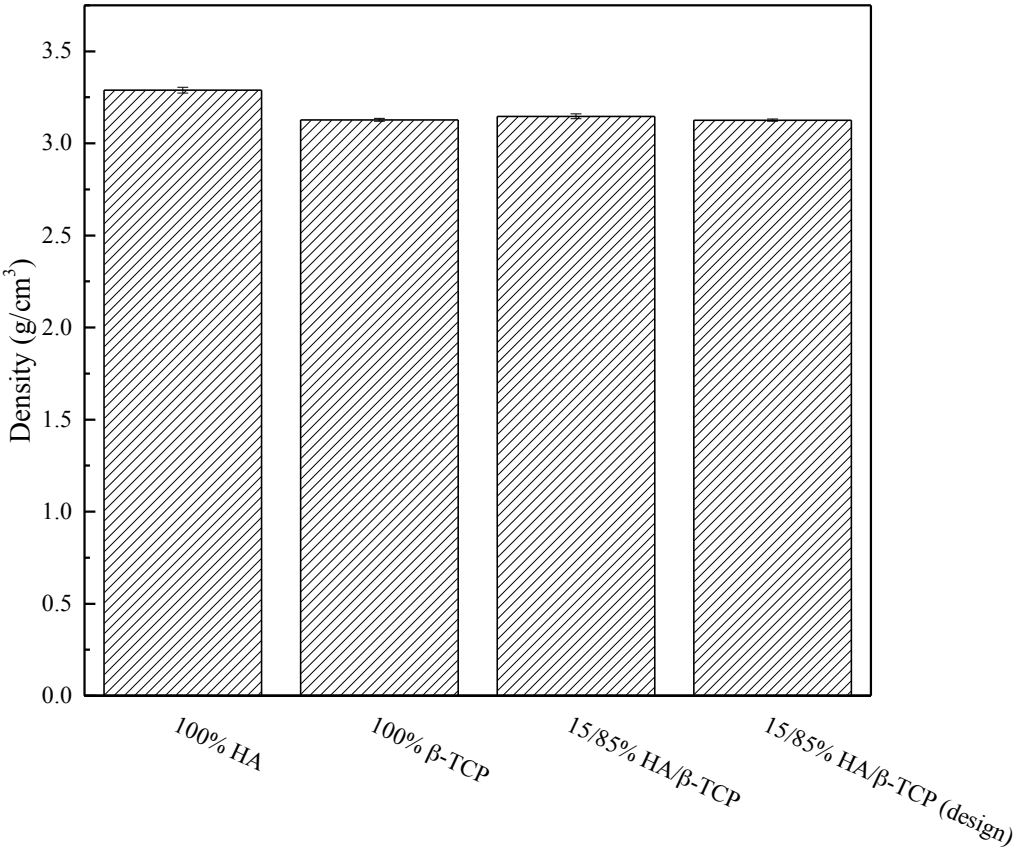

Figure 3.5: Bar graph representing the four experimental groups' density along with their respective standard deviation (S.D.).

Experimental Group	Mean (g/cm^3)	S.D.
100% HA	3.288	±0.016
100% β-TCP	3.128	±0.008
15/85% HA/β-TCP	3.147	±0.013
15/85% HA/β-TCP (design)	3.126	±0.006

Table 3.7: The mean experimental density (g/cm^3) of the four groups along with the 95% confidence interval.

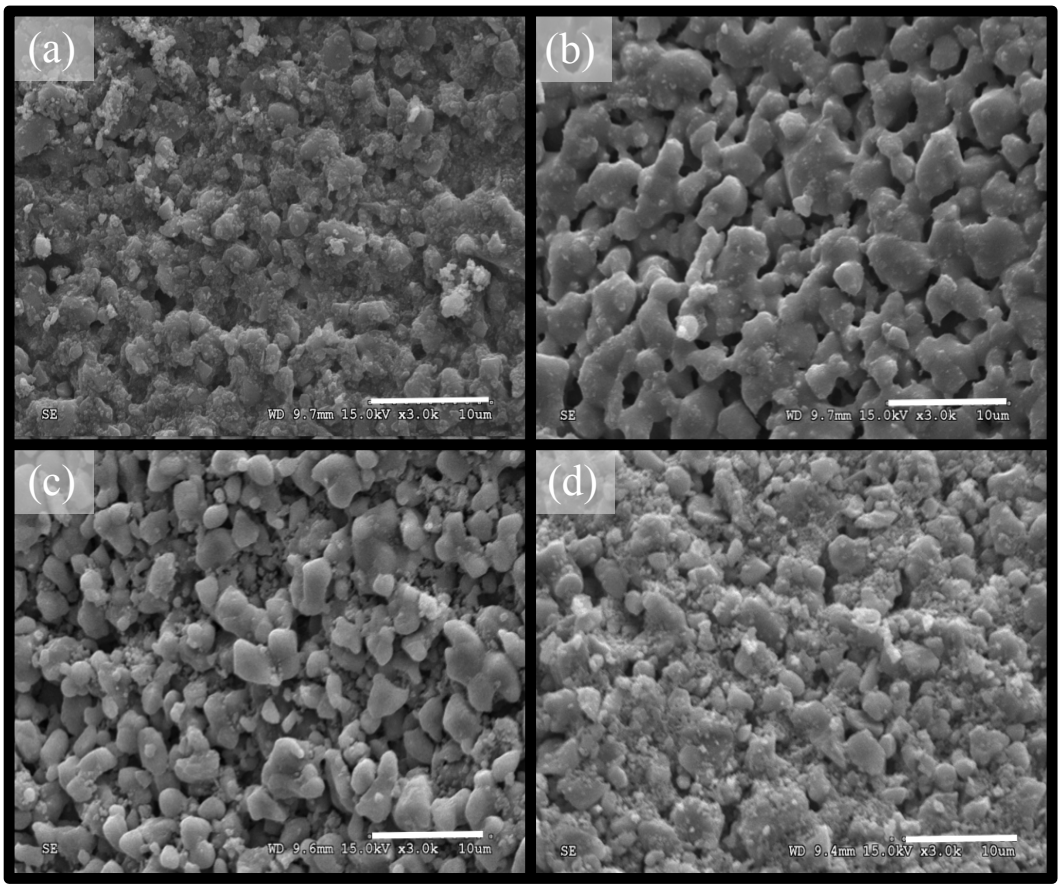

Figure 3.6: SEM images of the surface of a 15/85% HA/β-TCP scaffold from Hitachi S3500N at 15.0kV at 3000x. (a) green state, (b) sintered to 900°C, (c) sintered to 1100°C, and (d) sintered to 1250°C.

Sintering Temperature	Mean	S.D.
Green State	50.61[a]	±5.18
900°C	46.41[b]	±1.72
1100°C	44.21[c]	±1.98
1250°C	37.92[d]	±3.38

Table 3.8: Percent porosity (mean ± 95% confidence interval) of 15/85% HA/β-TCP based on sintering temperature. The letters represent statistically homogeneous groups.

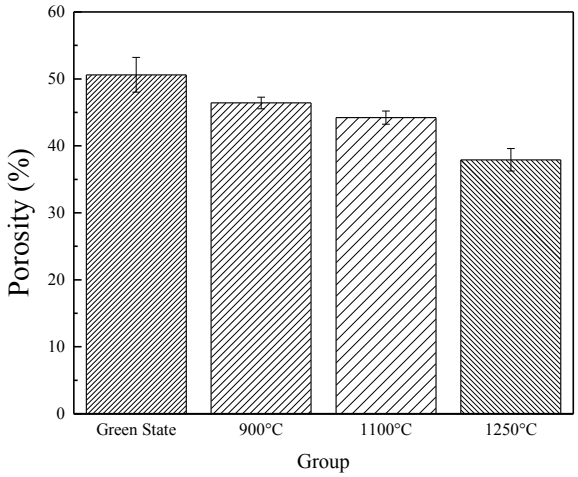

Figure 3.7: Percent porosity (mean ± 95% C.I.) for 15/85% HA/β-TCP at green state and various sintering temperatures.

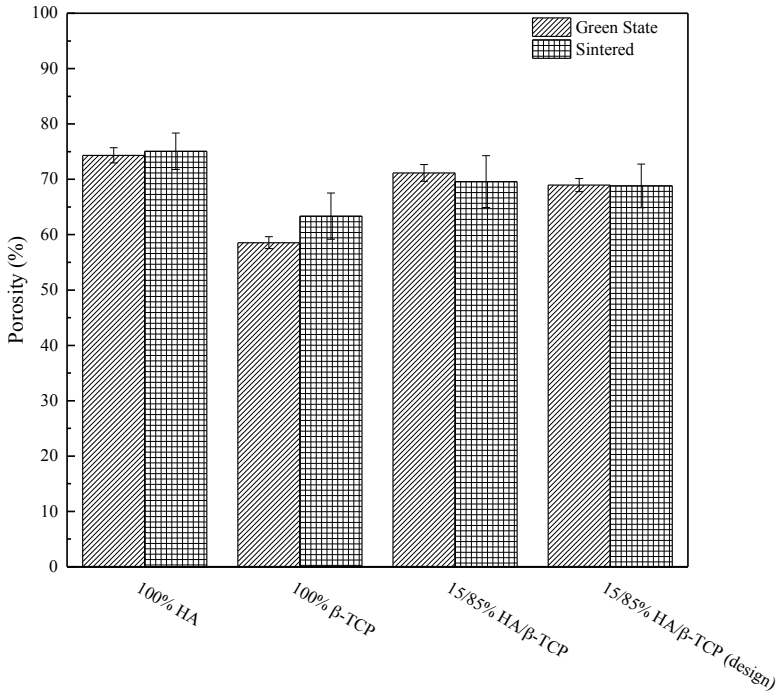

Figure 3.8: Bar graph representing the four experimental groups' (green state and sintered) mean percent (%) porosity along with their respective standard deviation (S.D.).

	Green State		Sintered	
Experimental Group	Mean	S.D.	Mean	S.D.
100% HA	74.33	±1.36	75.07	±3.3
100% β-TCP	58.56	±1.06	63.36	±4.18
15/85% HA/β-TCP	71.16	±1.51	69.59	±4.67
15/85% HA/β-TCP (design)	68.97	±1.18	68.82	±3.95

Table 3.9: The mean percent porosity (%) of the four groups, and their two states, green and sintered, along with the 95% confidence interval.

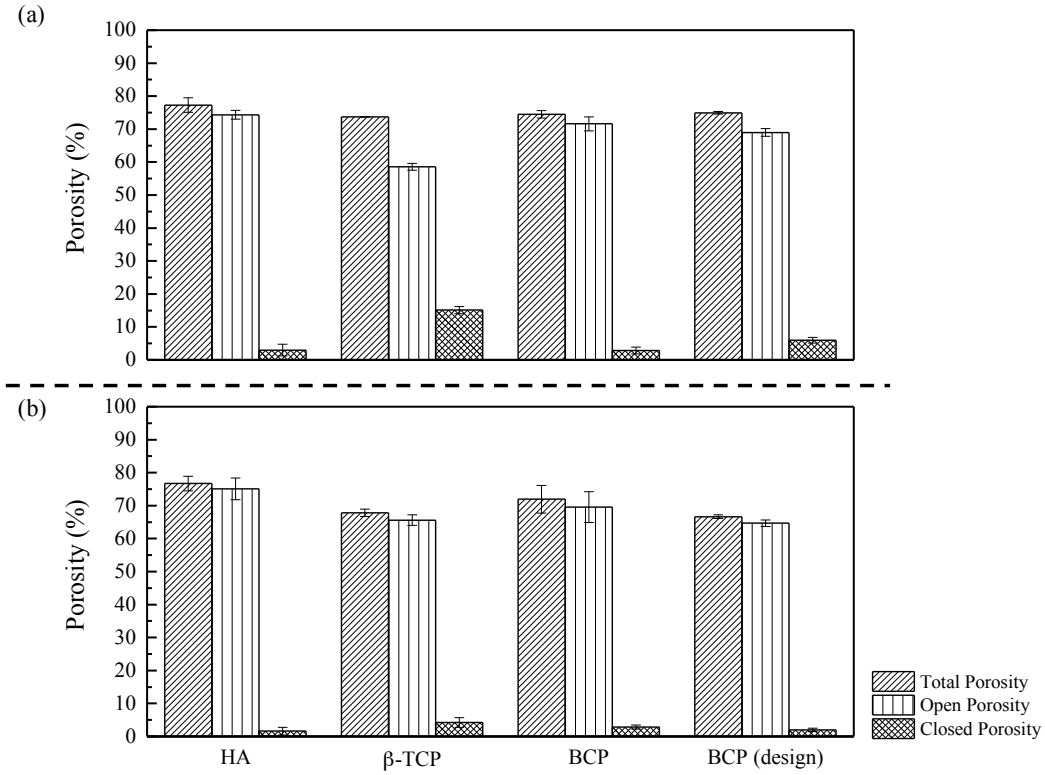

Figure 3.9: (a) Green state and (b) sintered state

		π_t	π_a	π_f
100% HA	Green State	77.29% (±2.20)	74.33% (±1.36)	2.97% (±1.80)
	Sintered	76.69% (±2.23)	75.07% (±3.30)	1.63% (±1.18)
100% β-TCP	Green State	73.69% (±0.02)	58.58% (±1.06)	15.11% (±1.06)
	Sintered	67.82% (±1.14)	65.58% (±1.60)	4.24% (±1.46)
15/85% HA/β-TCP	Green State	74.48% (±1.15)	71.62% (±2.12)	2.86% (±1.02)
	Sintered	71.95% (±4.21)	69.59% (±4.67)	2.37% (±0.64)
15/85% HA/β-TCP (design)	Green State	74.92% (±0.39)	68.97% (±1.18)	5.95% (±0.86)
	Sintered	66.65% (±0.59)	64.68% (±0.97)	1.98% (±0.52)

Table 3.10: Table summarizing the closed, open, and total porosity, of the four experimental groups, in their respective green and sintered states.

3.4.2 Calcium (Ca) to Phosphorous (P) ratio verification

The ICP was completed to determine the Ca/P ratio of the two individual materials, in each of the 3 respective states: (1) raw, (2) after calcination at 800°C, and (3) post sintering 1100°C. The trend in the TCP group seemed to show a decrease from raw to after calcination step, but then an increase once sintered (Table 3.11 and Figure 3.10). While the Ca/P ratio slightly increased while going from raw, to calcined, and ultimately sintered in the HA group (Table 3.11 and Figure 3.10). The one-way ANOVA statistical analysis resulted in a p=0.0204 and p=0.022, for HA and β-TCP respectively, indicating a significant effect due to the state of the material.

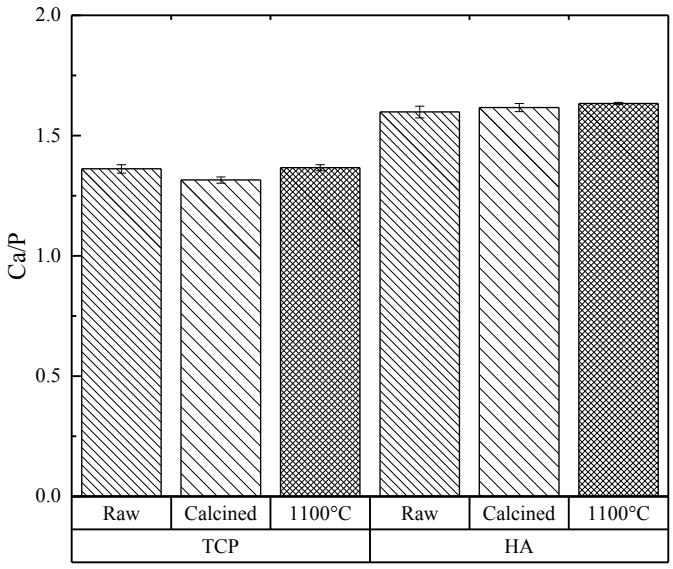

Figure 3.10: Mean ± 95% confidence intervals for Ca/P ratio depicting the two primary groups (HA and β-TCP) and their state.

	HA		β-TCP	
State	Mean	S.D.	Mean	S.D.
Raw	1.60[a]	±0.02	1.36[c]	±0.02
Calcined (800°C)	1.62[a]	±0.02	1.32[d]	±0.01
Sintered (1100°C)	1.63[a,b]	±0.00	1.37[c,e]	±0.01

Table 3.11: Mean ± 95% confidence intervals for Ca/P ratio depicting the two primary groups (HA and β-TCP) and their state. The letters depict statistically homogeneous groups.

3.3.3 Material Characterization X-ray Diffraction

XRD spectra were collected of the individual raw materials (Figure 3.11) for crystalline verification. Their spectra were matched to the theoretical HA and β-TCP. After confirmation of the material was complete, and the experimental colloidal gels fabricated and subjected to sintering at 1100°C, XRD spectra were obtained from the groups for crystalline phase determination and verification. The β-TCP phase is indicated by three high intensity peaks located at 27.9°, 31.2° and 34.4° while the highest peaks for HA are at 31.8° and 32.9° (Figure 3.11). High crystallinity was indicated by the narrow diffraction peaks described as sharp peaks. This result is in good agreement with other researchers' works that found that biphasic mixing on a crystallite level is feasible [81, 83, 84]. The XRD refinement results were used to give an approximate Ca/P ratio by applying the following equation (3.4.1):

$$Ca/P=\sum_{i}^{2}\left[wt\%_i\times(Ca/P)_i\right] \tag{3.4.1}$$

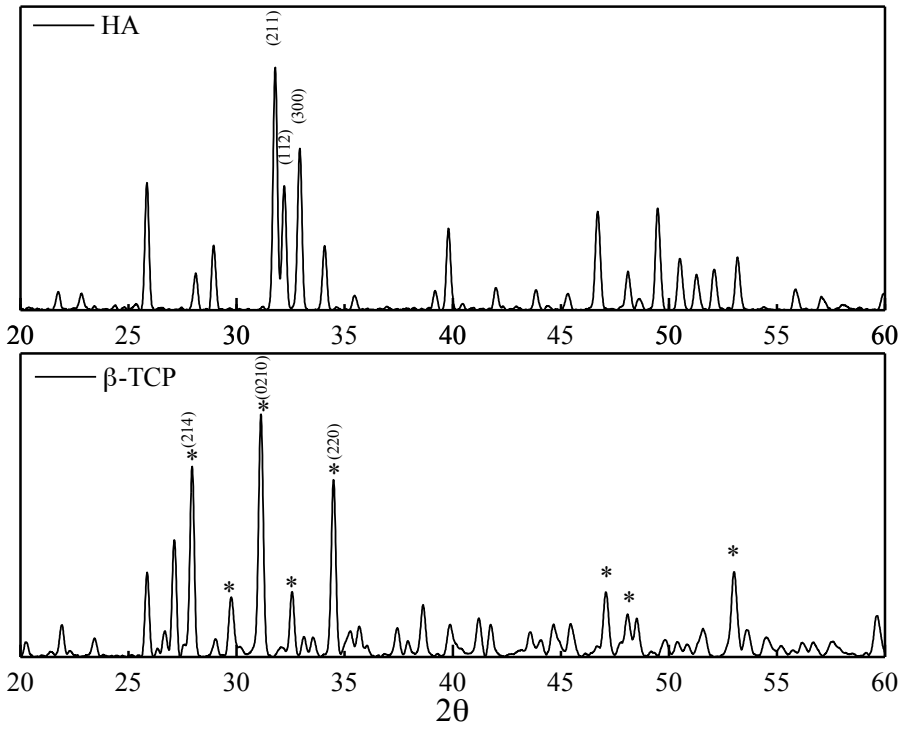

Figure 3.11: This XRD spectrum is a comparison between the two basic components of the ink. The upper box represents the XRD spectra of hydroxyapatite (HA) group while the lower box represents the β-TCP group. A few of the most intense diffraction peaks are shown on the spectra above.

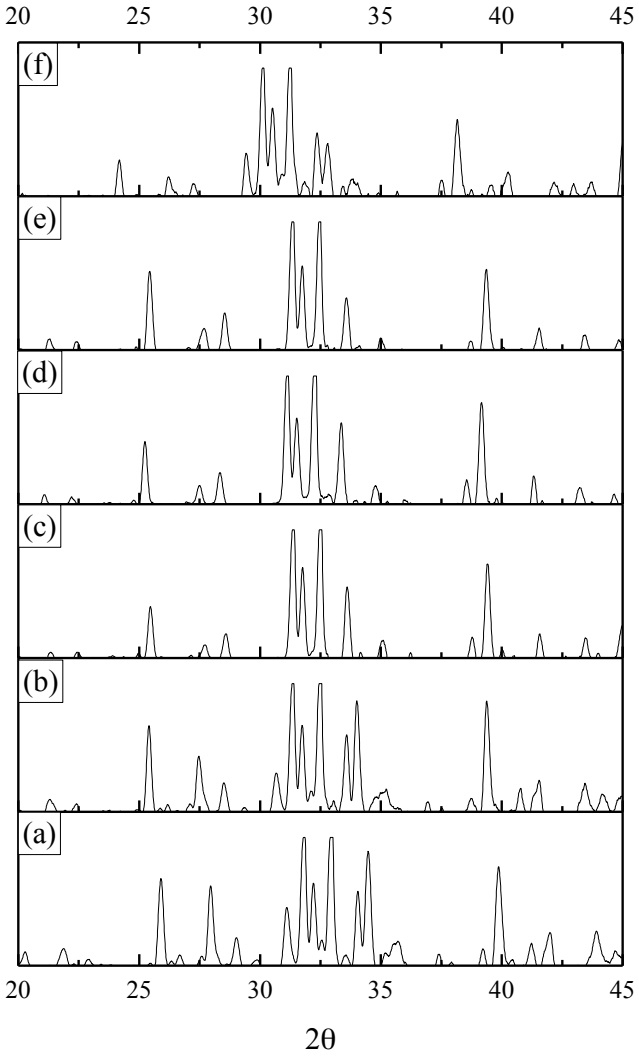

Figure 3.12: This XRD spectrum is for Group #1: 100% HA and is a comparison among the six (6) time points *in vitro*: (a) Initial, (b) 1 day, (c) 7 days, (d) 14 days, (e) 21 days and (f) 28 days.

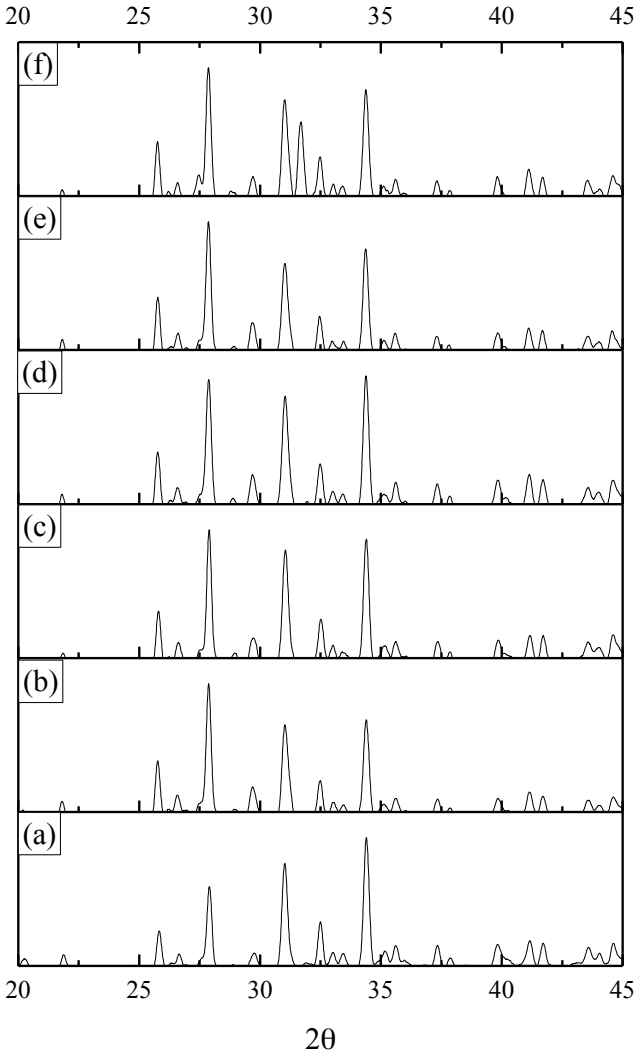

Figure 3.13: This XRD spectrum is for Group #2: 100% β-TCP and is a comparison among the six (6) time points *in vitro*: (a) Initial, (b) 1 day, (c) 7 days, (d) 14 days, (e) 21 days and (f) 28 days

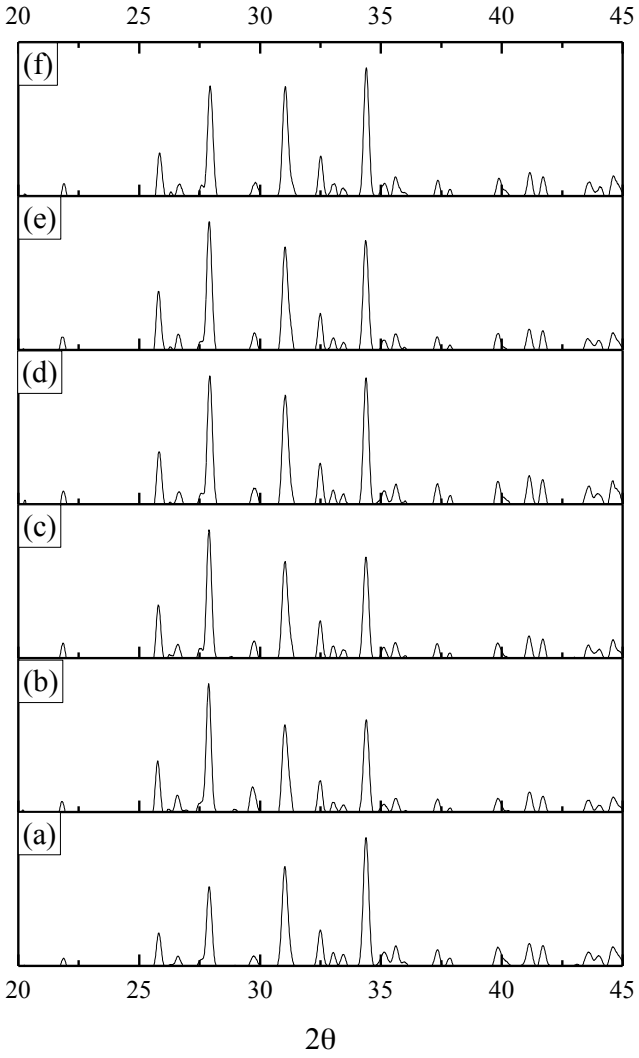

Figure 3.14: This XRD spectrum is for Group #3: 15/85% HA/β-TCP and is a comparison among the six (6) time points *in vitro*: (a) Initial, (b) 1 day, (c) 7 days, (d) 14 days, (e) 21 days and (f) 28 days

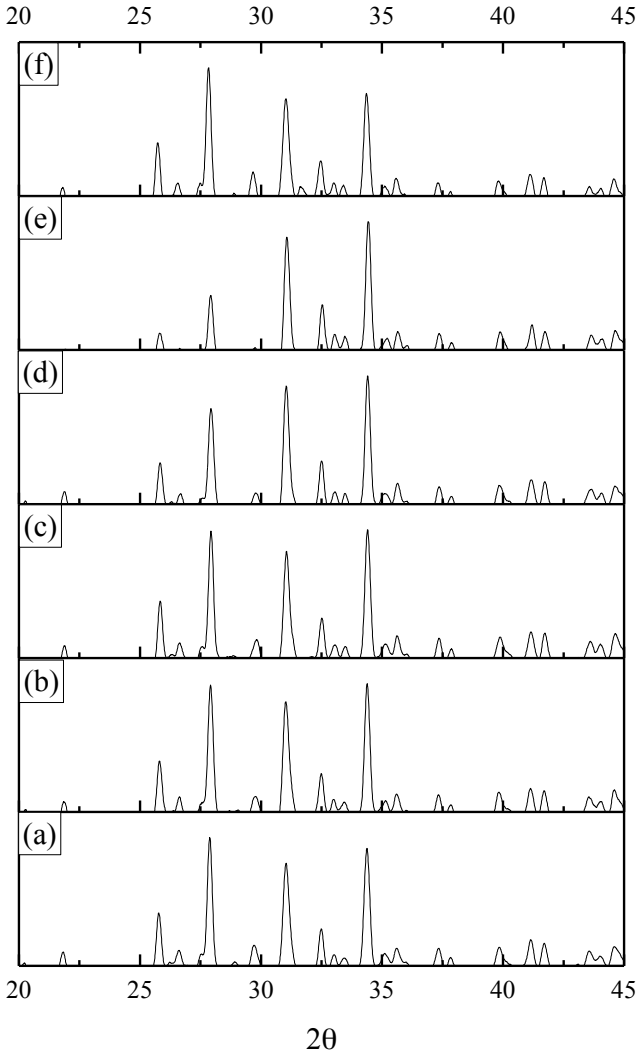

Figure 3.15: This XRD spectrum is for Group #4: 15/85% HA/β-TCP (design) and is a comparison among the six (6) time points *in vitro*: (a) Initial, (b) 1 day, (c) 7 days, (d) 14 days, (e) 21 days and (f) 28 days

The 100% HA and 100% β-TCP materials from both the raw form and post sintered to 1100°C were subjected to the Rietveld analysis using MAUD program for crystalline phase quantification. The crystalline phases present in the raw materials, as-received, are represented above and the phase fraction mean and 95% confidence interval are listed in Table 3.12 along with a visual bar graph seen below in Figure 3.16.

Phase ↓	Raw Material →	HA	β-TCP
%HA (±95%CI)		99.12[a] (±0.004)	0.017[e] (±0.03)
%β-TCP (±95%CI)		0.87[d] (±0.004)	90.03[b] (±2.96)
%Calcium Pyrophosphate (±95%CI)		0.00[e] (±0.00)	9.11[c] (±2.98)
%Calcium Oxide (±95%CI)		0.00[e] (±0.00)	0.84[d] (±0.10)

Table 3.12: Table indicating the percentage of each phase present in the raw materials as-received from the company. The standard deviations are listed in parentheses. The letters depict statistically homogeneous groups within each phase between all groups evaluated.

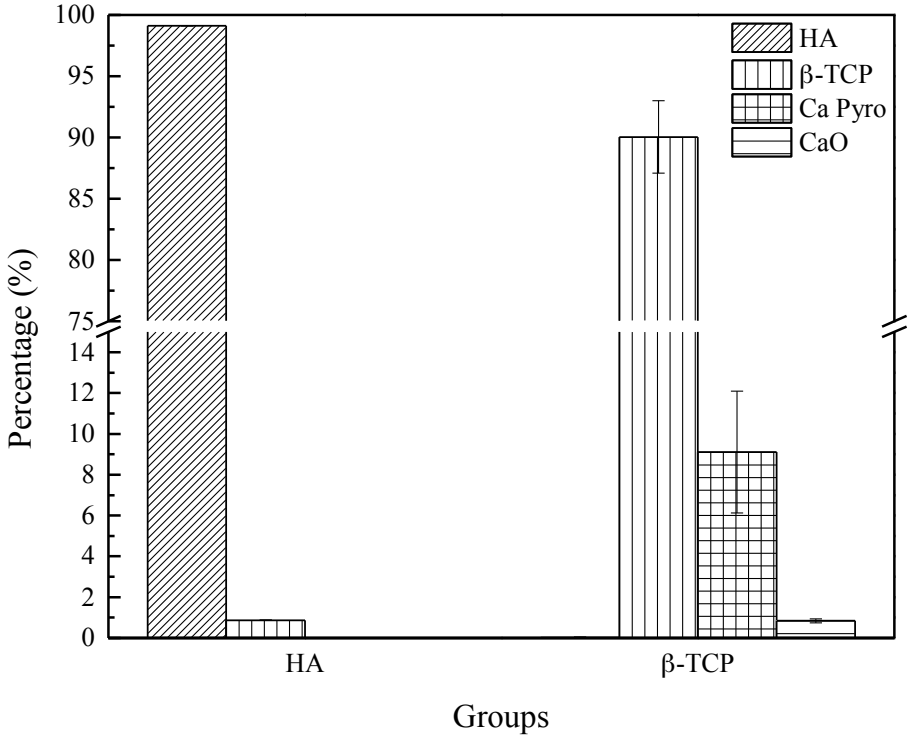

Figure 3.16: Percentage of each phase (HA denoted using diagonal lined bars, β-TCP hatched filled bars, and calcium pyrophosphate (Ca Pyro) in boxed bars, and calcium oxide represented with solid black bars). The raw materials prior to calcination as-received from company.

The EDS was completed to evaluate the Ca/P ratio for scaffold materials of 100% HA, 100% β-TCP, and 15/85% HA/β-TCP. The ANOVA statistics summary is presented in Table 3.13 and Figure 3.17. The Ca/P ratios observed for the different groups were similar to what was expected aside from 100% HA, which seemed to be slightly on the lower end of the atomic value

of ~1.67. The EDS was done as a supplemental quantitative measurement on the primary sample groups. These values should not be taken as an estimate instead of final average of the groups; a better representation for the Ca/P ratio can be given by using inductive coupled plasma (ICP).

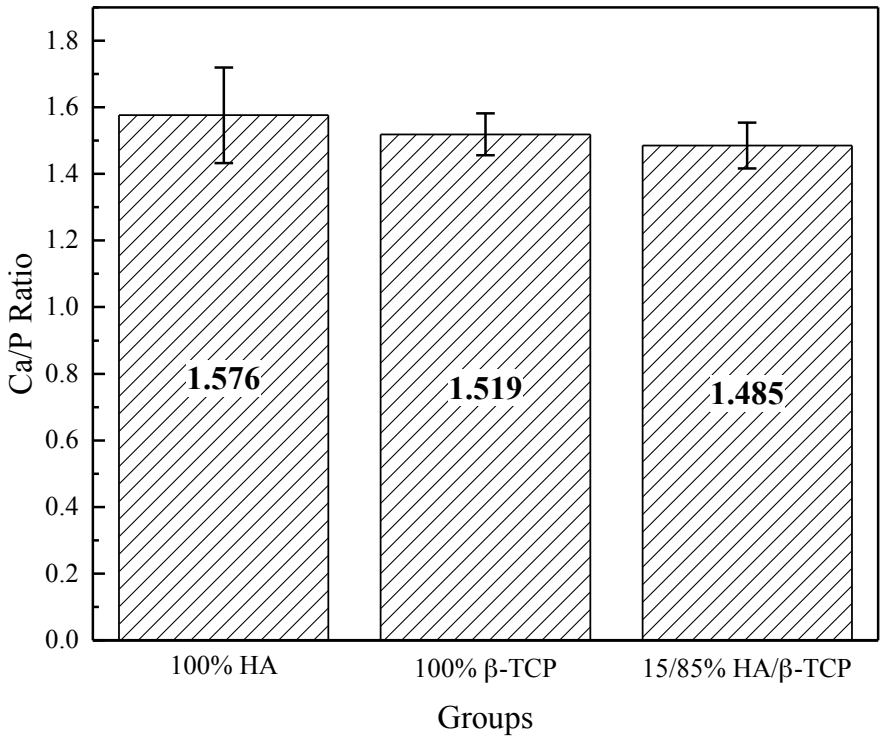

Figure 3.17: Mean ± 95% confidence intervals for Ca/P ratio of the experimental groups.

Group	Mean	Lower Limit	Upper Limit
100% HA	1.58	1.46	1.78
100% β-TCP	1.52	1.40	1.58
15/85% HA/β-TCP	1.49	1.37	1.58

Table 3.13: Mean ± 95% confidence interval for the Ca/P values of the three primary groups.

3.4.4 Fourier Transform Infrared Spectrometer (FT-IR)

FT-IR was executed to explore the chemical groups molecular vibration, primarily due to the advantage of vibrational spectroscopies over XRD is the identification of fine structural details, especially those of apatites, such as the location of carbonate species on the different sites of the apatite structure, the presence of PO_4^{3-} species, and at some instances the quantification of

the amount of OH^- ions [85-87]. FT-IR allows for the identification of most calcium phosphate phases. This method focuses on using the internal vibrational levels of molecules and ions, which may vary according to the short-range environments of these molecules, or ions. Phosphate (PO_4), carbonate (CO_3), hydroxide (OH) ions, and water (H_2O) molecules are the main groups detected by FT-IR. The PO_4^{3-} group has four main vibrational domains: ν_1(at about 950 cm^{-1}), ν_2(400–470 cm^{-1}), ν_3(1000–1150 cm^{-1}), ν_4(500–620 cm^{-1}). While carbonate ions, have four main vibrational domains as well: ν_1(~1050 cm^{-1}), ν_2(820–900 cm^{-1}), ν_3(1400–1550 cm^{-1}), and ν_4(650–750 cm^{-1}). Carbonate ions are always present in biological apatites and they may occupy different types of sites. With respect to the OH^- ion, there is only one vibrational domain corresponding to the stretching of the O−H bond (3400–3650 cm^{-1}). However, a signal line, corresponding to a rotational energy level of the ion in the lattice, is also observed (630–750 cm^{-1}). OH^- bands are essentially detected in apatites and related compounds. The OH^- stretching and movements are extremely sensitive to hydrogen bonds, and it has been previously shown in apatites that the OH bands can be considerably shifted away from their position in HA. Table 3.14 below gives a better summary of indicative peaks, which are relevant in the FT-IR spectra, with phases of importance. The most characteristic chemical groups in the FT-IR spectrum for HA are PO_4^{3-}, OH^-, CO_3^{2-}, and at seldom HPO_4^{2-}. Figure 3.18a-d presents FT-IR spectra of four experimental groups sintered to 1100°C.

Chemical group and phases	Adsorption bands (cm^{-1})
CO_3^{2-}	875; 1385; 1419; 1457
OH^-	632; 3572
PO_4^{3-} (β-TCP)	435
PO_4^{3-}	1046; 1091
PO_4^{3-} (HAp)	472; 570; 602; 963
PO_4^{3-} (β-TCP)	944; 971; 1127
$P_2O_7^{4-}$	725; 1210

Table 3.14: Location of FTIR adsorption bands (cm^{-1}) of certain phases and groups [85].

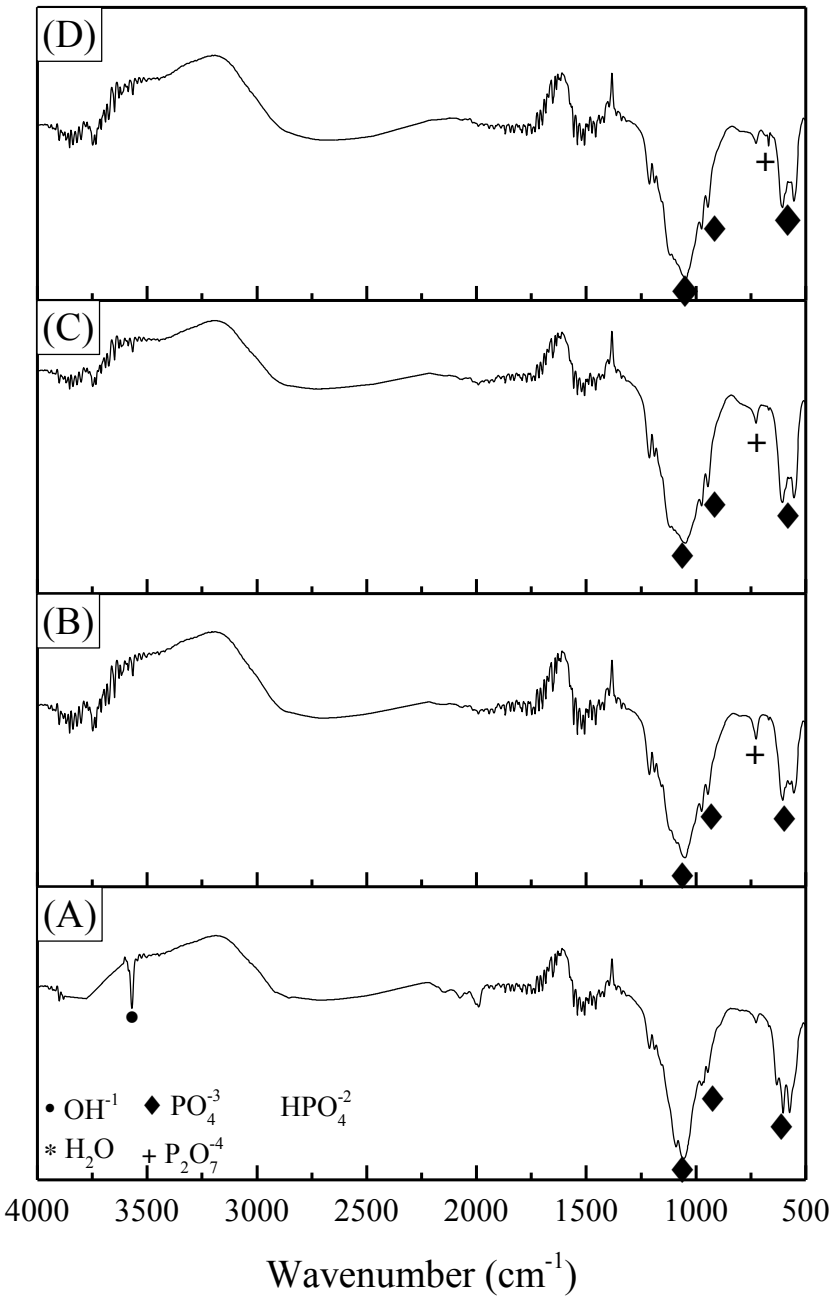

Figure 3.18: The FTIR spectra are shown for the four experimental groups (a) 100% HA, (b) 100% β-TCP, (c) 15/85% HA/β-TCP, and (d) 15/85% HA/β-TCP (design)

3.4.5 Differential scanning calorimetry (DSC) and Thermogravimetric analysis (TGA)

Using the DSC to verify whether any transformation was taking place, revealed two peaks (one endothermic and one exothermic) in all four experimental groups (Figure 3.19). The first as seen in Figure 3.19 below, is one around 100°C, which is indicative of the water boiling off from the material. The second peak, exothermic, is located at ~ 300°C, this is most likely indicative of other polymeric materials being removed from the colloidal gel.

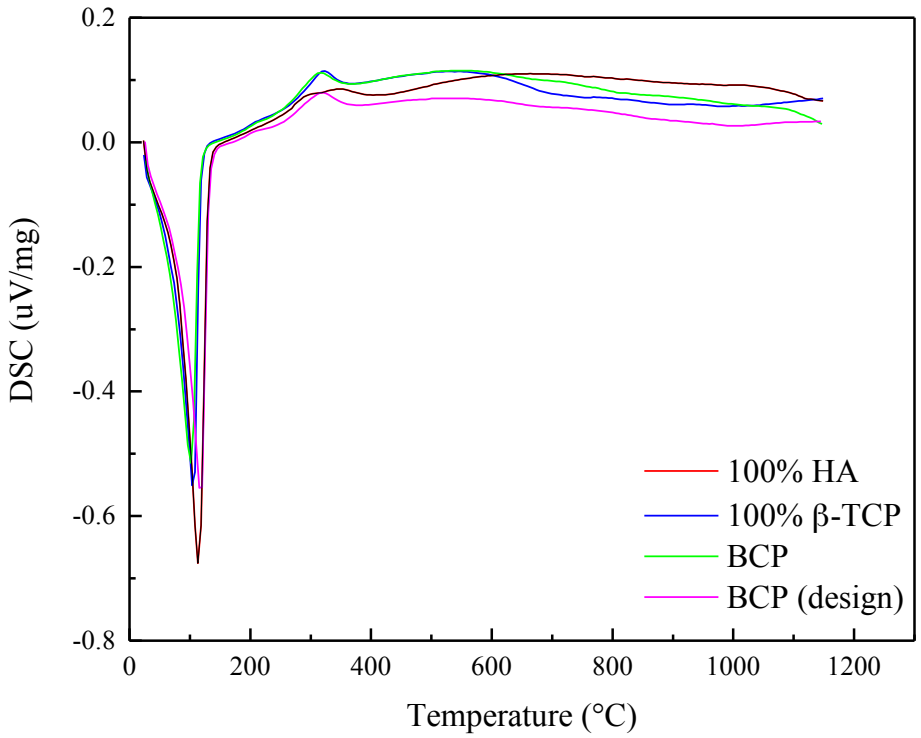

Figure 3.19: The above differential scanning calorimetry spectrum, is a comparison of the four experimental groups: (1) 100% HA – red; (2) 100% β-TCP – blue; (3) 15/85% HA/β-TCP – lime; and (4) 15/85% HA/β-TCP (design) – pink. The circles highlight from left to right the endothermic and exothermic peaks, respectively.

TGA results of as-dried colloidal gels are shown in Figure 3.20. The pre-drying of the ink in air evaporates any residual water from the green structure and the remaining components in the initial state are the ceramic particles, Darvan 821A® dispersant, the F4M viscosifying agent, and PEI. The TGA data indicates that burnout of the remaining material begins at ~75°C in air as a decrease can be seen in the data. Loss of weight in the range from ~100°C to 150°C is presumed to be due to decomposition of polymeric additives. The calculated weight fraction of ceramic gels in dried form is w_{solids}=~0.70. The weight loss becomes steady beginning around 200°C and remains consistent to the ultimate sintering temperature of 1100°C. The 100% HA

group, as can be seen in Figure 3.20, has the most loss, based on percentage (%), due to the fact that when the colloidal gel was fabricated it had the lowest solids fraction value at ~ 40%.

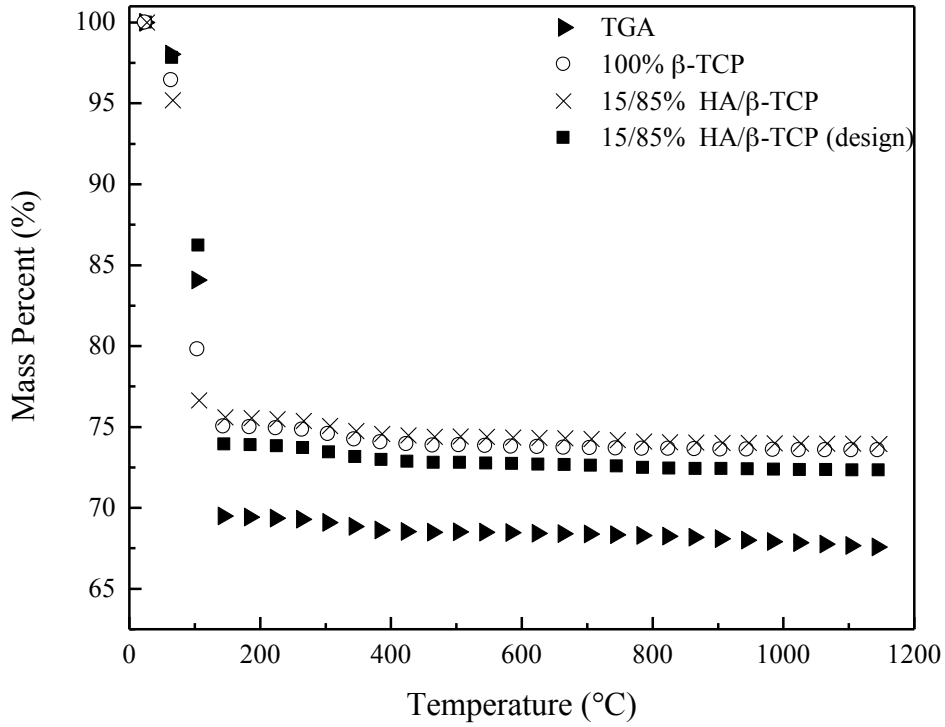

Figure 3.20: Thermogravimetric analysis graph above, gives a comparing of the four groups: (1) 100% HA –►; (2) 100% β-TCP –○ ; (3) 15/85% HA/β-TCP –×; and (4) 15/85% HA/β-TCP (design) – ■. The 100% HA shows the largest, nearly losing 30% of its mass during the process.

The data from the DSC and TGA analysis was plotted together to give a better visualization of what is occurring while materials are being 'burned' off during the sintering process. As can be seen in Figure 3.21A-D, the initial drop at approximately 100°C, where water would boil, there is also a significant endothermic peak. While in all of the experimental groups there is an exothermic reaction taking place at ~300°C, which can be seen in both Figure 3.19 and Figure 3.21. Figure 3.19 gives a better representation as showing an overlay of all experimental groups along with a better scale, shows that there is a slight difference in intensity among the groups with the 15/85% HA/β-TCP and 15/85% HA/β-TCP (design) group showing a similar trend, and the 100% HA showing the broadest exothermic peak, suggesting there may not be a significant reaction taking place.

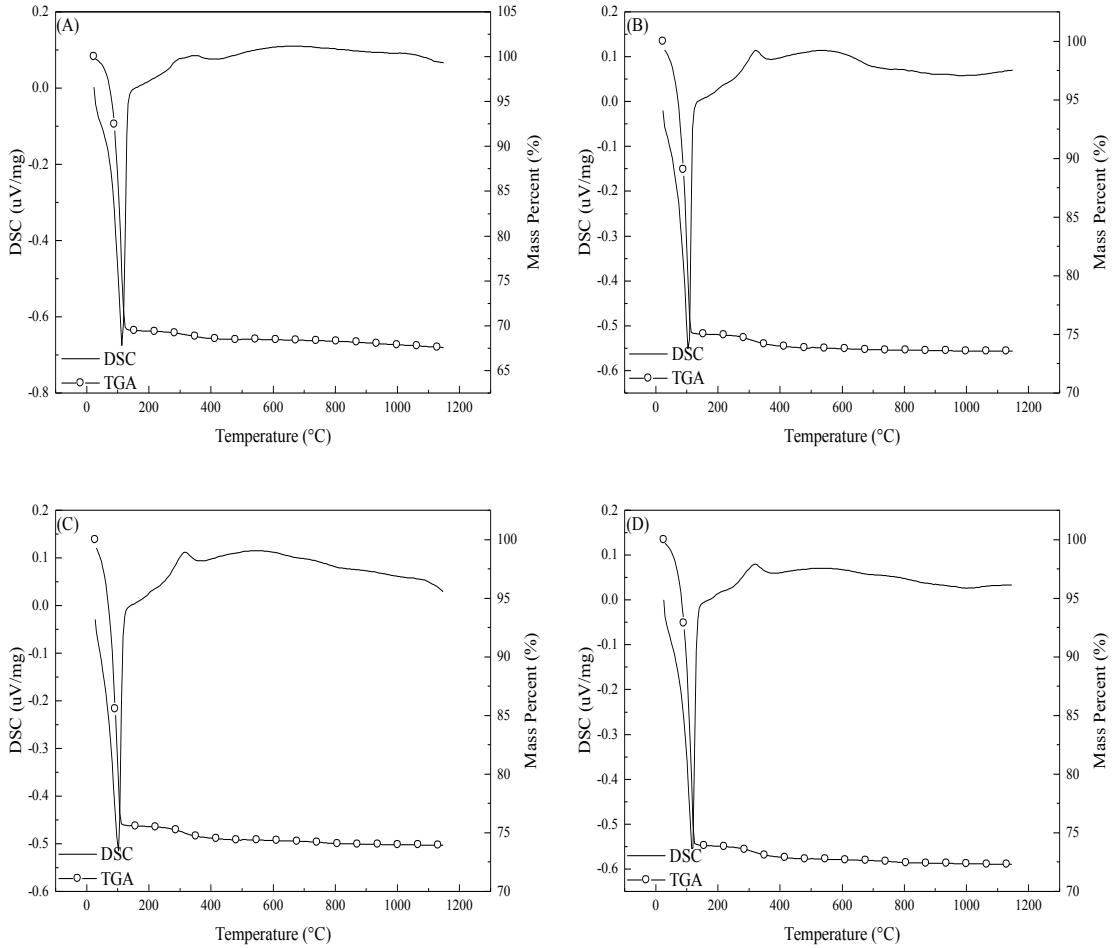

Figure 3.21: The figure above gives a representation and correlation between the DSC and TGA results for the four experimental groups: (A) 100% HA, (B) 100% β-TCP, (C) 15/85% HA/β-TCP, and (D) 15/85% HA/β-TCP (design).

3.4.6 Dissolution analysis

Immersion of bioactive glass in the SBF results in an initial partial dissolution of the material surface associated with a precipitation of a calcium phosphate that resembles the mineral phase of bone [88].

The initial dry and soaked weights of the four experimental group of samples: (1) 100% HA, (2) 100% β-TCP, (3) 15/85% HA/β-TCP and (4) (3) 15/85% HA/β-TCP (design) are listed below in Table 3.15. When comparing the two states of scaffolds (1) dry and (2) soaked, a $p<0.001$, was observed indicating a statistical significance. Within the states the only statistical significance was that the 100% HA scaffolds were statistically ($p<0.05$) different in comparison to the other three experimental groups (100% β-TCP, 15/85% HA/β-TCP and 15/85% HA/β-TCP

(design)). All percentages (%) reported are those compared to that of the weight of samples soaked for ~1 hour.

	Dry		1 hour soak	
Experimental Group	Mean	S.D.	Mean	S.D.
100% HA	0.083	±0.003	0.104	±0.005
100% β-TCP	0.098	±0.001	0.112	±0.004
15/85% HA/β-TCP	0.097	±0.001	0.110	±0.002
15/85% HA/β-TCP (design)	0.096	±0.001	0.109	±0.002

Table 3.15: Initial Weights of scaffolds used for the *in vitro* experimentation, both the dry scaffolds and those soaked in SBF for ~1 hour.

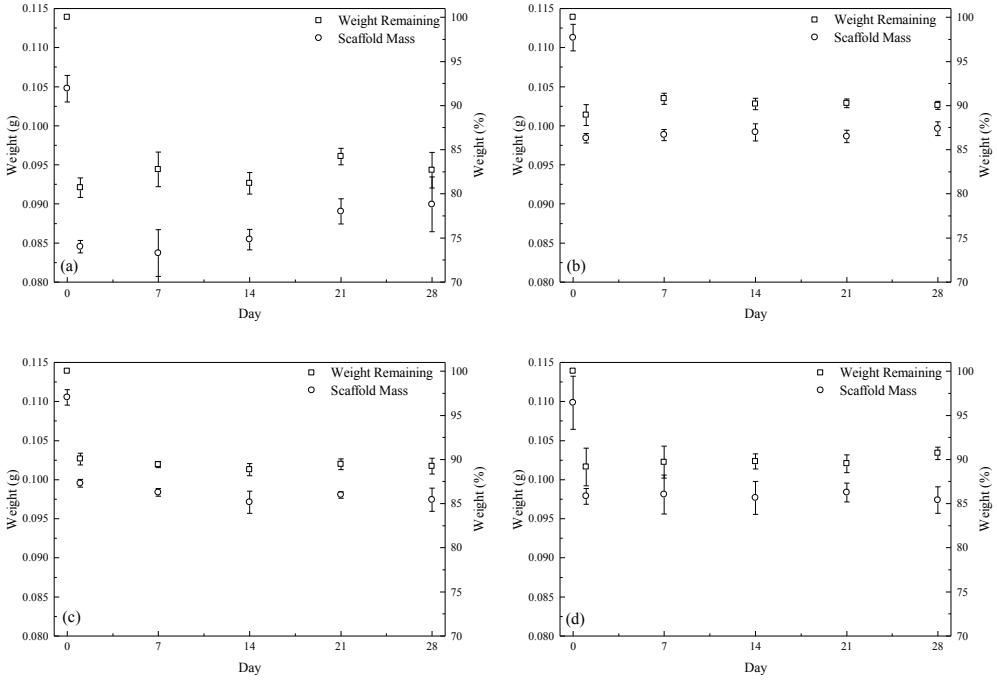

Figure 3.22: The above plots are graphs for the amount of weight (g) remaining after *x* days *in vitro* and the corresponding weight percentage remaining for the experimental groups: (a) 100% HA, (b) 100% β-TCP, (c) 15/85% HA/β-TCP and (d) 15/85% HA/β-TCP (design).

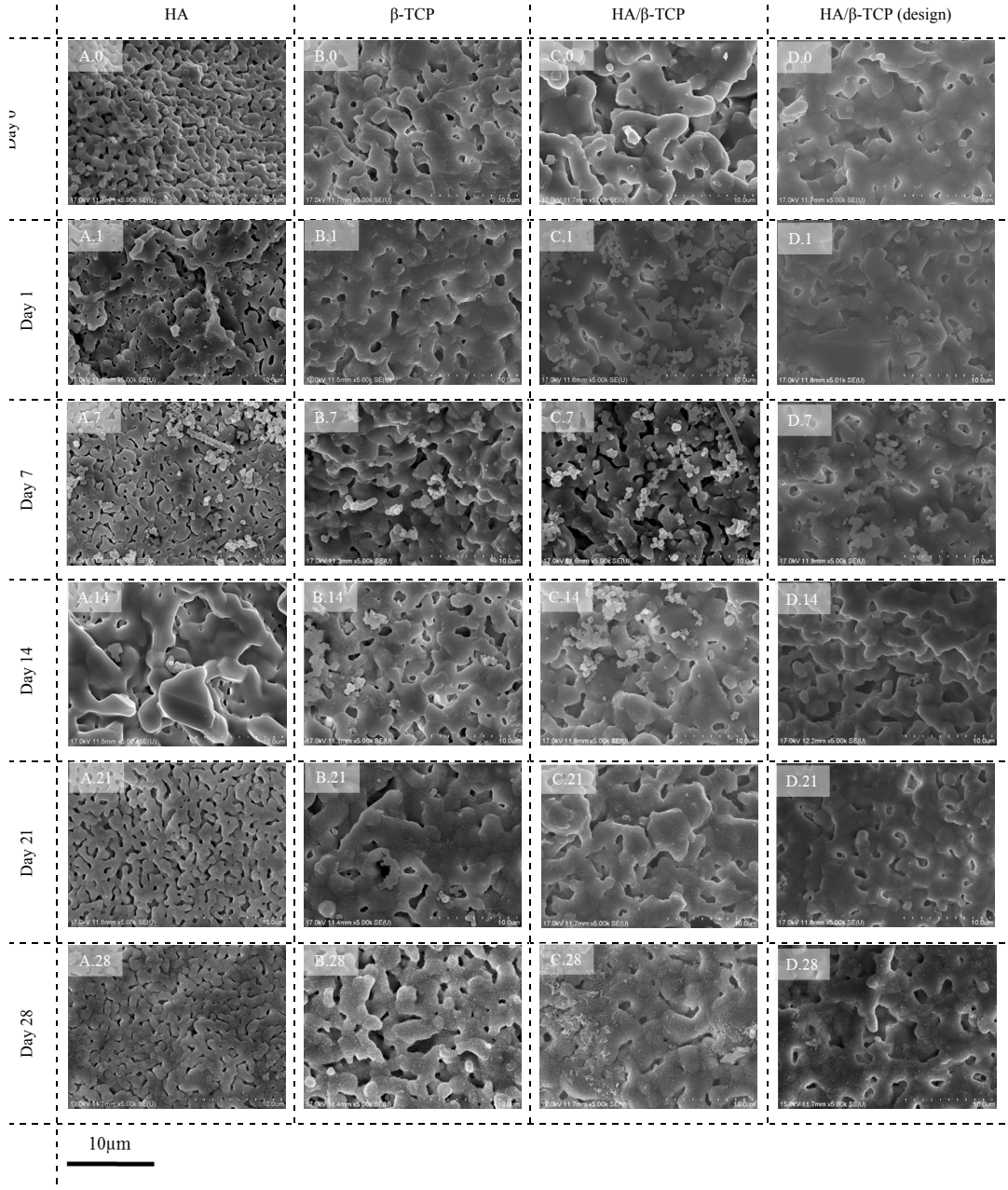

Figure 3.23: The above image is a matrix of the experimental groups post *in vitro*. The columns represent the material while the rows give the time point of the submerged *in vitro* time line.

Day (#)	1		7		14		21		28	
Experimental Group	Mean	S.D.	Mean	S.D.	Mean	S.D.	Mean	S.D.	Mean	S.D.
100% HA	80.71%	±0.01	82.77%	±0.02	81.18%	±0.01	84.24%	±0.01	82.69%	±0.02
100% β-TCP	88.92%	±0.01	90.78%	±0.01	90.18%	±0.01	90.25%	±0.01	90.04%	±0.00
BCP	90.06%	±0.01	89.42%	±0.00	88.86%	±0.01	89.47%	±0.01	89.25%	±0.01
BCP(design)	89.16%	±0.02	89.70%	±0.02	89.78%	±0.01	89.52%	±0.01	90.71%	±0.01

Table 3.16: The above table gives the percentage (%) of materials remaining after set number of days *in vitro* (PBS solution). The standard deviation (S.D.) is listed in % units. (BCP=15/85% HA/β-TCP).

3.5 Conclusion

The present aim (Aim #1) concentrated on the qualitative analysis of the BCP ceramic which is primarily used for the regeneration of bone. This aim focused on four general groups: (1) 100% HA, (2) 100% β-TCP, (3) 15/85% HA/β-TCP and (4) 15/85% HA/β-TCP (design). The work was partial based on preliminary work done by group of authors (Witek *et al* 2011) focusing primarily on the bulk properties of 15/85% HA/β-TCP rods. The material processing and subsequent colloidal gel fabrication was based on work done by Smay *et al*, and detailed in the methodology. The scaffolds chosen here were of similar dimension and pore size of previous *in vitro* and comparable *in vivo* studies, allowing for near direct comparison of results. The first steps of the characterization process were performed to verify, proper properties were achieved post sintering process (e.g., density).

Porosity evaluation performed with helium pycnometry demonstrated that porosity decreases linearly from the green state scaffolds that were subjected to 900°C. When the sintering temperature was increased to 1100°C, a decrease in porosity was observed followed by a significant increase in porosity when sintering temperature was raised to 1250°C. The porosity results are in agreement with the scanning electron micrographs, which showed more open structures for samples sintered to 1250°C.

Following the density experimentation, initial XRD scans were completed of the four groups to obtain their respective spectra. These initial spectra were considered to be the baseline to compare them to the subsequent spectra post *in vitro* experimentation period of four weeks. The XRD spectra for the green state showed HA and β-TCP peaks for each in their respective experimental group. Such observations were validated through phase quantification by Rietveld refinement where a substantial fraction of calcium pyrophosphate was observed following calcination at ~10%. When phase transformation/evolution as a function of sintering temperature for materials was evaluated utilizing the green state phase fraction as baseline, a decrease in the

amount of HA from ~11% to less than 1% was along with a proportional increase in the amount of β-TCP and minimal changes in the amount of CPP ($Ca_2P_2O_7$) was observed. The functional group OH^- in HA is possibly eliminated by a process called dehydration at a relatively high sintering temperature (~1100°C), but simultaneously while some of the HA is decomposing and forming into α-tricalcium phosphate (α-TCP), β-tricalcium phosphate (β-TCP) and tetracalcium phosphate ($Ca_4(PO_4)_2O$) (TTCP) [89, 90]. When the scaffolds were dehydroxylated via sinterting process, the HA lost OH^- radicals upon heating [91] and longer hold times (≥ 4 hours) applied according to the Equation (3.5.1) [92, 93]. The hydroxyl ion-deficient product $Ca_{10}(PO_4)_6(OH)_{2-2x}O_{2\square x}$, is known as the oxyhydroxy-apatite, which is from research is known to form around 900°C [90].

$$Ca_{10}(PO_4)_6(OH)_2 \rightarrow Ca_{10}(PO_4)_6(OH)_{2-2x}O_{2\square x} + xH_2O\uparrow \quad (3.5.1)$$

The chemical assessment to quantify Ca/P ratio or further verify the compositions of starting materials at the three various stages of colloidal ink development. The theoretical Ca/P ratio for pure HA, β-TCP, and calcium pyrophosphate are 1.67, 1.5, and 1, respectively [94]. The ICP results obtained are not in 100% direct agreement with the theoretical Ca/P ratios of HA and β-TCP. The bulk raw form of HA had Ca/P value of 1.598, approximately 5% lower than that of the theoretical 1.67, while the β-TCP material was about 10% lower from its theoretical Ca/P value of 1.5. That leads to the conclusion that the β-TCP material utilized in this work, is calcium deficient thus further confirming the shifting of phase percentages remaining after the sintering process. Additionally with the results of the ICP indicating the Ca/P values below the theoretical value lead to the molar ratio shifting away from 5/3 and 3/2 of Ca to P for the HA (Equation (3.5.2) and β-TCP (Equation (3.5.3), respectively, having a stoichiometric formula as seen below:

$$Ca_{4.79}(PO_4)_2(OH) \quad (3.5.2)$$

$$Ca_{2.72}(PO_4)_2 \quad (3.5.3)$$

The presence of the rapidly dissolving low stoichiometry phases such CPP is typically not detrimental to the initial host to grafting material response. Since the amount of secondary phase determined by Rietveld refinement was considerable (~10%), its initial rapid dissolution may enable further opening of the porous network, allowing the release of Ca and P to the wound-healing site along with larger diffusivity pathway for nutrients and oxygen, which are desirable features for osseoconduction. On the other hand, the release of large quantities of ions

at short periods of time may be detrimental or toxic to the dynamically changing cell populating the wound-grafting material [95, 96]. Although the chemical properties are an important for grafting purposes they are not the only important property to consider when tailoring scaffold materials to patient and/or sites. With respect to *in vitro* degradation analysis, there was no statistical significance among the four experimental groups. Therefore it can be concluded that even when taking CPP into consideration, does not necessarily make a dynamic difference, which can be further translated into *in vivo* situation under the same assumption. However, it should be taken into consideration that the presence of particles composed of two or more phases produced along with potential partial or full phase transformation may account for substantial changes in particle fusing, necking, and growth, thereby accounting for the observed microstructural evolution and kinetics [10, 97].

Following XRD and Rietveld analysis, material composition and chemical groups were further evaluated through Fourier Transform Infrared Spectroscopy prior to and after sintering. First, organic materials/remnants content was verified after calcination, and at both temperatures no organic content was present in the materials along with a low absorbance for H_2O after both calcination and all sintering regimens, suggesting this fabrication route would not have an effect on the physicochemical properties.

All the experimental groups (1) 100% HA, (2) 100% β-TCP, (3) 15/85% HA/β-TCP and (4) 15/85% HA/β-TCP (design) resulted in similar FTIR spectra, with exception of 100% HA. The group composed of 100% HA had the OH^- peak present, thus indicating one of the primary differences between the spectra. Additionally groups composed of the two phases, (i) HA and (ii) β-TCP, had peaks indicative of the CPP phase, and also lacked the definitive OH^- peak. These results are in agreement with phase quantification results, which were obtained from the XRD spectra.

The primary goal of this aim was achieved and further confirmed with multiple analyses. The phase transformation or as referred in conclusion of HA transforming to β-TCP and small amounts of CPP, has been of interest in past, not with regards to possibly being detrimental to the host but more so of the ever so 'disappearing' Ca^+ ion(s). The results have shown and confirmed the HA decomposed into β-TCP from 100°C, thus making it indicative that HA in not fully stable, with colloidal inks containing a high amount of β-TCP. It can be concluded that the presence of the TCP in composite colloidal inks is the stimulus for further decomposition of the HA phase through the process of dehydroxylation. So the primary reason for the often so none matching Ca/P ratio value was due to taking TCP's Ca/P theoretical value and not its experimental value.

Ca/P ratio is a relevant factor, as it is coupled to scaffold degradation once placed *in vivo*, so it will help better tailor the material, which ultimately becomes the scaffold.

Ultimately the fabrication of 100% HA, 100% β-TCP, or a combination of both, BCP, is done by the sintering of the biologic or synthetic apatite. The BCP composition after sintering is related to the calcium-deficiency of the not sintered apatite and then ultimately on the final sintering temperature. These calcium deficient apatites are sintered at or above 700°C following the reaction:

$$\underset{\text{(Calcium deficient apatite (CDA))}}{Ca_{10-x}M_x(PO_4)_{6-y}(HPO_4)_y(OH)_2} \rightarrow \underset{\text{(HA)}}{Ca_{10}(PO_4)_6(OH)_2} + \underset{\text{(β-TCP)}}{Ca_3(PO_4)_2}$$

The apatite is deemed to be calcium, Ca^{2+}, deficient when the Ca/P ratio is determined to be lower than the stoichiometric value. The *M*, in the formula is used to indicate other possible ions, which may show in the mixture.

Biodegration, the process that occurs when a material breaks down into its smaller components, reduces the complexity of the matrix system by 'eroding' the material. This process of degradation or resportion of the calcium phosphate material ultimately results in physical and chemical changes post introduction in to a biological environment, whether it be *in vitro* setting with fluids such as SBF or PBS, or implantation into the host. The most obvious changes to this scaffold and its subsequent material will start with the breaking of the scaffold into smaller particles, whether it is naturally or due to movement. With this being an issue the scaffold will endure a loss in its mechanical strength, and in due time it will incur a loss of density, as well as change in its porosity. These aforementioned changes ultimately have an effect on the scaffolds size, volume, and weight. With respect to the possible chemical changes, the local environment immediately around the implant its general vicinity may have a pH change which will facilitate the dissolution of the scaffold material. The degradation or resorption has been linked to the bioactivity of the calcium phosphate (CaP) materials, which compose the scaffold. These CaP materials, more specifically HA and β-TCP, have a unique feature to them, known as *bioactivity*. Bioactivity is defined as the ability to form a chemical bond with bone, which results in a bone-scaffold interface and eventually leading to the formation of bone at this interface. The dissolution properties of the CaP materials can be linked to their properties, which can include physical form, composition, crystal structure, and crystallinity. These are factors that are directly associated with the material, while other factors such as pH or solution composition will also play a role in the process. For example two scaffolds composed of 15/85% HA/β-TCP will have a

different dissolution rate if the density was altered to be different among them, i.e. the material with higher density will ultimately dissolve at a slower rate than that scaffold with a lower density. The calcium phosphate scaffolds composed of different materials or a combination of two, have different crystallographic structure, which results in different internal bond strengths, which are related to the solubility of the final 'product'. In certain instances even materials with the same composition but different structure, such as α-TCP and β-TCP, will vary in in their dissolution rate. The order of solubility of a few commonly used CaP materials in scaffold fabrication is as follows:

$$ACP \gg DCP > TTCP > \alpha\text{-}TCP > \beta\text{-}TCP \gg HA$$

(ACP = amorphous calcium phosphate; DCP = monetite, $CaHPO_4$; TTCP = tetracalcium phosphate, $Ca_4P_2O_9$; α- and β-TCP, $Ca_3(PO_4)_2$; HA = hydroxyapatite, $Ca_{10}(PO_4)_6(OH)_2$).

β-TCP has shown *in vitro* to dissolve at a faster rate in comparison to HA, while the dissolution of the biphasic calcium phosphate (BCP) is based on the ratio of HA/β-TCP, with higher amounts of HA in comparison to β-TCP, slowing the rate. In the past *in vitro* results have indicated that β-TCP was about 3 to 12 times faster in comparison to 100% HA. These monophasic or biphasic calcium phosphate ceramics are osteoconductive but not osteoinductive. These osteoconductive ceramics provide the necessary factors that allow for "vascular ingress, cellular infiltration and attachment, cartilage formation and calcified tissue deposition" [98, 99]. While the osteoinductive property of the materials' "stimulate uncommitted cells, such as mesenchymal stem cells, to convert phenotypically to chondroprogenetor and osteoprogenitor cells" [98-101]. Although in some instances the osteoinductuve property has been linked to BCP ceramics, which are implanted subcutaneously (under the skin). Even this has been observed in scaffolds composed of BCP material, in may not necessarily be linked its osteoinductive feature, but more along the geometry of the scaffold, with the incorporation of materials such as bone morphogenic proteins [25, 98, 101, 102].

The characterization of the calcium phosphate materials by appropriate methods cannot be overlooked for the proper interpretation of the *in vitro* and *in vivo* observations. In terms of characterization XRD, supplemented by FTIR analysis would be the preferred method. Characterizing by calcium to phosphate ratio alone without XRD and FTIR may give misleading results especially when investigating the possible various phases (e.g. HA + TCP, HA + TCP + CaO, etc). These CaP biomaterials, which are considered ideal candidates for bone replacement consist of HA, β-TCP, or combination of both. These materials posses the advantage of having the ability to controlled.

CHAPTER 4
CREATING A FUNCTIONALLY GRADED BIPHASIC CALCIUM PHOSPHATE (BCP) SCAFFOLD WITH THE UTILIZATION OF A NOVEL MIXING CHAMBER

4.1 Overview

Chapter 4 focuses the use of the 3D printer to build novel scaffolds for the potential bone replacement applications. The focus is to show the capabilities of the 3D printer and how it can create custom tailored scaffolds on the micro and macro scale. The work employs the use of alumina and zirconia to mimic the calcium phosphate system, as these two ceramics provide the ability to differentiate for a better analysis.

4.2 Introduction

Previously three basic periodic structures have been most widely assembled, including space filling layers, high aspect ratio walls, and spanning elements, as illustrated in Figure 4.1. Space filling volumes are built from solid layers requiring the deposited ink to be deposited in a pattern with no gaps between adjacent filaments. To create a space-filling layer with a centerline-to-centerline lateral (*x*-*y*) spacing of d, the layer-to-layer (*z*) spacing is $0.25 \cdot \pi \cdot d$, where d is the filament diameter. While, high aspect ratio walls need the deposited filament have lateral spacing >d. Spanning lattices have a lateral spacing of >d, but adjacent layers are rotated by an angle (typically 90°) and requires that the ink can bridge gaps in underlying layers. In these structures, spanning lattices are especially important due to the versatile applications in the areas of electronics [103-105], composites [105-107], and biological science [108].

Computer-aided design (CAD) and computer-aided manufacturing (CAM), technological advancements in 3D-printing in the form of robocasting, fused deposition modeling (FDM), and selective laser sintering (SLS) have allowed for the advanced control of bioactive ceramic scaffold shape, size, and porosity [41]. Among the various 3D printing methods, robocasting allows for the building of ceramic-based scaffolds without the need for a mold and requires very little polymeric binder [38]. Robocasting builds (*'prints'*) geometries by computer-controlled extrusion of colloidal pastes/gels (i.e., inks) [17]. 3D printing methods can produce a variety of structures using CAD/CAM programs [34] that are adapted to reproducing/constructing a variety

of structures from various image/file sources (i.e., CT scans) (Figure 4.2). One advantage of 3D printing is the ability to design specific shapes/objects to be used in bone replacement surgeries. The current state of the art 3D programs have produced a variety of designs, which have been produced with the SFF/RP system [11, 15, 41, 54, 109, 110].

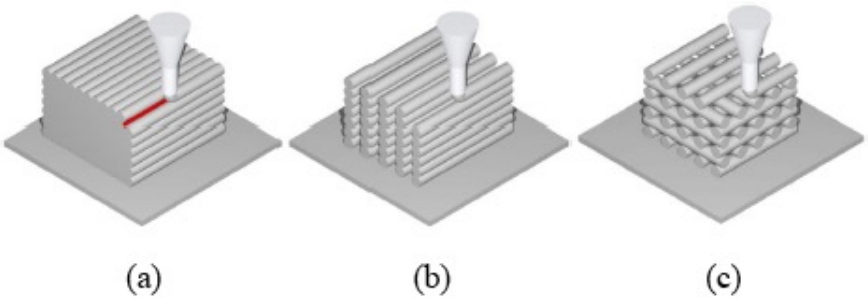

Figure 4.1: (a) space filling layers, (b) high aspect ratio walls, and (c) spanning elements [53].

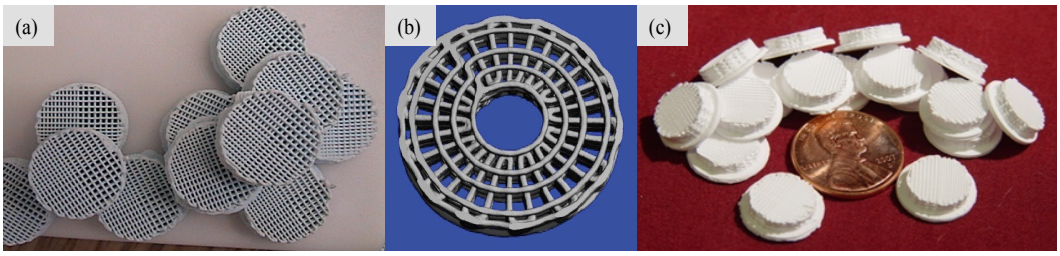

Figure 4.2: The images above represent a few examples of scaffolds, which can be fabricated using the robocasting system. (a) Represents a quadranted scaffold with 3 different pore sizes, (b) a CAD cross-section of a cylindrical scaffold [111] and (c) scaffolds with a cap, used for *in vivo* studies, to prevent from falling thru a circular defect.

An example of a design a 'robocasting' machines is represented in Figure 4.4. The system uses positive displacement syringe pumps to dispense the ink in a pattern controlled by the x-y-z gantry robot. For ceramics, the ink is typically deposited onto a ceramic substrate submersed in an oil bath. For silicone materials, the ink is deposited directly onto the substrate in air (for silicone material printing). For situations where HA/β-TCP scaffolds are desirable, the ink deposition must be done on a ceramic plate in an oil bath to prevent non-uniform drying [38].

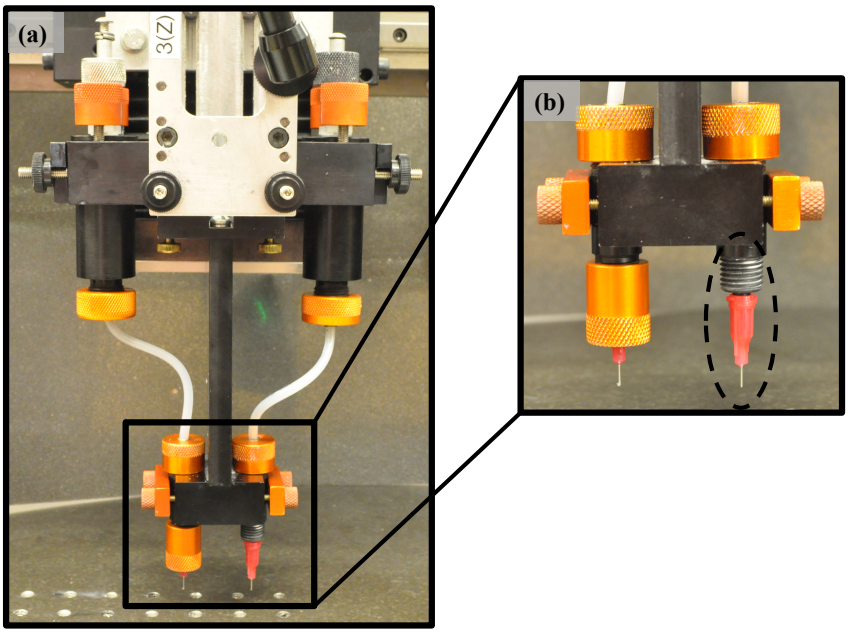

Figure 4.3: (a) Overall setup of the robocaster used for two-tip printing, (b) zoomed in image of the set up for the dispensing of the two "individual" materials. The dashed circular shape in (b) indicates how exchanging the printing tip can customize the size of the rods.

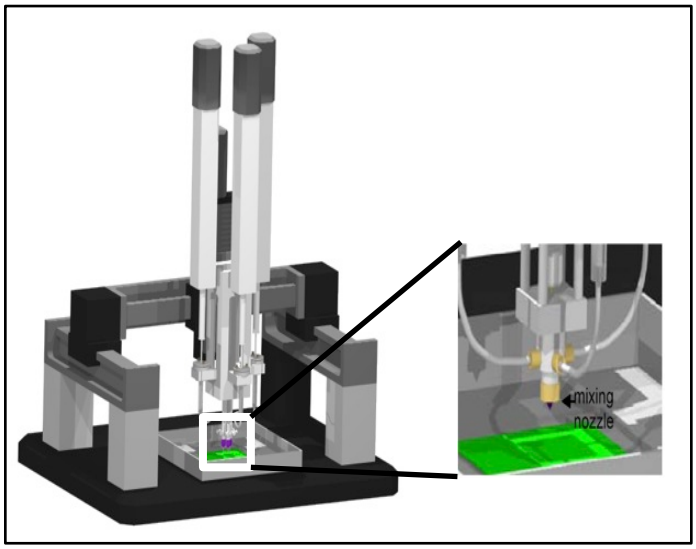

Figure 4.4: Schematic of robocasting machine currently in use at the Smay Lab Group (Oklahoma State University-Tulsa, Tulsa, OK), 3D Inks LLC (Tulsa, OK USA).

Colloidal ink suspensions can be tailored to a variety of specific needs ranging from the concentration of HA or β-TCP (e.g., 15/85, 20/80, 35/65, and 60/40) to the size/shape of the scaffold that needs to be manufactured to the particular patient defect. Therefore, such technique allows the possibility of unique chemistry arrangement within the structure, permitting further steps in bioactive ceramic material scaffold designing.

For example, from a macro-structural arrangement standpoint, robocasting of bioactive ceramic material rods allows distances between rods adjustment to be between 100μm and 1000μm, potentially altering the host response to the scaffold. Structural and within-material pore dimensions add another element to scaffold designing, as structural pore size influences vascularization. In addition, establishment of cellular content and pore size within the material component of the scaffold affects its mechanical strength while yielding dissolution properties influences the ability to tailor the scaffold for a specific application.

Depending on chemical composition and crystal structure, calcium phosphates exhibit different biodegradation rates *in vivo* (i.e., β-TCP>HA). When two different calcium phosphates are properly mixed and subsequently sintered together, a functionally graded material having the two phases of the different dissolution rates can be prepared.

The ultimate goal is to utilize the results from Specific Aim #1, to make sure that no unexpected phases arise during the degradation process, which can possibly be detrimental to the host. This will help in establishing the extremes of using the mixing ratio of the various materials to be utilized. As can be seen in Figure 4.5, two materials will be utilized to fabricate the structure. The syringe reservoirs, labeled material #1 and #2 are loaded with a 100% β-TCP or 100% HA, respectively, colloidal gel. The first goal was to successfully create a functionally graded lattice-based scaffold, with the manipulation of each respective material controlled in the CAD design. It is important to fully understand the mixing chamber and model it properly, using a CSTR design approach.

Using an advanced feature, such as a mixing chamber, the scaffold can be tailored and enhanced to a specific site and for the individual patient. When considering the multi (two)-tip technology currently being utilized to fabricate scaffolds, the variation in the scaffold is limited to interchanging between layers or mid layer (Figure 4.6a). With the use of an already developed feature such as the mixing chamber, one can fabricate a functionally graded scaffold, truly tailoring the compositions, to the one, which would be deemed necessary at that location in the lattice-based scaffold. The scaffold can be tailored in more of a 3D fashion as can be seen in Figure 4.6b. The adjustment of the speed of the motor in combination of the mixing motor can create different rationed material from a combination of 2 to 4 different materials.

This concept of mixing materials and co-extruding thru a single tip has been explored with a primitive mixing motor. The results with the utilization of the first version of the mixing motor although successful, resulted in bad ‘mixedness’, and additionally presented a long time to fully change over from one material. The delay to fully change over was seen and illustrated when printing silicone samples with red and blue dye as seen in Figure 4.8. As can be seen, in

the array, that the sample starts at the top row in each column, but there is some remaining material, still being extruded, it is not until the last (third) structure (bottom row) does one see the complete change over. With respect to the bad 'mixedness' that is shown in backscatter SEM micrographs as seen Figure 4.9, the mixing was not as uniform as it would be ideally. This can be seen with the brighter/lighter shades being representative of the $BaTiO_3$ material and the darker shades representing the $SrTiO_3$.

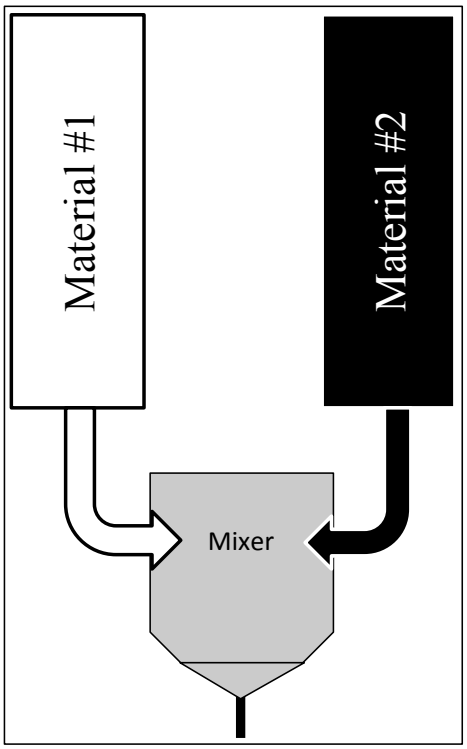

Figure 4.5: A schematic of the mixing nozzle (motor) to be used to mix to 100% colloidal gel pastes into a functionally graded structure (The mixer design is in Figure 4.12 and Figure 4.13).

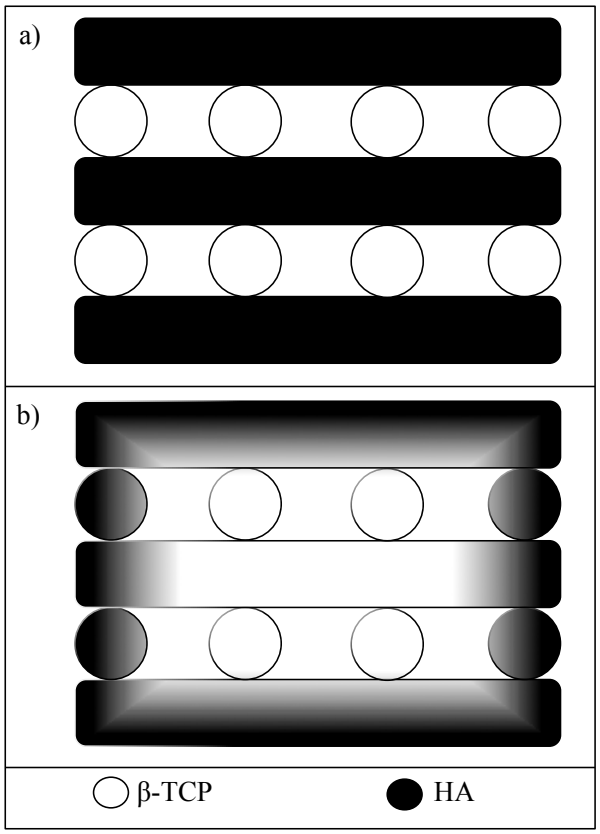

Figure 4.6: (a) A schematic of the graded structure, indicating the change of material in different layers; (b) The new proposed use of a mixing nozzle to create a graded structure, with a higher content of HA on the outside, with a higher content of β-TCP on the inside while moving towards the center of lattice-based scaffold.

Figure 4.7: Image showing a printed scaffold, using the multi-tip method, the two materials used were white and black silicone, and represents the schematic in Figure 4.6a.

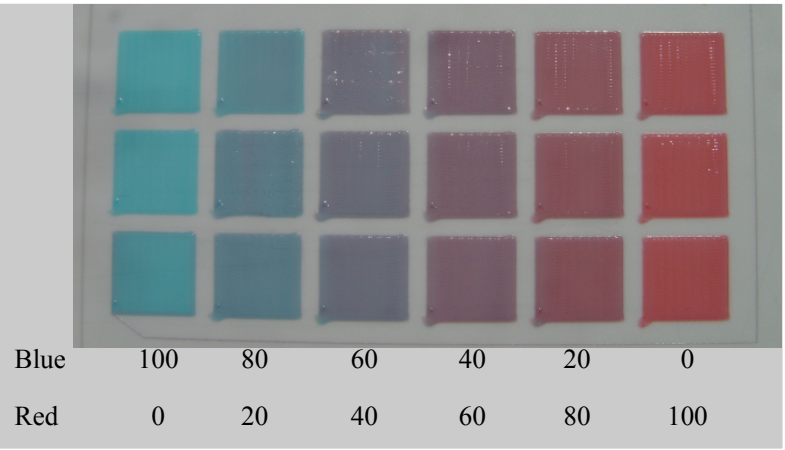

Figure 4.8: This array of silicone cubes represent the change over time, when co-extruding materials thru a single orifice. All of the cubes with their respective ratio of blue to red were started at the top and printed until completion.

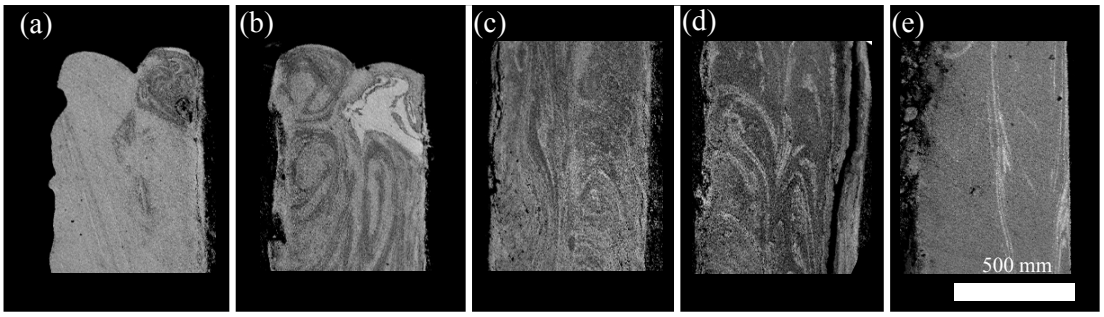

Figure 4.9: The backscatter SEM (B-SEM) images represent a mixture of two materials using the first mixing motor designed in the Smay lab. The binary array starts with a pure single material, (a) 100% $BaTiO_3$, and decreases 25% in each subsequent step (b) 75/25, (c) 50/50, (d) 25/75, and ultimately reaches the other pure material, (e) 100% $SrTiO_3$, being extruded [59].

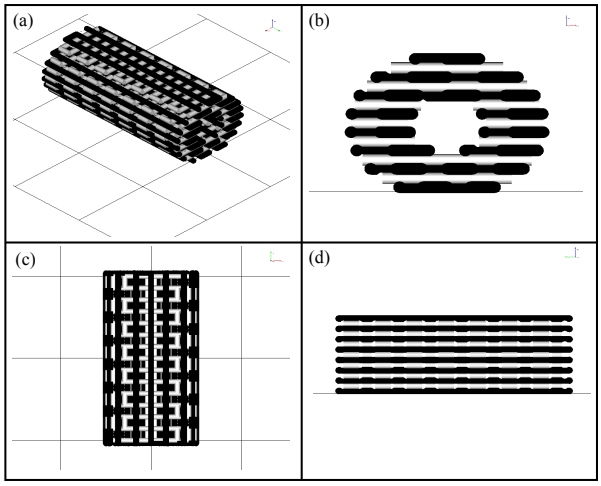

Figure 4.10: The above image gives a rendering of the CAD file, which was designed for a prototype experiment for a long bone study. This cylindrical scaffold was fabricated from two materials (white = material #1 and black = material #2). The image gives the reader four images to get a better visual understanding: (a) iso, (b) front, (c) top and (d) side.

In this specific aim, aluminum oxide (Al_2O_3) (also known as alumina) and zirconium dioxide (ZrO_2), referred to as zirconia, concentrated colloidal gels were used as model ink materials as they can differentiate in the SEM using backscatter mode. The Al_2O_3 and ZrO_2 powders used are high purity, sub micrometer-size, and relatively monodispersed. Al_2O_3 and ZrO_2 powders were dispersed into an aqueous suspension with the addition of polyelectrolytes, several critical factors such as the pH, the surface chemistry of powders, the degree of polyelectrolytes dissociation, the molecular weight of polyelectrolytes, and the adsorption of polyelectrolytes must be understood and controlled [112-115]. After the stabilized suspensions were fabricated, the gel-based inks were prepared by adding appropriate amount of flocculants. During the extrusion, the colloidal gel needed to sustain the creep deformation caused by the extrusion pressure, which was induced shear stress.

4.3 Experimental Section

4.3.1 Materials

Aluminum oxide (Al_2O_3) (AKP-30, Sumitomo Chemical Co., Tokyo, Japan) and Zirconia (ZrO_2) (TZ-3Y, Tosoh Corporation, Tokyo, Japan) powders were utilized, with their properties listed in Table 4.1, as the ceramic phase.

	Al_2O_3	ZrO_2
Mean Particle Size *(μm)*	0.32	0.04
Specific Surface Area *(m^2/g)*	7.10	16.0
Density *(g/cm^3)*	3.97	6.05

Table 4.1: Basic properties of aluminum oxide (Al_2O_3) and zirconia (ZrO_2).

4.3.2 Colloidal Gel Fabrication

Concentrated Al_2O_3 and ZrO_2 colloidal gels were prepared following a similar multi-step procedure as in Specific Aim #1. First, Darvan 821A® (Darvan 821A®, R.T. Vanderbilt Co., Norwalk, CT), de-ionized water, and Al_2O_3 or ZrO_2 powders were added sequentially into a 250 mL sample cup containing ~25 grams of 3 mm diameter zirconia milling media. The blend was mixed for 3 min in a non-contact mixer (Thinky AR-250; Thinky, Tokyo, Japan) to obtain a highly concentrated colloidal suspension. Next, hydroxypropyl methylcellulose (Methocel F4M, Dow Chemical Co., Midland, MI), a 5 wt% stock solution, was added at a 7 mg/mL aliquot followed by mixing for 90 seconds. The suspensions were gelled with the addition of the flocculent, nonlinear polyethyleneimine ($PEI_{50\text{-}100k}$) (with M_W=50,000~100,000, Sigma-Aldrich, St. Louis, MO) 10% by weight solution. In this specific aim the colloidal inks were fabricated with a solid fraction of ϕ_{solids}=~0.47. All samples were prepared in de-ionized water having a nominal conductivity of 5×10^{-4} $\Omega^{-1}\cdot cm^{-1}$.

4.3.3 Viscoelastic property measurement

Al_2O_3 and ZrO_2 colloidal gels were compared to the BCP colloidal gel that is prepared by polyelectrolyte induced bridging-flocculation [10, 59, 116]. The rheological properties are measured using a controlled stress-strain rheometer (C-VOR 200, Bohlin Instruments, East Brunswick, NJ) fitted with a C14 cup and bob geometry (cup diameter = 16mm, bob diameter = 14mm) with serrated walls to prevent wall slip. Pre-conditioning of the samples was performed. For each measurement, a sample of 3.6 mL of colloidal gel is loaded into the measuring system and subjected to 30 min oscillatory pre-shear at 1Hz with a controlled shear stress at 0.02Pa. After pre-shear, the sample is kept undisturbed 30min for equilibrium. All measurements are conducted at 25°C and a cover plate with filled water reservoir is used to minimize evaporation.

The shear elastic modulus (G') is measured in oscillatory mode, where the stress amplitude is logarithmically increased from 1 to 2000Pa at an angular frequency of ω = 1Hz. The yield "critical" stress (τ_y) of the gel is taken as the stress magnitude where G' drops to 90% of the maximum value during a stress sweep experiment starting from low stress. The second set of

experiments measures the flow curve of carbon black gel. In viscometery mode, the shear stress (Pa), τ, is recorded as a function of shear rate, ($\dot{\gamma}$) in an ascending series of discrete steps (0.001 ~ 100s^{-1}) with a 1-minute equilibrium at each step.

4.3.4 Fabrication of graded scaffolds (via two-tip method)

Robocasting uses a gantry robotic control machine (Aerotech Inc., Pittsburgh, PA) to extrude colloidal ink through fine nozzles. Printing was done with two materials (e.g.: colloidal inks or silicone). The two-tip method was done out by using a separate nozzle for each material. The printing parameters were set in the design of the structure. The ink delivery system is mounted on a *z*-axis mounted controlled stage for printing on a stationary platform. The 3-axis (*x*-*y*-*z*) motion is independently controlled by a custom-designed, computer aided program RoboCAD (RoboCAD 4.2, 3D Inks LLC, Tulsa, OK). Once a layer is '*printed*', the gantry was translated up (Δz) in the *z*-axis and the syringe is translated to with respect to the *x*-*y* axis, to allow for the printing of the secondary material, with the change between syringe #1 and #2 occurring at pre determined geometrical locations as designed in the program per the design. This process is repeated until entire scaffold is printed. This Δz distance is a function of the deposition nozzle diameter (D) and for all structure design parameters the following correlation was used: in this project, a Δz of $(\pi/4)\cdot D$. The colloidal gel exits the nozzle as a continuous, rod-like filament due to its rheological properties, which also aid in shape retention, allowing the rods to fuse together at points where they are in contact. Interruptions of ink flow (e.g. air bubbles, clogs, etc.) during fabrication are not desirable. Start-stop events were avoided as much as possible, but as this was a two-tip method, it was necessary when a change in tip (material) was indicated in the design parameter.

4.3.5 Fabrication of mixed-material scaffolds (via mixing chamber)

Stock inks of the prepared pure ceramics were loaded into individual reservoirs and then co-extruded through a mixing chamber to form samples with desired compositions by controlling the flow rate ratios of the two inks through the deposition nozzles. Figure 4.11 shows a schematic for the intended application where a binary array is illustrated. The ends in the array represent the two pure ceramic compositions and in between there is a systematic variation in composition from 'pure material 1' (Al_2O_3) to 'pure material 2' (ZrO_2) as seen in Figure 4.5. The interior circles represent a binary mixture of the two pure components with ratios as follows: 75/25, 50/50, 25/75 of Al_2O_3/ZrO_2, respectively as seen in Figure 4.11. Hence, if suitable pure inks are created, the entire composition range in the space may be rapidly processed in a single array printing experiment. The samples are discrete, and the composition step size can be

adjusted to suit the experimenter's desires. The pre-mixing of samples can be avoided and on the print properties can be tailored with real time mixing operations.

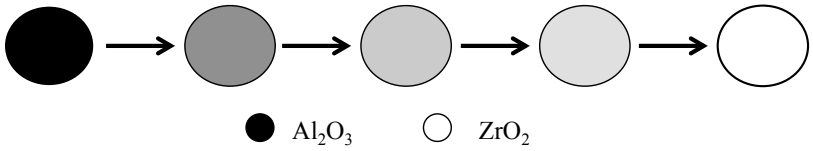

Figure 4.11: The black shade represents the Al_2O_3 while the lighter "white" shade represents the ZrO_2 material. The 5 circular shapes represent a different ratio of Al_2O_3 to ZrO_2 material ranging from 100% Al_2O_3, followed by 75/25, 50/50, 25/75, and ultimately 100% ZrO_2.

Aqueous stock inks of alumina (Al_2O_3) and zirconia (ZrO_2) were prepared at ϕ_{solids}=~0.45 volume solids loading such as those utilized and thoroughly explained in Specific Aim #1 (Chapter 3). The colloidal gels were loaded into individual syringes and attached to the robocaster (3D Inks LLC, Tulsa, OK) device as shown in the inset in Figure 4.4.

The mixing chamber was a custom assembly, which was designed and built to facilitate dynamic mixing of the two more colloidal gels immediately before extrusion. Figure 4.12 shows the entire motor and mixing chamber schematic in addition to a cross section of the mixing assembly. The mixed volume between the mixer body & mixing tip is stirred by a rotating mixing paddle. The active mixing region (or dead/mixing volume) is < ~300 nL.

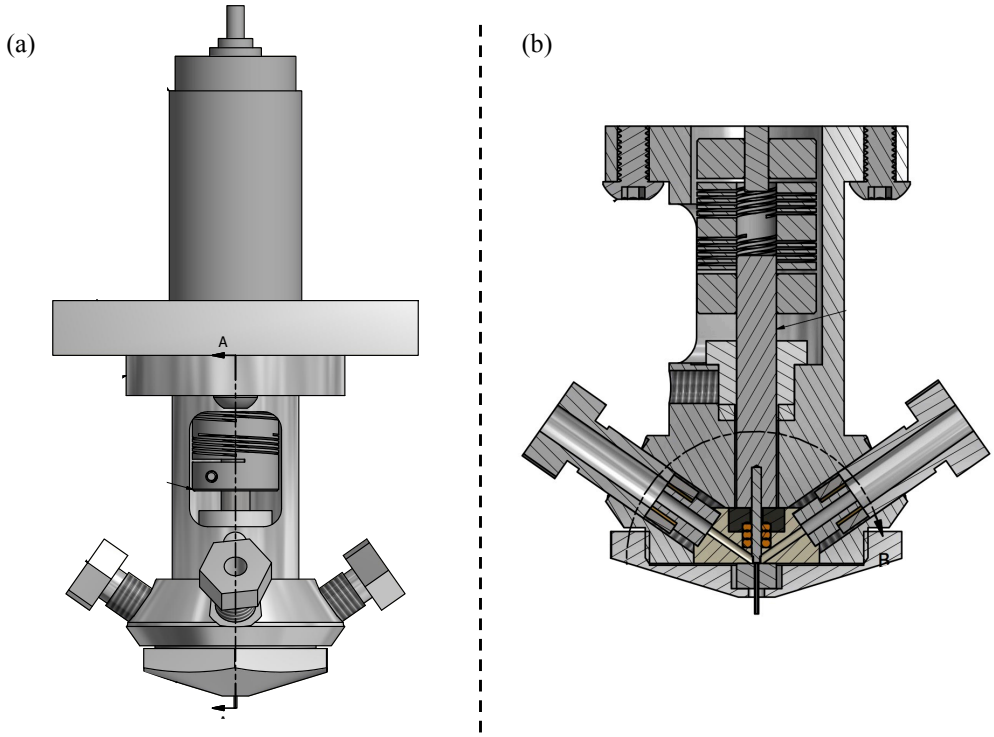

Figure 4.12: (a) Overall schematic of the mixing motor assembly, (b) cross-section of the entire assembly from part (a) scaled at 2.5:1.

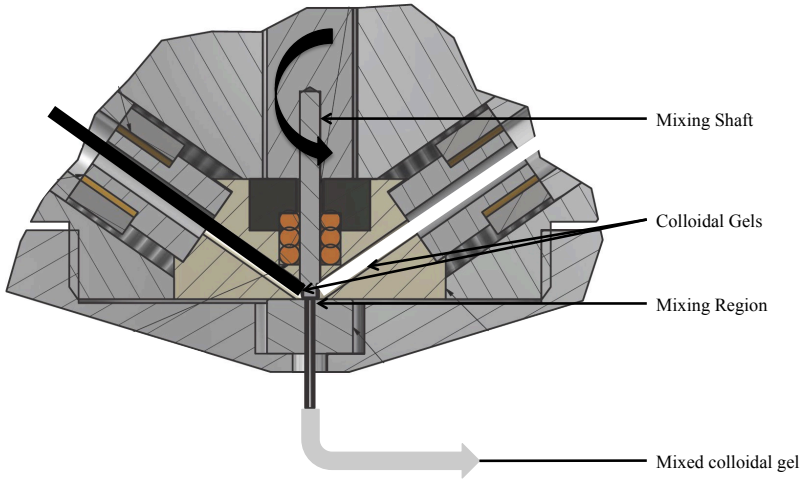

Figure 4.13: A magnified view of the mixing chamber assembly. Individual colloidal gels enter a common mixing chamber where they are mechanically mixed using a rotating paddle to produce a new mixed composite colloidal gel.

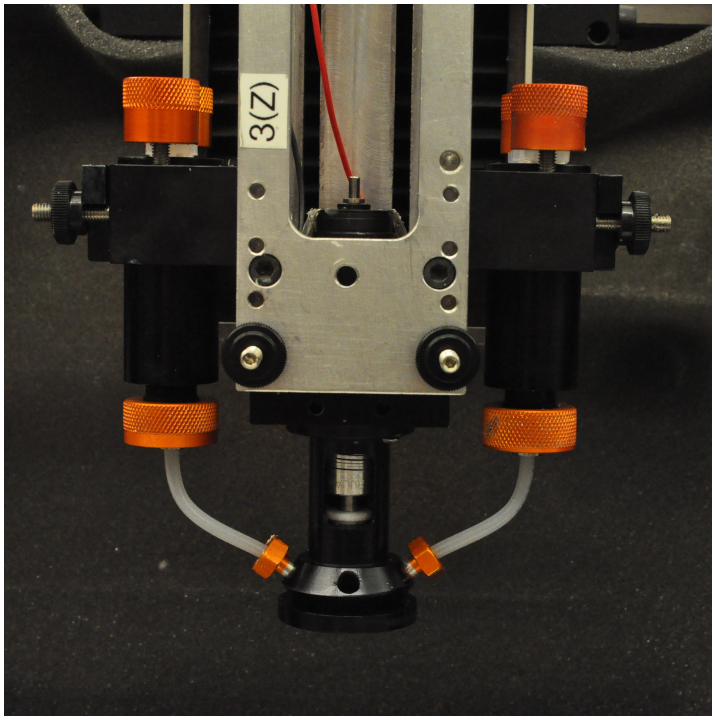

Figure 4.14: Digital image of mixing nozzle fully assembled, prior to printing silicone structures for analysis.

Positive displacement syringe pumps were used to push ink streams into the mixing chamber (Figure 4.12(c) and Figure 4.13) before being co-extruded as a single filament onto the substrate or underlying layers. Agitator mixing speed was maintained at 2000RPM. Four layer, space filled cuboid samples having square cross sectional area of 5 mm × 5 mm were written at a linear speed of 8 mm/s through a conical nozzle having a diameter of 337 μm (Eagle Stainless Tube and Fabrication, Inc., Franklin, MA). The simply calculated Reynolds Number (assuming no agitator factor) for this system was ~ 1.14×10^{-5} (distance, D= 0.2 mm, velocity, V=8 mm/s, density, $\rho_{Al_2O_3}$=3.3 g/cm^3 and ρ_{ZrO_2}=6.01 g/cm^3 and viscosity, μ = 800 Pa•s at a shear rate γ= 10 s^{-1}) with an average residence time of 37.5 μs within the mixing chamber.

$$\text{Reynolds Number} = \text{Re} = \frac{\rho VD}{\mu} = \frac{VD}{\nu} \tag{4.3.1}$$

V = mean colloidal gel velocity
D = pipe diameter
ρ = colloidal gel density
μ = colloidal gel dynamic viscosity
ν = colloidal gel kinematic viscosity

The low Reynolds Number together with a short residence time (τ) warrants the use of a mechanical mixing agitator/paddle to assist in mixing of the colloidal gels. Samples were then deposited onto an alumina substrate, which was immersed in oil. After the fabrication process, substrates were removed from the oil tray, dried in air at room temperature, sintered to 1650°C

for 4 hours, embedded, thin gold coated, and then subjected to back scatter electron microscopy (B-SEM).

$$\text{Residence time} = \tau = \frac{V}{q} \tag{4.3.2}$$

V = system capacity to hold a substance

q = flow rate of the substance through the system

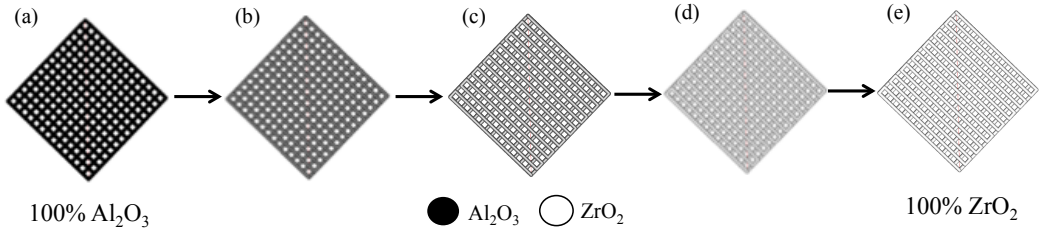

Figure 4.15: This figure represents what the the shapes which will look like from a top view, these are CAD images rendered in RoboCAD 4.1: (a) 100% Al_2O_3, (b) 75/25 Al_2O_3/ZrO_2, (c) 50/50 Al_2O_3/ZrO_2, (d) 25/75 Al_2O_3/ZrO_2, and (e) 100% ZrO_2.

4.3.6 Heat Treatment of Scaffolds

Samples printed with a ratio of Al_2O_3 to ZrO_2 ink were sintered in an air atmosphere furnace (Nabertherm LHT 02/17, Nabertherm GmbH, Lilienthal, Germany) for 2 hours at 1600°C, which was attained from room temperature. The temperature increase rate was kept at 5°C/min, while two constant temperature steps at 80°C for 2 hour and 500°C for 4 hours were introduced before dwelling for 4 hours at 1650°C.

4.3.7 Scaffold Characterization - X-ray Diffraction

The XRD (Bruker AXS D8 Discover, Madison, WI) was used to determine the crystalline phase(s) present within the raw, green and sintered stages. Three different spectra from each testing group were obtained (n=3 per group). The diffractometer, using a curved crystal monochromator, operating at 45mA and 45kV, and scanned in the 2θ with a range from 20-65° [10], with a step size of 0.02° at 3 seconds per step.

Rietveld refinement analysis used the data collected from X-Ray diffractometer, which subsequently converted data to "*.xy*" format. The raw data was then input into, Material Analysis Using Diffraction (MAUD) software for quantitative analysis. Rietveld analysis utilized the samples from previous XRD spectra (i.e., peak, heights, widths and positions). This refinement method was used to verify the phase(s) (Al_2O_3 or ZrO_2) present in the individual colloidal gels at the different stages.

4.3.8 Back-scattered Electron Microscopy (B-SEM)

Scaffolds of the different rationed groups were infiltrated and finally embedded using a methacrylate-based resin (Electron Microscopy Sciences, Fort Washington, PA) according to the manufacturer's instructions. A field emission scanning electron microscope (FE-SEM) (Hitachi S-4800, Santa Clara, CA) was used to observe the 'mixedness' of the colloidal inks thru the mixing motor. The polymerized sample blocks were then subjected to cut and grinding. The blocks were then cut in half by aiming the center of the scaffold along the axis with a precision diamond saw (Labcut 1010, Extec®, Enfield, CT). The sections were then polished by means of a series of SiC abrasive papers (400, 600, 800, and 1200 grit) (Carbimet, Buehler, Lake Bluff, IL) using a grinding/polishing machine (Labpol 12-3DI, Extec®, Enfield, CT) under water irrigation [117]. A 1-μm polishing compound was used to remove residual scratches. Scaffolds of the different rationed groups were mounted onto standard SEM pin stub mounts, (Product #: 16111, Ø12.7mm x 8mm pin height) (Ted Pella, Inc. Redding, CA), grounded with Graphite Conductive Adhesive 154 (Electron Microscopy Sciences, Fort Washington, PA), and mounted to a multi holder for 8 pin stubs (Product #: 15310-8) (Ted Pella, Inc. Redding, CA). The multi holder was placed into the sputter coater (Edwards S150B Sputter Coater, Sanborn, NY) and coated with gold for one minute. The back-scattered electron detector (BSE), work was performed at the Core Lab of Helmerich Research Center at OSU-Tulsa and was used to give a better representation of the mixing methods. BSE microscopy is based on the larger atoms, those greater atomic number, Z, having a higher probability of producing an elastic collision because of their larger cross-sectional area. Subsequently, the number of backscattered electrons reaching a BSE detector is proportional to the mean atomic number of the sample. Therefore, a "brighter" BSE intensity is correlated with higher average Z in the samples, while the "dark" areas have a lower average atomic number, Z. Thus, BSE images were helpful for obtaining high-resolution compositional maps of the mixing and to distinguish between the two phases [118-121].

4.3.9 Radial Distribution Function (RDF)

In order to compare and describe the mixing modes (powder mix *vs* colloidal gel mix), a pair distribution function g(r), needed to be calculated. The particle positions were located using a macro (Appendix C) along with the particle analysis function of ImageJ (National Institutes of Health). The g(r) is represented mathematically with the following formula,

$$g(r)=\frac{N(r)}{4\pi r^2(\Delta r)\rho} \tag{4.3.3}$$

where N(r) was the number of particles in an annular disc/shell of width, Δr, at a distance of a radius, r, drawn with a particle at center, ρ the number of particles per cm^2 [122]. This correlation function, *g(r)*, with respect to a two-dimensional image as shown in Figure 4.16(a) and (b), calculated based on pairs of particles relative to the reference particle. This function ultimately is more so a qualitative expression, with regards of giving the probability of locating the center of one particle a specified distance from the center of another particle. At short distances (r), the correlation will most likely be equal to zero while at greater radius values the *g*(r), converges to 1, which will give the indication of a uniform probability. There were 3 experimental groups and each group had three RDF correlations compared to each other (Table 4.2).

↓ Experimental group	Analysis Group/Area ↓		
75/25% Al_2O_3/ZrO_2			
50/50% Al_2O_3/ZrO_2	Surface Area	Powder Mixed	Colloidal Gel Mixed
25/75% Al_2O_3/ZrO_2			

Table 4.2: Experimental groups used for determination of the radial distribution correlation among the experimental groups.

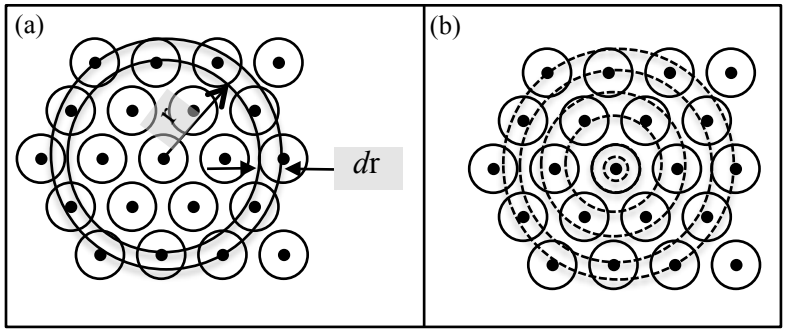

Figure 4.16: (a) and (b) both represent the Radial Distribution Function as a probability of finding two particles at some distance or separation of radius, r [122].

4.4 Results and Discussion

4.4.1 Rheological comparison Al_2O_3 and ZrO_2 vs. BCP

As illustrated in Figure 4.17 and summarized in Table 4.3, when the shear stress (τ) logarithmically increases from low to high values, the elastic modulus G' keeps constant as equilibrium elastic modulus G'_{eq} until yield value, τ_y, after that, the elastic modulus G' decreases significantly. The scaling of equilibrium elastic modulus G'_{eq} and yield stress τ_y with solid fraction, ϕ_{solids}, for the different materials are shown in Figure 4.17. The results for of the Al_2O_3,

BCP, and ZrO_2 of similar ϕ_{solids} loading varied by an order of magnitude in comparison to the BCP colloidal gel. The trend as seen, increasing values in the Al_2O_3 and ZrO_2, was expected, as for a fixed ϕ_{solids}, the G'_{eq}, and critical stress τ_y increases with higher amounts of [PEI] wt%, resulting in a stiffer colloidal gels [53].

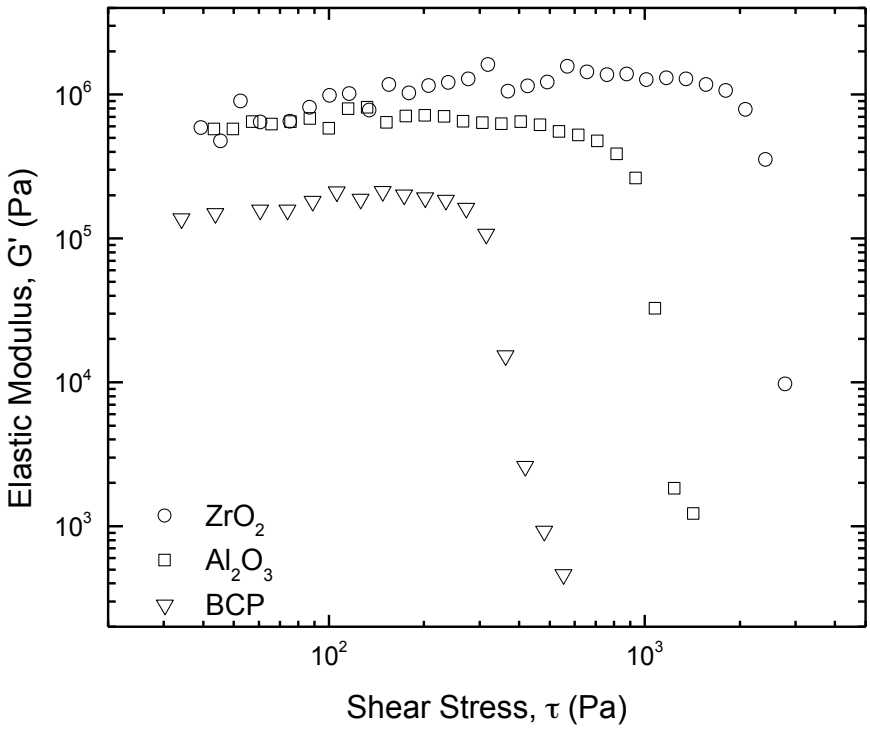

Figure 4.17: Experimental rheological data, shear elastic modulus, G', as a function of shear stress τ, for Al_2O_3 and ZrO_2 compared to BCP colloidal gels of φ_{solids} = ~0.47.

Sample	Al_2O_3	ZrO_2	BCP
G'_{eq} (Pa)	1,104,900	1,971,000	212,000
(0.9) G'_{eq} (Pa)	994,410	1,773,900	190,800
τ_x	1082.23	2868.83	235.99
δ (°)	45.0	45.0	45.0
[F4M] (mg/mL)	7.0	8.5	8.0
[PEI] (%)	6.0	6.0	5.0
Φ_{solids}	0.47	0.465	0.46

Table 4.3: A summary of the pertinent information/results extrapolated from Figure 4.17 for the comparison of the 3 different collodial gels used for robocasting.

The two tip fabrication method prints were done with either a white and black silicone combination (All Purpose Silicone GE112A 24C, GE Silicone, Huntersville, NC) or the combination of Al_2O_3 and ZrO_2. Figure 4.7 represents how the material is changed during a layer-by-layer design. The advantage with a two-tip printing method is there is no need in taking

a change over of material into consideration, as is the case with the mixing chamber method. The disadvantage is that with the two-tip printing apparatus you can print only 100% material 'A' or 100% material 'B' at a time, while the challenge with the mixing chamber was to consider the residence time when adjusting the ratios of multiple materials during the printing process. In the present study this was accomplished by a design feature of the mixing chamber, keeping the dead volume relatively low (<~300 nl).

4.4.2 Material Characterization and Mixing method analysis

The scaffolds were prepared two different ways: (1) 'pre-blended' to a certain ratio of Alumina to Zirconia (powder mixed) or (2) mixed from the colloidal gel via the novel-mixing nozzle. In some instances silicone was used to give a better visualization of the results, whether it was printing with 'pre-blended' materials using the nozzle array or using 'pure' one phase colloidal gel blended with another 'pure' form to result in a predefined ratio. Figure 4.7 shows what the capability of the nozzle array can print, from the macroscopic scale, giving the ability to vary materials in a layer-by-layer fashion. While Figure 4.18, was printing using the mixing nozzle, and only using two materials, but were able to further customize on the go, by adjusting the ratio or material #1 to material #2 between layers. This mixing nozzle method is beneficial by not limiting the user and structure to the 'pre-blended' materials that are loaded to print but allows for the customizability in various ratios.

Both materials and their respective final products were also subjected to a density analysis, with the alumina, being about 99.2% dense with respect to its theoretical density of 3.97 g/cm^3, while the zirconia was about 97.5% of its theoretical density of 6.05 g/cm^3. The mixed materials were approximately 98.2%(±0.004) when compared to their average calculated theoretical density based on the densities of alumina and zirconia and their relative phase fractions (based on volume percent) (Figure 4.23 and Table 4.6).

X-ray diffraction (XRD) spectra were collected of the individual materials (raw, green state, and sintered) (Figure 4.20). Their spectra were matched to the theoretical Al_2O_3 and ZrO_2. After confirmation of the material was complete the inks were fabricated and sintered to their respective protocols and XRD spectra (Figure 4.21) were then obtained for the experimental groups (Table 4.4) for crystalline phase determination. The alumina peaks exhibited peaks of higher intensity in groups 1 and 2, but started to decrease as the amount of alumina started decreasing and zirconia began to increase, this is seen in Figure 4.21.

The Rietveld analysis for crystalline phase quantification of the experimental groups (2, 3, and 4) is represented in Figure 4.22 and the phase fraction mean and the 95% confidence interval are listed in Table 4.5.

Group	Components
1	100% Al_2O_3
2	75/25% Al_2O_3/ZrO_2
3	50/50% Al_2O_3/ZrO_2
4	25/75% Al_2O_3/ZrO_2
5	100% ZrO_2

Table 4.4: Table summarizing the 5 experimental groups analyzed and compared with different fabrication protocols.

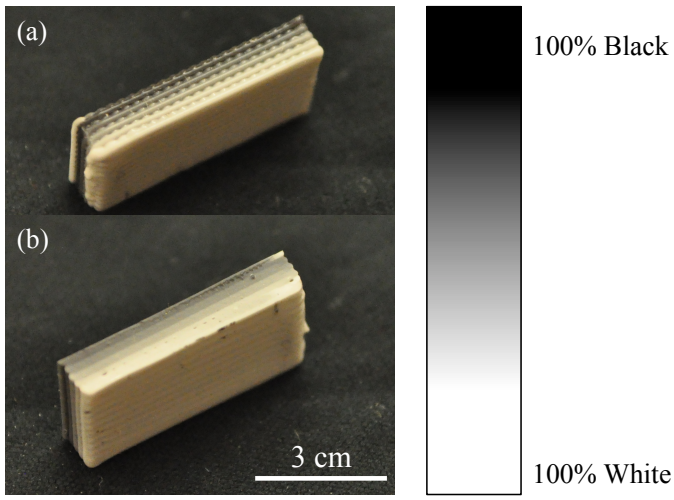

Figure 4.18: A digital image of a silicone square printed using the mixing nozzle, with the bar indicating the ratio of black and white silicone used in the program. (a) shows the outside edge, showing the detail as can be visually indicated by seeing the hairpin turns in alternating layer and (b) the square was cut longitudinally and shown here is the cross-sectional area. Each ratio printing 2 layers, starting at 100% white, 75/25% white/black, 50/50% white/black, 25/75% white/black, and ultimately ending with 100% black.

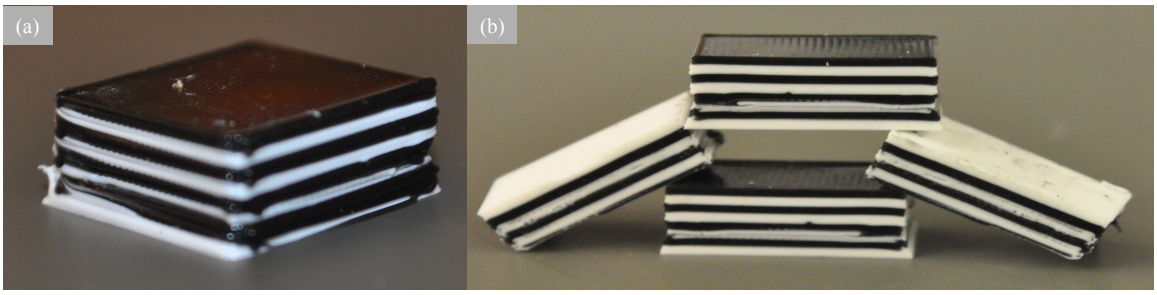

Figure 4.19: Digital images of silicone box scaffolds printed using the nozzle array. (a) the overall structure showing the interchanged layers and (b) cross-sectioned scaffolds to give a image of the continuity of the structure.

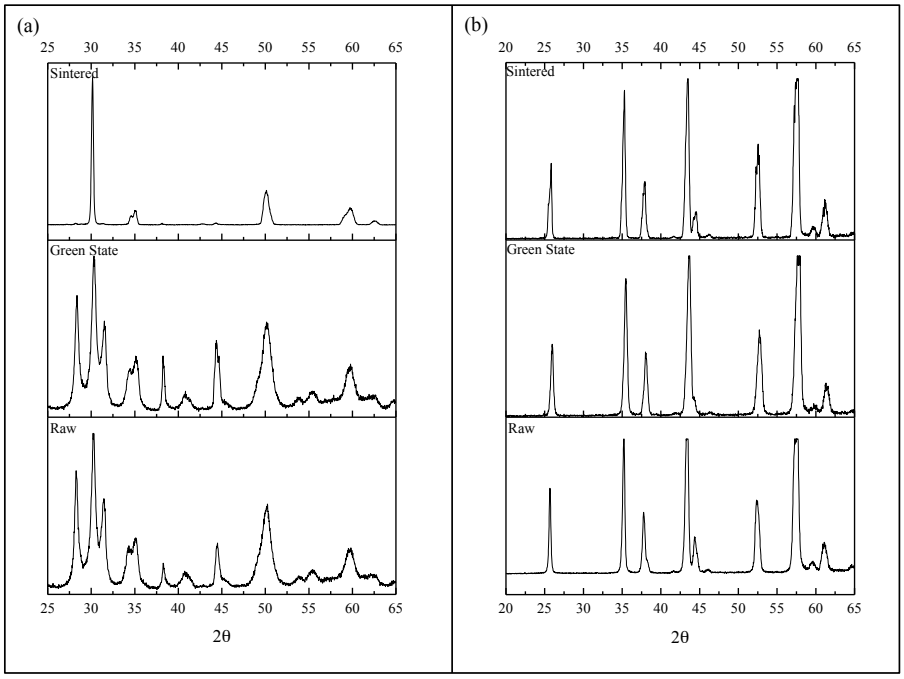

Figure 4.20: X-ray diffraction spectra of the (a) alumina and (b) zirconia materials used for the mixing study to compare the two different methods. Both materials had spectra collected for their raw state, green state, and following the sintering process for verification purposes.

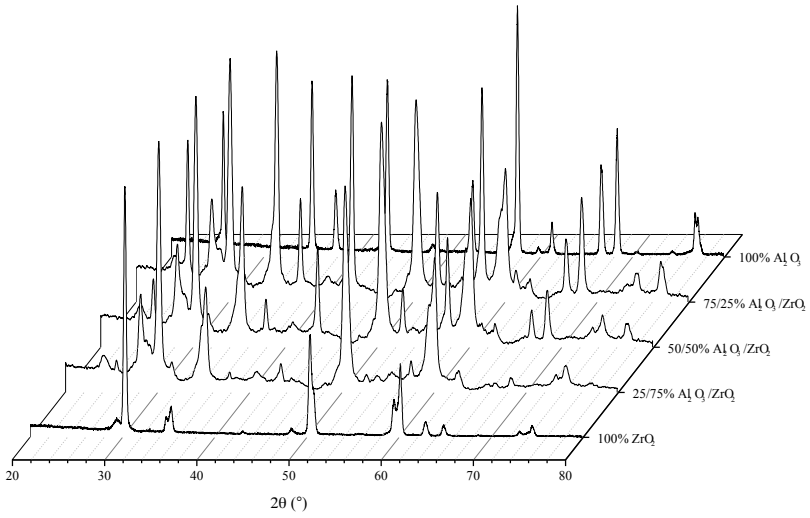

Figure 4.21: XRD spectra of the 5 experimental groups, with three regions of interest indicated to visually show that the materials were being mixed and the spectra was able to determine the values of these.

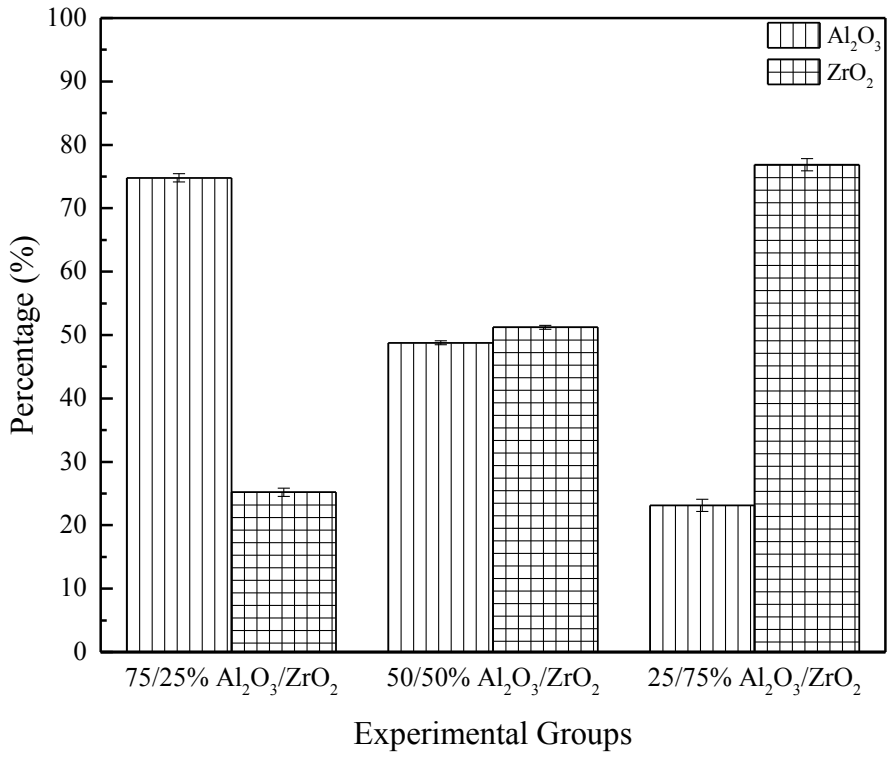

Figure 4.22: Percentage of each phase, Al_2O_3 and ZrO_2, for the three experimental groups, along with their corresponding standard deviations.

Experimental Group ↓/Phase →	Al_2O_3	ZrO_2
75/25% Al_2O_3/ZrO_2	74.79% (±0.65)	25.21% (±0.64)
50/50% Al_2O_3/ZrO_2	48.78% (±0.33)	51.22%(±0.32)
25/75% Al_2O_3/ZrO_2	23.13% (±0.96)	76.87% (±0.96)

Table 4.5: Table indicating the percentage of each phase present in the experimental groups. The standard deviations (±S.D.) are listed in parentheses.

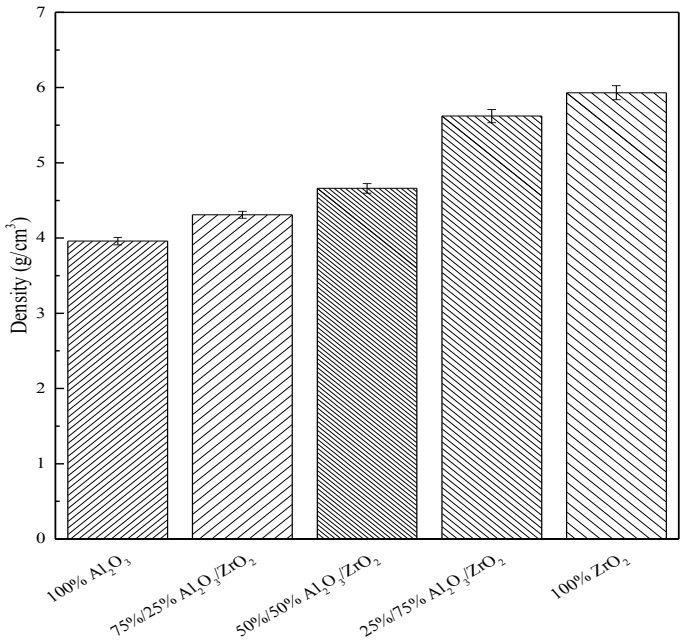

Figure 4.23: The above bar graph plots the mean densities and their respective standard deviations from the helium pycnometry analysis of the binary Al_2O_3 and ZrO_2 scaffold system.

Al_2O_3/ZrO_2				
100/0	75/25	50/50	25/75	0/100
3.94 (±0.04)	4.29 (±0.05)	4.63 (±0.06)	5.60 (±0.08)	5.90 (±0.09)

Table 4.6: Table summarizing density analysis, giving the mean values in g/cm^3, and their respective standard deviation (±S.D.)

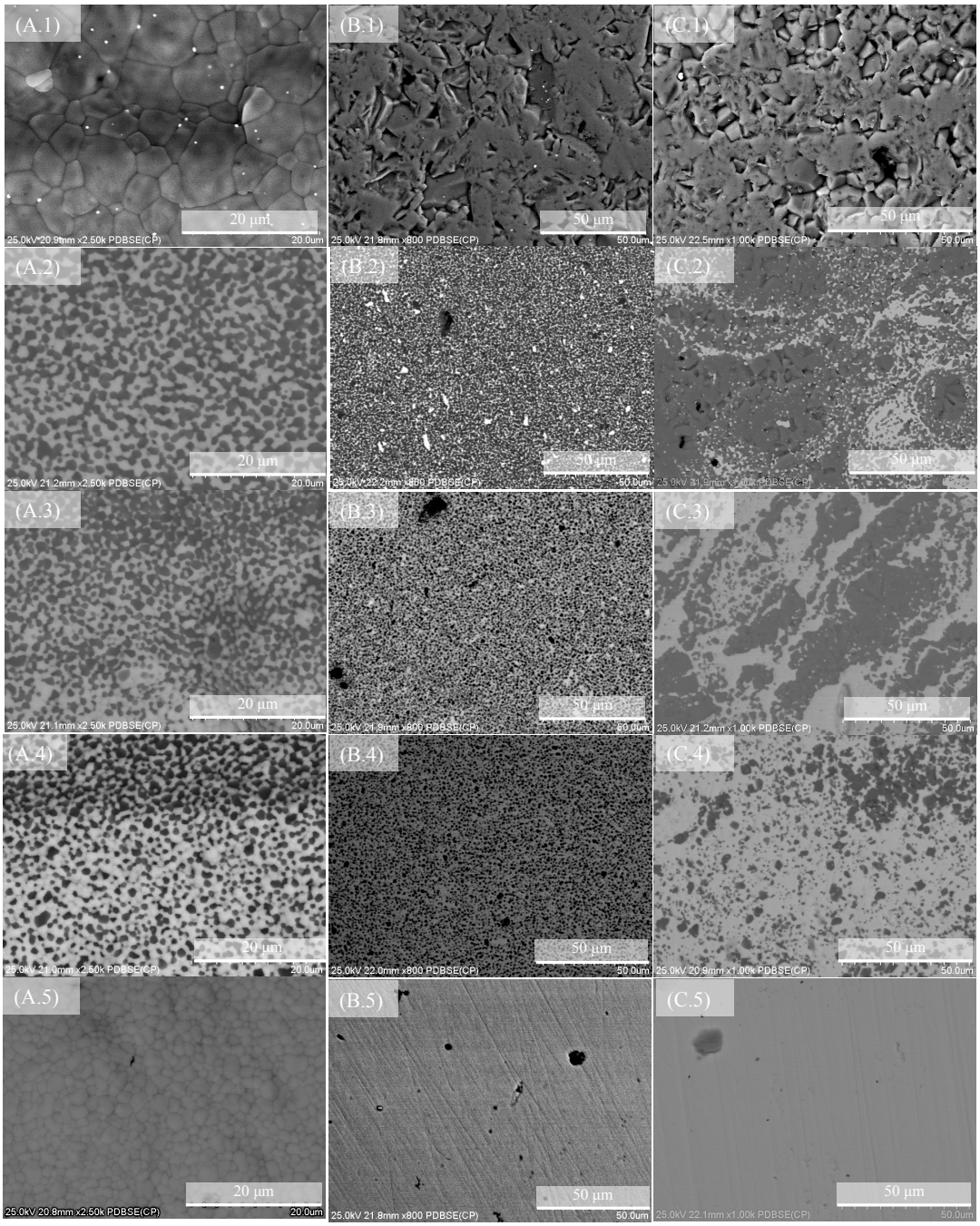

Figure 4.24: The above micrographs are back scatter SEM images for the three methods and 5 various experimental groups per method: (a) surface, (b) powder mixing, and (c) colloidal gel mixing, while ranging from (1) 100% Al_2O_3, (2) 75/25% Al_2O_3/ZrO_2, (3) 50/50% Al_2O_3/ZrO_2, (4) 25/75% Al_2O_3/ZrO_2, and (5) 100% ZrO_2.

Using the SEM micrographs and ImageJ software, an analysis was performed to give a rough quantitative answer to the proportion oh each material (e.g.: Al_2O_3 or ZrO_2). Figure 4.25

and Table 4.7 both give a summary of the phases among the 3 experimental groups where the Al_2O_3/ZrO_2, ratio was varied. Looking at the results in Figure 4.25, and using the dashed line (-----) as a point of reference for what the ratio was expected to be, it was concluded that the colloidal gel mixing gave results closets to the expected/designed values. The only group which did not have any statistical significance (p>0.05) was the 25/75% Al_2O_3/ZrO_2

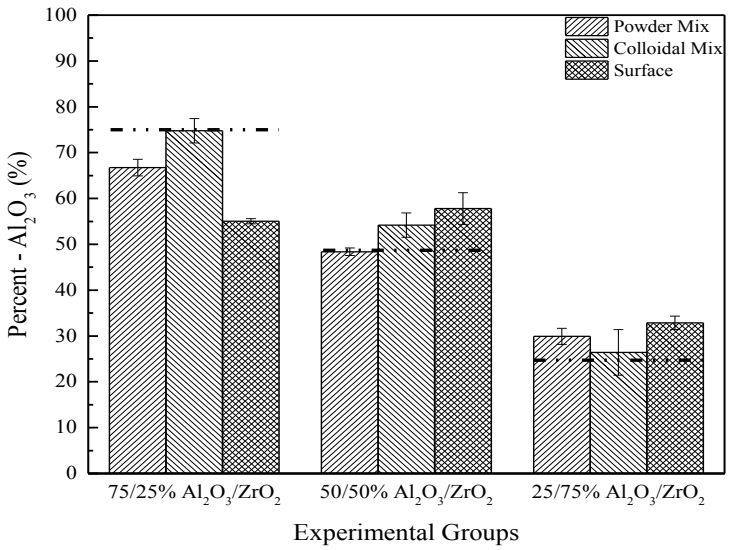

Figure 4.25: Bar graph representing the mean phase percentage of alumina (Al_2O_3) along with its corresponding standard deviation (±S.D.). The dashed lines represent the volume % of the as fabricated structure/ink.

Exp. Group ➔ Area ↓	75/25% Al_2O_3/ZrO_2	50/50 Al_2O_3/ZrO_2	25/75 Al_2O_3/ZrO_2
Surface	55.04(±0.6)/ 44.96(±0.3)	57.8(±3.5)/ 42.2(±4.95)	32.85(±1.5)/ 67.15(±2.1)
Powder Mix	66.74(±1.8)/ 33.26(±2.5)	48.38(±0.8)/ 51.62(±1.1)	29.91(±1.8)/ 70.09(±2.5)
Colloidal Mix	74.80(±2.7)/ 25.2(±3.8)	54.17(±2.7)/ 45.83(±3.8)	26.43(±5.0)/ 73.57(±7.1)

Table 4.7: This table corresponds to Figure 4.25, giving the average numerical phase percentages for both alumina (Al_2O_3) and zirconia (ZrO_2) and with their respective standard deviations (±S.D.).

The radial distribution function (RDF) relates how the particles are packed together, relating the diameters of the particles, meaning that, the closest that two particles can be to one another will be equal to one diameter length. At short distances (r), the RDF will be equal to zero, indicating the effective width of the particle, this holds to be true due to the fact that the particles which are considered as 'hard spheres' will not overlap one another. The numerous peaks which can be seen in Figure 4.26, Figure 4.27, and Figure 4.28 indicate that the particles are packed around each other, with the occurrence of these peaks at larger radii being indicative of a higher degree of order. Also while the radius grows larger the *g*(r), converges to 1, which will give the indication of a uniform value. In all three experimental groups 75/25%, 50/50%, and 25/75% Al_2O_3/ZrO_2, the powder mixing group showed the smoothest RDF results, with a continuous value hovering around RDF=1 (Figure 4.26(b), Figure 4.27(b), and Figure 4.28(b)). The powder mixing group showed more organization and was visually seen that way too, when comparing the Al_2O_3 and ZrO_2 phases as can be seen in the backscatter SEM micrographs (Figure 4.24).

Taking for instance Figure 4.24(B.3) and Figure 4.24(C.3), powder mixed and colloidal mixed respectively, it is clearly seen that the mixing condition is different in comparison to one another. One can see the distinction between the two phases (Al_2O_3 and ZrO_2) but the continuity of the mixture is not a smooth, which when looking at the RDF results in Figure 4.26, Figure 4.27, and Figure 4.28, makes it evident that the powder mixing results in a better particle distribution. Although the mixing of particles was not as uniform in the colloidal gel mixing method in comparison to the powder mixing, the phase quantities were still near the designed values, indicating that the mixing nozzle and its corresponding parts did properly extrude the correct ratio of materials.

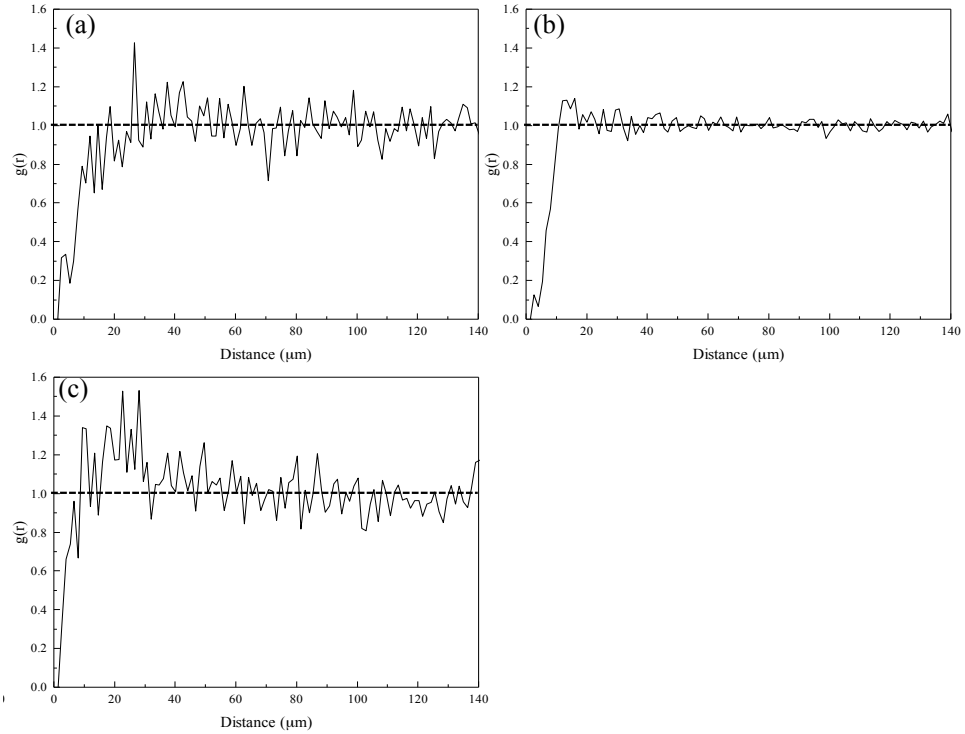

Figure 4.26: The radial distribution functions for 75/25% Al_2O_3/ZrO_2, for (a) Surface measurement, (b) powder mixing measurement, and (c) colloidal gel mixing.

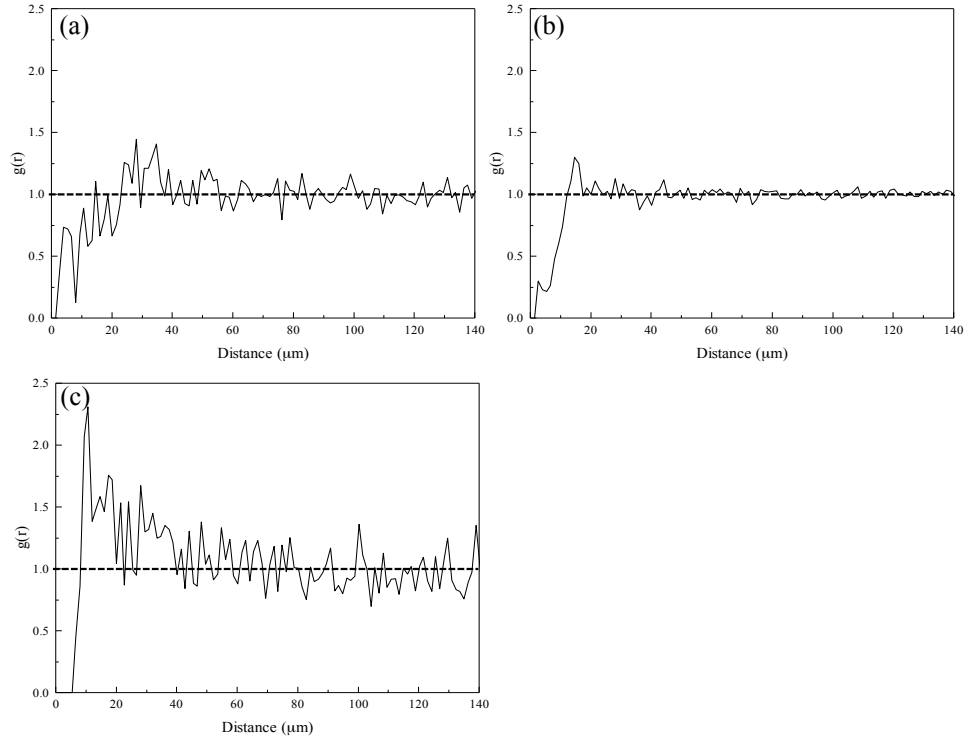

Figure 4.27: The radial distribution functions for 50/50% Al_2O_3/ZrO_2, for (a) Surface measurement, (b) powder mixing measurement, and (c) colloidal gel mixing.

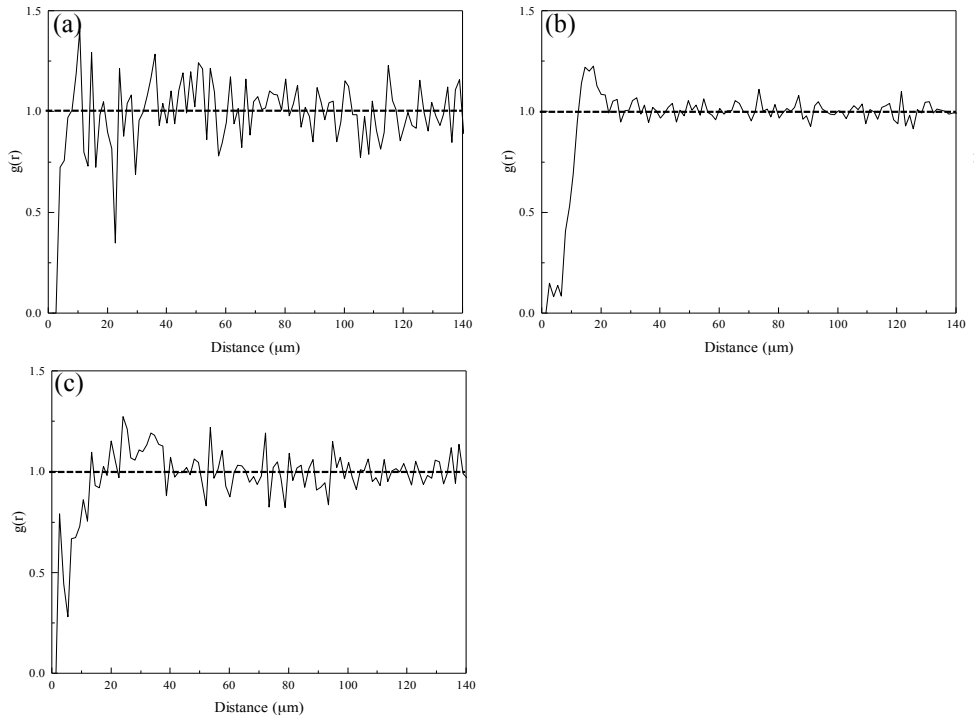

Figure 4.28: The radial distribution functions for 25/75% Al_2O_3/ZrO_2, for (a) Surface measurement, (b) powder mixing measurement, and (c) colloidal gel mixing.

4.5 Conclusion

The concept of functionally graded scaffold has led to the development of gradient porous biomaterials. While there are not many examples of actual applications of the graded porous biomaterials or scaffolds, the interest of searching a new fabrication method of the materials still continues. So far, few fabrication methods have been developed for producing functionally graded scaffolds. The biomaterials can be made into a gradient porous material. The structural features and mechanical properties of functionally graded/gradient porous scaffolds have not been characterized. There are very few *in vitro* and *in vivo* studies of functionally graded scaffolds. However, these functionally graded scaffolds are largely still in the stage of laboratory research. While there are several patents on graded porous biomaterials, examples of clinic applications are scarce. A possible hurdle may be the manufacturing cost, which will prevent the realization of the potential of functionally graded scaffolds. For (bio)inert porous biomaterials, graded/gradient pore size and porosity will have obvious long-term benefit in terms of tissue ingrowth and minimization of stress shielding. However, for these biodegradable porous scaffolds, the effect of graded/gradient micro-/macro- structures on the tissue ingrowth and

regeneration would be only in a short term. While functionally graded scaffolds and their composites have optimized mechanical and cell/tissue ingrowth properties, there will still be room for enhancement. Cost-effective methods are still needed to ensure suitable pore sizes and high pore interconnectivity. With the current trend being in bone regeneration rather than tissue replacement, bioactive/biodegradable ceramic composites in the form of graded porous scaffolds will have their advantages compared to homogeneous porous biomaterials and compared to sole polymer or ceramic porous materials. The pores in the functionally graded porous scaffolds can be tailored with the application of a coating (e.g., slurry dipping, sol-gel coating, or biomimetic coating (simulated body fluid (SBF)). Furthermore coating with proteins or embedding with growth factors can also modify the porous scaffolds. The macro-scaled pores can also be modified by filling or loading with biodegradable ceramic material such as calcium sulfate ($CaSO_4 \cdot 2H_2O$), biodegradable polymers, or natural species like collagens, chitosan, or cells. One promising case would be the development of porous bioactive/biodegradable composites with graded/gradient pore size, porosity, and composition and the modification of the composites with spatially distributed biochemical stimuli so that stem cells loaded into scaffolds would develop into complex tissues such as bone-cartilage tissue.

With regard of printing these graded or functionally graded materials, certain parameters must be established to successful fabricate these with reproducible results. Taking the scaffold graded on the macro scale, i.e. varying material between layers or struts, with the use of the nozzle array tool, the ability to control the on-off of the ink flow is critical. The nozzle array allows for the use of multi-tips, extruding 'pre-blended' single or multicomponent ink, with distinct placement. The volumetric flow rate, Q, is ~300 nl/sec and a start-stop volume of <6 nl is ideal. Although those two parameters are crucial to fabrication, the precise alignment of the multiple tips is also a key factor. While trying to fabricate scaffolds, which are functionally, graded the use of a mixing nozzle is necessary. The premise of the mixing nozzle is to allow the ability to change material on the go while printing, allowing for even greater customizability on various scales. Ideally the mixing nozzle would allow for quick change in composition, therefore a mixer volume, V_{mixer}, < 100nl is ideal. Having a small dead volume, means that there is not much material, if any built up, so it is mixing and then being immediately extruded, so ideally this would permit to have a quick change over from one ratio to another. Additionally, just as in the nozzle array, the on-off parameter is important, allowing for precise starts-stops. With no less importance than the other parameters with regards to the mixing nozzle, the mixing efficiency is highly important. This is important due to the fact that one would like to have an evenly distributed mixture.

From the backscatter SEM analysis, qualitative and quantitative, it was approximated that the correct ratios of the two materials, Al_2O_3 and ZrO_2, (i.e. 100/0, 75/25, 50/50, 25/75, 0/100) was retained in the fabricated scaffold samples. Although the ratios were within 5% of their designed ratio, the mixing of the colloidal gels in the mixing nozzle was not as ideal, when compared to the powder mixed, 'pre-blended' colloidal gels. The cross sectional images of colloidal mixing method revealed large spots, ~10 μm, of phases in randomly oriented spots in the mixed phase scaffolds. Even though from the surface micrographs the mixing looked to be uniform, the results from the RDF are not in entire agreement with the images. In the past a similar result has been seen with using a similar protocol in mixing, and two primary factors can possibly be linked to the poor distribution, (1) the dead volume and residence time may be too small, with a quick mix and extrude, the gel is lacking the sufficient mix by the paddle; (2) the viscosities of the colloidal gels may be too large to permit for them to fully and uniformly mix thoroughly in the short amount of time and small amount of volume. Three viable solutions may be to either (1) increase the size of the dead volume, (2) increase the mixing motor RPMs to great than 2,000, and/or (3) tweaking the viscosities of the colloidal gels.

The benefit of the mixing nozzle has over the nozzle array, is maneuvering away from the fabrication of scaffolds using 'pre-blended, multi-component' ink (100% β-TCP, 15/85% HA/β-TCP, or 50/50% Al_2O_3/ZrO_2) and allowing the use of infinite compositions with grading in 1D, 2D, and 3D. To further the possibilities with these tools/accessories, combining the mixing nozzle with the nozzle array will allow for the printing of intricately designed functionally graded scaffolds with support material. This is an important feature for various applications, especially in can be of use in the dental and orthopedic applications. This will allow the ability to indicate and place at specific locations a particular ratio of material, allowing either zirconia toughened alumina (ZTA) or alumina toughened zirconia (ATZ). This kind of customization will be ideal to the users as much as it will be to the recipients who will be getting the benefit of these biomaterial scaffolds. Just as this will give the further customizability in non-bioresorbable ceramic scaffolds, it will be beneficial to the community of bioresorbable ceramics such as hydroxyapatite and β-tri-calcium phosphate. With the utilization of this design of the mixing nozzle will allow the user to fabricate scaffolds which vary composition radially, in turn allowing even closer mimicking of the patients bone, when taking the long bone into account.

CHAPTER 5
INNOVATIVE THREE-DIMENSIONAL BCP SCAFFOLDS FOR CRITICAL LONG-BONE DEFECT REGENERATION

5.1 Overview

This chapter ties in the techniques and results from previous chapters and gives a more thorough *in vitro* analysis, and further provides some preliminary data towards the prototype critical sized long bone defect, using a long bone scaffold. The results from the previous chapters as well as this chapter lay important groundwork to move forward in using these ceramics and mode of fabrication to help repair long bone defects or fractures.

5.2 Introduction

The repair of critical sized long bone segmental defects has been an interest in the orthopedic field due to its reconstructive complexity. Attention is given to the defective site's blood supply, with focus between bone and immune cells and mechanical reestablishment. Commonly, these defects are caused by trauma, or tumor resection. These issues may leave the patient with a critical size defect, which must be controlled with suitable dead space management followed by bony reconstruction using a graft material that is osteoconductive and degradable, minimizing complications and shortening the length of time of patient immobility.

Bone wound healing is a complicated area of research and doctors, engineers, and scientist will continue searching for the most appropriate solutions. Large, critical sized, defects or load bearing areas, there is not a viable or ideal solution on the market. The future of bone grafting is heading towards the combination of materials, which will have tailor-able properties. After a series of *in vitro* and *in vivo* studies done by Ricci et al and others a reliable scaffold model with regards to material and pore size was verified. Due to the drawbacks of traditional scaffold fabrication methods and tools, complex and intricate shapes have been limited, which in turn hindered the ability to fabricate scaffolds for more complex bone replacement sites.

Three-dimensionally printed scaffolds fabricated from colloidal gel based inks have been successfully used to assemble space filling solid structures, (e.g., high aspect ratio walls and periodic lattices) however, cantilevered elements or unsupported structures in the past have been

difficult to fabricate due to a lack of an appropriate fugitive support material. Ideally the fugitive support material would print and dry with similar characteristics as the previously mentioned ceramic colloidal gels, with the feature that it was removable during a sintering process. Therefore the support material must possess shear thinning with yield stress rheology and a shear modulus comparable to that of the ceramic based colloidal gel. Additionally it should be aqueous for compatible printing with ceramic-based colloidal gels. All while being stable enough in an oil bath during the printing process and resisting shrinkage upon drying.

Ultimately Smay et al. developed an aqueous fugitive support material, carbon black (CB) colloidal gel. The CB colloidal gel maintained its shape upon extrusion through the deposition nozzle and the drying of printed structures. Upon heat treatment in air, negligible residual ash was observed in the printed sample structures as can be seen in Figure 5.4. These characteristics suggest that the CB ink satisfies the printability requirements of the deposition process. The compatibility with the calcium phosphate based inks suggested that the CB ink may be compatible with other ceramic compositions. Furthermore, controllability of combustion rate via heating rate and oxygen partial pressure make carbon black inks appealing as a support for various structures. The development of this support material is expected to benefit the practitioners of aqueous colloidal gel solid freeform fabrication (SFF) processes to fabricate more complex and intricate scaffold design.

The stability of calcium phosphate (CaP) ceramics is known to be composition and structure dependent [123], and depending on the material (HA, β-TCP, or BCP) when implanted will undergo dissolution at different rates (HA < β-TCP) [31, 124]. When these CaP materials are implanted *in vivo*, induce a precipitation of a phase which is comparable to the HA like mineral found in bone [125]. While in some instances it has been seen that a bone apatite-like material was formed in a nonosseous site [124, 125]. Since one of the important factors with regards to bioactivity (bone tissue formation rate and bone tissue bonding) is the dissolution produced from the CaP ceramics, which in turn may affect cellular activity, organic matrix deposition, or mineral deposition [126, 127].

5.2.1 In Vitro dissolution release of Ca^{2+}

Dissolution, *in vitro*, measurements are of value to determine or observe any possible phase changes that can possibly occur during the fabrication process or dissolution process. [128, 129]. In the past there has been work done to try to interpret as well as predict the long-term effects of the dissolution of CaP ceramics. This study set out to determine the relative dissolution behavior of the four experimental groups (Table 5.1), specifically the mean concentration

(μg/mL) of Ca^{2+} and PO_4 which were released from the experimental scaffold groups in a Tris(hydroxy)methylaminomethane-HCl buffer environment [125].

Group	Description	Abbreviation
1	100% HA	HA
2	100% β-TCP	β-TCP
3	15/85% HA/β-TCP	BCP
4	15/85% HA/β-TCP (design)	BCP (design)

Table 5.1: Summary of the four primary experimental scaffold groups used for the *in vitro* evaluation of Ca^{2+} and PO_4 release over a set amount of time.

5.2.2 Chemical - Biological Factors

Many scaffold designs at times can incorporate extra chemical or biological factors to enhance bone growth (Table 5.2) [130-133]. The choice of selecting which factors to integrate should be based on the ultimate goal of the scaffold is to enhance cell by (i) differentiation or (ii) proliferation, although these two are inversely proportional both are time dependent. Each independent specific factor affects differentiation or proliferation differently with respect to tissue development [134]. Cells can be used as a factor for various purposes: (i) deliver a factor for tissue healing [135] or (ii) directly stimulate the cell population within the scaffold [134]. In certain instances the scaffold itself can be utilized as a release device for certain factors, such as having a material integrated into its macro pores [136] or it can be even filled with a carrier, such as calcium sulfate, $CaSO_4$, (CS), that can release cytokine agent [137].

Growth factor	Abbreviation	Functions
Bone morphogenic protein	BMP	BMPs are osteoinductive. Induces bone formation by causing the migration of mesenchymal stem cells and their differentiation into osteoblast. BMPs do not initiate osteoclast activity.
Transforming growth factor-β	TGF-β	Causes proliferation and differentiation of bone by stimulating migration of osteoprogenitor cells, and regulating cell proliferation, cell differentiation and extra cellular matrix (ECM) synthesis. Inhibits proliferation and differentiation of osteoclast progenitor cells.
Fibroblast growth factor	FGF	Induces angiogenesis by increasing osteoblast proliferation, and also a potent stimulant for

		wound healing
Insulin-like growth factor	IGF	Stimulates osteoblast proliferation and bone matrix synthesis. IGFs also stimulate osteoclasts.
Vascular endothelial growth factor	VEGF	Induces angiogenesis during and permeabilization of capillaries bone formation. Regulates migration, proliferation and survival of endothelial cells by nutrient supply through the newly formed blood vessels.
Platelet-derived growth factor	PDGF	A key regulator of wound healing/tissue repair. Stimulates bone cell proliferation and angiogenesis.
Epidermal growth factor	EGF	Participates in wound healing process by regulating keratinocyte phenotype
Placental growth factor	PGF	PGF, a member of VEGF family, stimulates angiogenesis.

Table 5.2: Commonly used growth factors in tissue engineering for drug delivery applications [138-140].

5.2.3 Possibility of Cytotoxicity (Ca^{2+} and PO_4)

Phosphorus (P) is widely distributed in the body. More than 80% of total phosphate (PO_4) is present in the bone and teeth in the form of apatite. The remaining phosphate is mostly present in the skeletal muscle, with trace amounts in the extracellular fluids (<0.1%) [141-144]. Intracellular phosphate ions are essential for oxidative phosphorylation and approximately 20% of cellular phosphate is present in the mitochondria. Roughly 30% of total cellular phosphate is stored in the endoplasmic reticulum and is used in phosphorylation of various proteins. The remaining cellular phosphate is present in the nucleus, Golgi complex and lysosomes. Transporting phosphate in and out of the cell according to the need of the body is a complex process and the exact molecular mechanisms of such sensitive transport are not entirely clear. It is important to note that cells use PO_4 to transport cellular energy through the formation of ATP by oxidative phosphorylation.

With the aforementioned, phosphorus is an essential nutrient for the body and is routinely consumed through food. After consumption, phosphorus binds with oxygen and exists as PO_4 in the body. Both organic and inorganic forms of PO_4 are present in regularly consumed foods. The amount of total PO_4 ingestion can be significantly influenced by consumption of processed food and beverage, as there are phosphate metabolites additives in these items. Following a meal,

inorganic phosphate can be rapidly absorbed across the small intestine and enter the blood stream causing an elevation in blood phosphate levels. The net efficiency of intestinal phosphate absorption is double that of Ca^{2+} [145]. Taking into consideration just the amount of phosphate consumed and adding a calcium phosphate (CaP) based scaffold can lead to a potential toxic situation. Phosphate toxicity due to excessive retention of PO_4 in the body can cause a variety of cellular and tissue damage (Figure 5.1). An example is seen with the higher occurrence of vascular calcification, encountered in patients with chronic kidney disease, is related to the increased retention of phosphate in the body [146, 147]. The normal range of PO_4, should be on the order of 2.4 – 4.1 mg/dL, so this is of importance as when scaffold is placed in the system, the levels in the local region may be slightly higher than normal, but should not increase the over all levels to prevent any complications such as cell death, which in turn would lead to killing new bone cells.

Inorganic phases	**Wt %**
Calcium orthophosphates (biological apatite)	~60
Water (H_2O)	~9
Carbonates	~4
Citrates	~0.9
Sodium	~0.7
Magnesium	~0.5
Traces: Cl^-, F^-, K^+, Sr^+, Pb^{2+}, Zn^{2+}, Cu^{2+}, Fe^{2+}	balance
Bioorganic Phase	**Wt%**
Collagen type I	~20
Non-collagenous proteins: osteocalcin, osteonectin, osteopontin, thrombospondin, morphogenetic proteins, sialoprotein, serum proteins	~3
Other traces: polysaccharides, lipids, cytokines	balance
Primary bone cells: osteoblasts, osteocytes, osteoclasts	balance

Table 5.3: Biochemical composition of bone [147, 148]

Ca/P	Compound	Chemical formula	Solubility at 25°C, −log(K_s)	Solubility @ 25°C, g/L	pH stability range in aqueous solutions at 25°C
0.5	Monocalcium phosphate monohydrate (MCPM)	$Ca(H_2PO_4)_2 \cdot H_2O$	1.14	~18	0.0–2.0
0.5	Monocalcium phosphate anhydrous (MCPA or MCP)	$Ca(H_2PO_4)_2$	1.14	~17	[c]
1.0	Dicalcium phosphate dihydrate (DCPD), mineral brushite	$CaHPO_4 \cdot 2H_2O$	6.59	~0.088	2.0–6.0
1.0	Dicalcium phosphate anhydrous (DCPA or DCP), mineral monetite	$CaHPO_4$	6.90	~0.048	c
1.33	Octacalcium phosphate (OCP)	$Ca_8(HPO_4)_2(PO_4)_4 \cdot 5H_2O$	96.6	~0.0081	5.5–7.0
1.5	α-Tricalcium phosphate (α-TCP)	α-$Ca_3(PO_4)_2$	25.5	~0.0025	[a]
1.5	β-Tricalcium phosphate (β-TCP)	β-$Ca_3(PO_4)_2$	28.9	~0.0005	[a]
1.2–2.2	Amorphous calcium phosphate (ACP)	$Ca_xH_y(PO4)_z \cdot n$H2O, n = 3–4.5; 15–20% H_2O	[b]	[b]	~5–12[d]
1.5–1.67	Calcium-deficient hydroxyapatite (CDHA or Ca-def HA)[e]	$Ca_{10-x}(HPO_4)_x(PO_4)_{6-x}(OH)_{2-x}$ ($0 < x < 1$)	~85	~0.0094	6.5–9.5
1.67	Hydroxyapatite (HA, Hap or OHAp)	$Ca_{10}(PO_4)_6(OH)_2$	116.8	~0.0003	9.5–12

1.67	Fluorapatite (FA or FAp)	$Ca_{10}(PO_4)_6F_2$	120.0	~0.0002	7–12
1.67	Oxyapatite (OA, OAp, OXA)[f]	$Ca_{10}(PO_4)_6O$	~69	~0.087	[a]
2.0	Tetracalcium phosphate (TTCP or TetCP), mineral hilgenstockite	$Ca_4(PO_4)_2O$	38–44	~0.0007	[a]

Table 5.4: Existing calcium orthophosphates and their major properties. [a]These compounds cannot be precipitated from aqueous solutions. [b]Cannot be measured precisely. However, the following values were found: 25.7 ± 0.1 (pH = 7.40), 29.9 ± 0.1 (pH = 6.00), 32.7 ± 0.1 (pH = 5.28). The comparative extent of dissolution in acidic buffer is: ACP >>α-TCP >> β-TCP >CDHA>> HA > FA. [c]Stable at temperatures above 100°C. [d]Always metastable. [e]Occasionally, it is called "precipitated HA (PHA)". [f]Existence of OA remains questionable [148, 149].

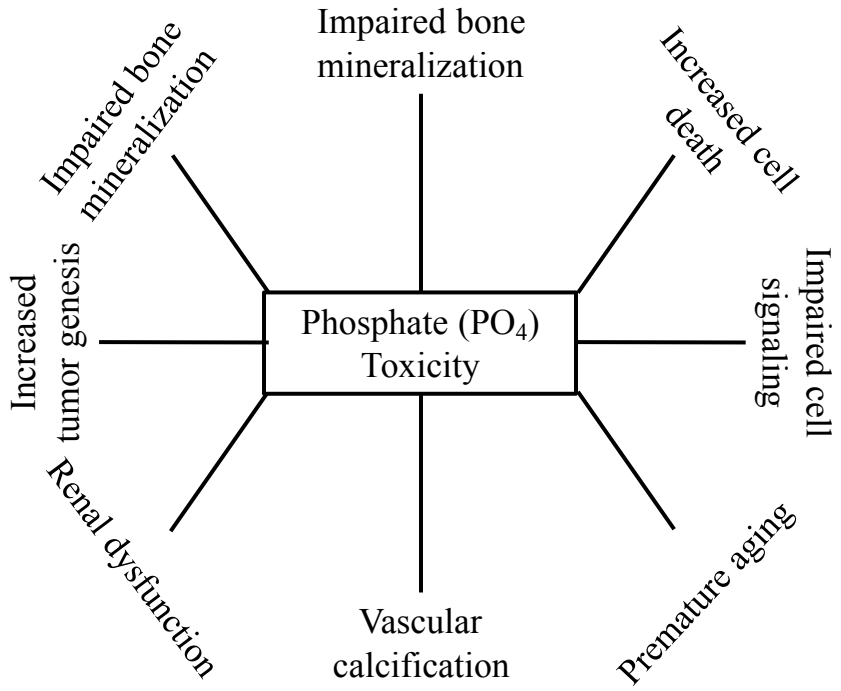

Figure 5.1: List of possibly pathological events, which can be related phosphate toxicity as previously documented in animal and human studies [145, 150, 151].

5.3 Experimental Section

5.3.1 Support Material – Carbon Black

The carbon black ink (CB) formulation utilized uses an anionic dispersant in combination with a cationic flocculent molecule to control gel strength. Carbon black (CB) (Monarch 120, Cabot Corporation, Billerica, MA) with specified particle density of approximately 1.8 g/cm^3 and specific surface area of ~31.3 m^2/g. To disperse the CB, sulfonated naphthalene condensate, ammonium salt (NSC4AL) (AGNIQUE NSC4AL, Cognis, Cincinnati, OH), a 44% by weight of an aqueous solution of ammonium neutralized derivative of sulfonic acid, containing a naphthalene functional unit, is used to stabilize carbon black in water. Subsequently, an aliquot of poly(ethylene glycol) (PEG) (Carbowax PEG-6000, Dow Chemical Company, Midland, MI) stock solution (10% by weight in water) was added at 5 mg/mL of ceramic and the suspension was again mixed for an additional 2 minutes at 2000 rpm. Nonlinear poly(ethylenimine) (PEI) (ICN Biomedical, Aurora, OH) with Mw = 50 to 100 kDa is prepared in aqueous stock solutions with 10% by weight polymer and is used as a flocculant. Deionized (DI) water (DI-H_2O) wherever mentioned has a nominal conductivity 5×10^{-4} $(\Omega\cdot cm)^{-1}$. In the robocasting process, paraffin oil (Ultra-Pure, Lamplight Farms, Menomonee Falls, WI) is used as an oil bath to prevent drying during the printing process.

An example of CB gel of 30mL volume with a solids volume fraction of $\phi_{CB} = 0.37$ is given in the following. The amounts of each concentrated stock solution; carbon black and water for this example are given in Table 5.5. First, the NSC4AL, along with carbon black powder is added to this aqueous solution in three equivalent aliquots and mixed for 1 minute after each addition using a non-contact, planetary mixer (Thinky AR-250; Thinky, Tokyo, Japan) and deionized water is added into a 250mL sample cup filled with 30g of 3 mm diameter zirconia milling media. Next, the PEG is added to the carbon black suspension. Finally the PEI flocculant is added to the carbon black suspension such that the weight ratio of PEI molecules to sulfonated naphthalene equals approximately 0.23. The PEI is added in four steps with mixing for 1 minute after each addition.

5.3.2 Thermogravimetric Analysis (TGA)

After drying, the carbon black gel is heated in a Simultaneous Thermal Analysis (STA) (STA 449 F1 Jupiter®, Burlington, MA) to characterize its burnout behavior. The heating profile from 25°C to 900°C occurs at a ramp rate of 2.5°C/min in zero hydrocarbon air composed of 80/20 N_2/O_2 ratio (ZHCAir, Airgas USA, Radnor, PA) with flow rate set to 150mL/min.

Carbon Black (CB)

$\phi_{CB}=0.37$ $\rho_{CB}=1.8\frac{g}{mL}$

$V_{total}=30mL$ [PEG]=10%

$V_{solid}=(45mL)\cdot\phi_{CB}=11.1mL$ (5.3.1)

$V_{liquid}=V_{total}-V_{solid}=18.9mL$ (5.3.2)

$M_{CB}=(V_{solid})\cdot(\rho_{CB})=19.98g$ (5.3.3)

$M_{NSC4AL}=(0.106)\cdot(M_{CB})=2.12g$ (5.3.4)

$$M_{PEI}=\left[[PEG]\cdot(10^{-3})\frac{g}{mg}\cdot(V_{liquid})\Big/\left(0.055\frac{g\cdot mol}{g\cdot stock\ solution}\right)\right]=1.50g \quad (5.3.5)$$

$$M_{PEG}=\left[M_{PEI}/M_{NSC4AL}\right]\cdot(M_{NSC4AL})=2.318g \quad (5.3.6)$$

$M_{H_2O}=(V_{liquid}-M_{NSC4AL}-M_{8PEG}-M_{PEI})\approx10.11g$ (5.3.7)

Table 5.5: The example calculation for the fugitive support material, carbon black (CB), based on a 37% solids loading ($\phi_{solids}=0.37$).

Substance	**Quantity (g)**
DI-water	~10.11
CB	19.98
NSC4AL	2.12
PEG	2.32
PEI (10%)	1.50

Table 5.6: Approximate values of necessary substances needed to make a 30mL batch of the fugitive support material, carbon black ($\phi_{solids}=0.37$).

5.3.3 Carbon Black vs. BCP gel

CB gel prepared is compared to the BCP colloidal gel that is prepared by polyelectrolyte induced bridging-flocculation [10, 59, 116]. The rheological properties are measured using a controlled stress-strain rheometer (C-VOR 200, Bohlin Instruments, East Brunswick, NJ) fitted with a C14 cup and bob geometry ($I.D._{cup}$ = 16mm, $O.D._{bob}$ = 14mm) with serrated walls to prevent wall slip. Pre-conditioning of the samples was performed. For each measurement, a sample of 3.6 mL of gel is loaded into the measuring system and subjected to 30 min oscillatory pre-shear at 1Hz with a controlled shear stress at 0.02Pa. After pre-shear, the sample is kept undisturbed 30 minutes for equilibrium. All measurements are conducted at 25°C with a cover and plate with filled water reservoir which is to minimize evaporation.

The shear elastic modulus (G') is measured in oscillatory mode, where the stress amplitude is logarithmically increased from 1 to 1000Pa at an angular frequency of $\omega = 1$Hz. The yield stress (τ_y) of the gel is taken as the stress magnitude where G' drops to 90% of the maximum value during a stress sweep experiment starting from low stress. The second set of experiments measures the flow curve of carbon black gel. In viscometery mode, the shear stress, τ, is recorded as a function of shear rate, ($\dot{\gamma}$) in an ascending series of discrete steps ($0.001 \sim 100 s^{-1}$) with a 1-minute equilibrium at each step. The apparent viscosity (η_{app}) of carbon black inks can be obtained as a function of the shear rate.

5.3.4 In Vitro Ca^{2+} and PO_4 release

The release of Ca and PO_4 ions during dissolution of the CaP based scaffolds (Table 5.1) was measured using 0.05 mol/L Tris-(hydroxy)methylaminomethane-HCl (bioWORLD, Dublin, OH) solution with a pH of ~7.3 and maintaining a temperature of 37°C (in an incubator). The weight of scaffold to volume of solution ratio was 1 mg/mL as recommended by Ducheyne et al. [125]. The time periods to be examined for the release of ions was 1 hour ranging to 2 weeks, with three samples measured for each time point. The Ca^{2+} concentrations of the solutions were measured with the utilization of atomic absorption spectroscopy (AAS) (Varian AA240FS, Santa Clara, CA). The phosphate (PO_4) concentration of the solutions was measured as a phosphomolybdate complex [125, 152] in a UV-visible spectrophotometer (Cary 5000 UV-Vis-NIR, Santa Clara, CA)

5.3.5 Cell Alignment/Cytotoxicity/Protein Mapping

Fluorescence microscopy images were taken of scaffolds stained 4',6-diamidino-2-phenylindole (DAPI), additionally staining for proteins S-100β and $p75^{LNGFR}$. The S-100β is indicative of a vital nervous system sell cell cytosolic protein [153, 154] while the $p75^{LNGFR}$ is a membrane receptor which is critical for binding certain growth ligands (e.g.: NT-3 and NGF) [154, 155]. The microscopy images were then analyzed using the angle tool in ImageJ [154, 156]. Approximately 400 cells were measured for the two time points. For each cellular nucleus, an angle was drawn between the major axis of the elliptical nucleus and the corresponding line drawn through the predominating strut direction. The corresponding angle off the strut was then recorded, the angle drawing procedure is illustrated in Figure 5.13(a).

5.4 Results and Discussion

5.4.1 Rheological properties of CB gel

The initial dispersion of CBG has a relatively low viscosity and gel behavior is only evident after the PEI flocculant, is added. Figure 5.2 shows the oscillatory and steady flow

behavior of CB gel. The elastic shear modulus (G') is graphed as a function of applied shear stress amplitude for the CB compared to the BCP colloidal gel. The magnitude of G' for the CBG material is comparable to that for the BCP gel. Three parameters may be used for comparison of the data: the plateau elastic shear modulus ($G_0^{'}$) is representative of the elastic nature of the colloidal gel network prior to rupture of the gel, the shear yield stress (τ_y) defined as the stress amplitude where $G^{'}/G_0^{'} = 0.9$ and the yield strain (γ_y) defined as the strain amplitude when $G^{'}/G_0^{'} = 0.9$ [157]. These results are summarized in Table 5.7. The latter is used as a more accurate representation of the physical process used in robocasting where the colloidal gel goes from rest in a reservoir and is then extruded through a tip. The yield stress of the CBG is the higher of the two materials. Likewise, the yield strain for the CBG gel is also higher, but BCP yield strain is lower. Perhaps the more important comparison for the CB gel to the BCP gel is the plateau shear modulus.

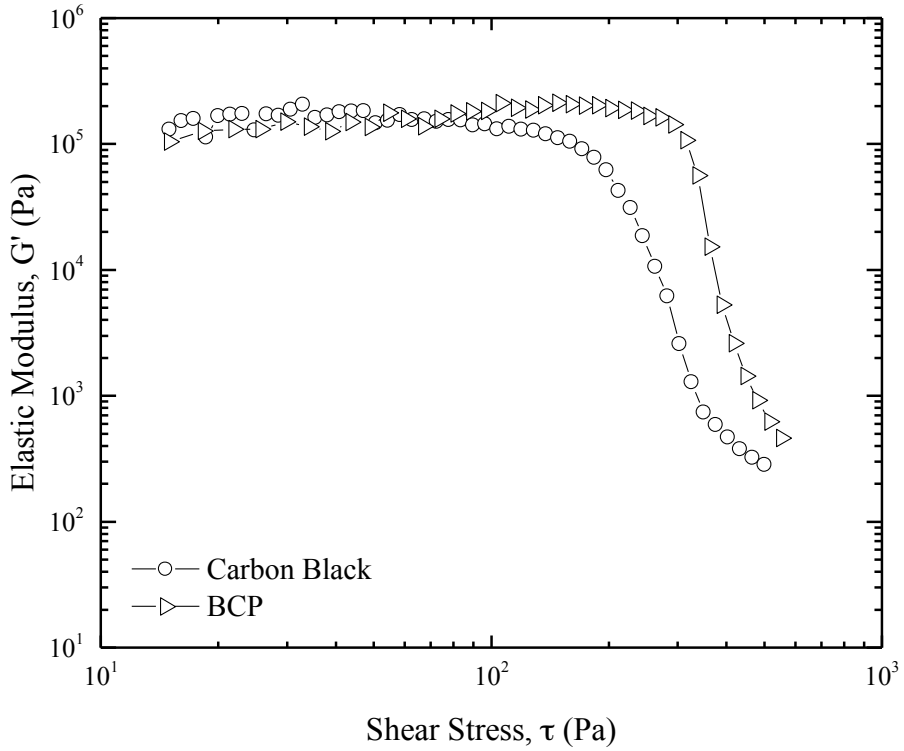

Figure 5.2: Rheology of BCP colloidal gel as compared to the fugitive support material, carbon black, illustrating the elastic modulus as a function of shear stress.

Sample	BCP	CB
G'_{eq} (Pa)	212,000	204,640
(0.9) G'_{eq} (Pa)	190,800	184,176
τ_y	32.38	46.06
τ_x	235.99	259.39
δ (°)	45.0	45.0
[PEG]	-	5%
$M_{[PEI]}/M_{[NSC]}$	-	0.23
Φ_{solids}	0.46	0.37

Table 5.7: Summary of rheology results in comparing two printable gels, BCP and the fugitive support material carbon black.

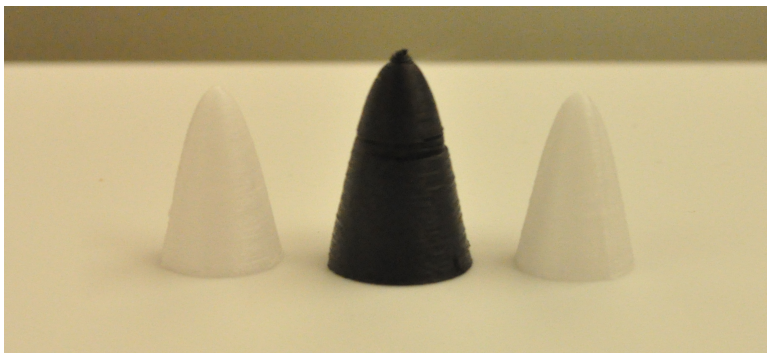

Figure 5.3: Digital image showing 3D printed cones from left to right: alumina, carbon black, and alumina.

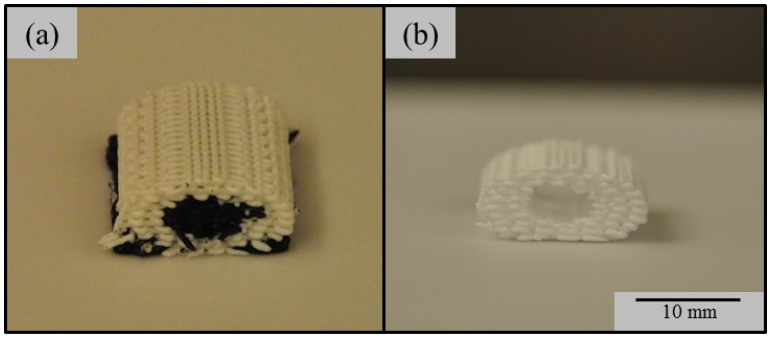

Figure 5.4: (a) A cubic window frame lattice structure printed with 100% β-TCP gel supported by the carbon black (CB) gel and (b) 100% β-TCP structure after sintering [59, 108].

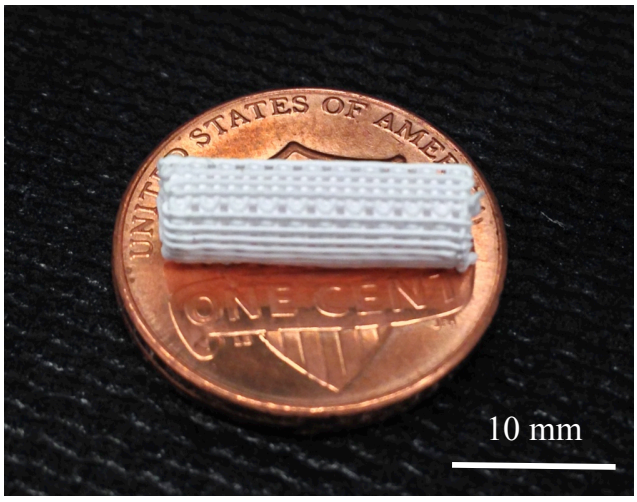

Figure 5.5: Digital picture of a 3D printed 100% β-TCP scaffold, using a penny as a reference for size comparison.

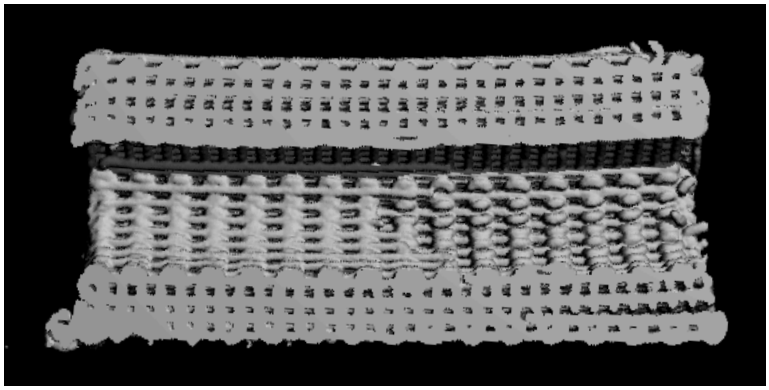
Figure 5.6: Three-dimensional reconstruction obtained through microCT of a 100% β-TCP long bone scaffold, the image is cut longitudinally.

5.4.2 TGA Analysis of Carbon Black Burnout

TGA results of as-dried CB ink are shown in Figure 5.7. The pre-drying of the ink evaporates any residual H_2O from the green structure and the remaining components in the initial state are the NSC4AL dispersant, the PEG gelling agent, PEI and carbon black particles. The TGA data indicated that burnout of the remaining material begins at around ~260°C in air. Loss of weight in the range from ~260°C to 345°C is presumed to be due to decomposition of polymeric additives. The calculated weight fraction of CB in this dried ink is w_{CB}=0.85. This discrepancy likely indicates that not all of the polymeric additives are easily volatilized at these lower temperatures, but rather indicate that some of the polymer burns off at higher temperature along with the degradation of the CB particles. Above 460°C, oxidation of carbon black accelerates and comes to completion by ~645°C. Hence, it is determined that at ~625°C burnout of carbon black support may be carried out to completion at a reasonable speed in air, which is consistent with observation from other researchers [158].

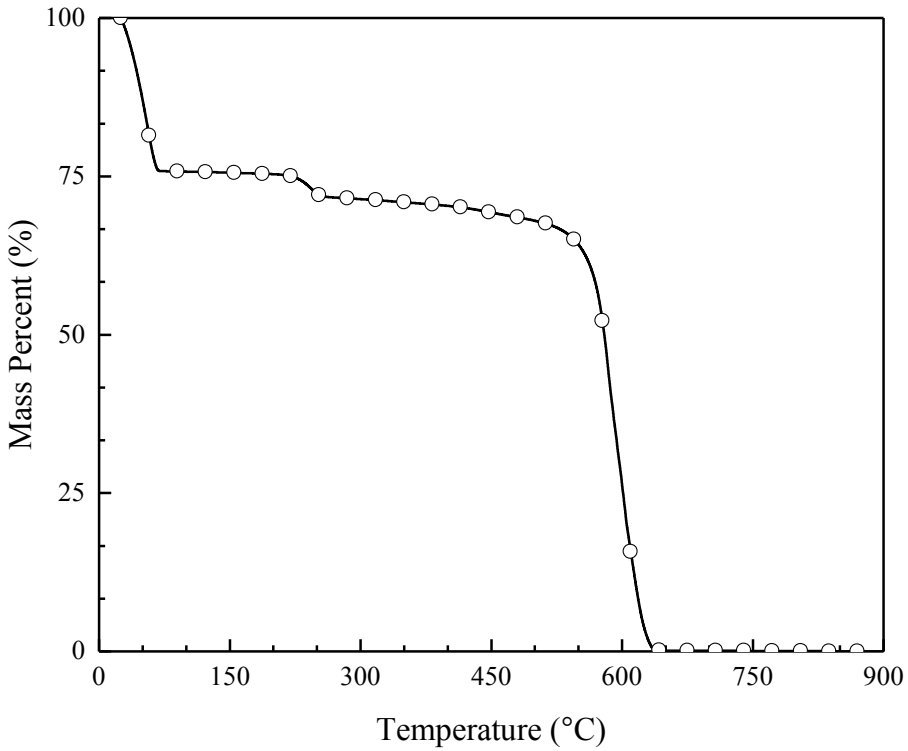

Figure 5.7: The plot illustrates the burn out process of carbon black, starting at room temperature (~20°C) until about 900°C. As can be seen in the graph, that there is 0% remaining after ~615°C.

5.4.3 Ca^{2+} and PO_4 concentration analysis

The calcium and phosphate concentration (mg\dL) of scaffold dissolution in Tris-HCl solution is summarized in Figure 5.8, Figure 5.9, Figure 5.10 and Table 5.8. Figure 5.8 and Figure 5.9 are the representation of Ca^{2+} and PO_4^{3-}, respectively. The graphs initially start at time point 0 hours, which was used as initial, in analysis for both calcium and phosphate, for calcium the 100% HA scaffold groups show the greatest concentraion of Ca^{2+} ions (~1.9 mg/dL), but eventuially release at a slower rate, which can be seen at hour 336 (day 14), that the 100% HA scaffold have the least amount of calcium ions released. On the other end of the spectrum, the 100% β-TCP has the highest concentration released with approxiamtely 7.6 mg/dL measured (Table 5.8). The 15/85% HA/β-TCP scaffold group, fell in between the 100% HA and 100% β-TCP groups, and at day 14 had a Ca^{2+} ion release of approximately 5.95 mg/dL (Table 5.8).

While the PO_4^{3-} ion showed similar trends as those in Ca^{2+} the one apparent difference was with the 100% HA scaffold group. There was almost 0 mg/dL of the phosphate ion released in the first 24 hours, in comparison to the how much Ca^{2+} ions released in that same time frame. The 100% HA group eventually did end up having a release of approximately 5.1 mg/dL at day 14 but it was short of what the other three groups (100% β-TCP, 15/85% HA/β-TCP, and 15/85%

HA/β-TCP (design)) released in those same 336 hours. 100% β-TCP, 15/85% HA/β-TCP, and 15/85% HA/β-TCP (design) followed the same trend, and at day 14, they all had an average PO_4^{3-} ion concentration of ~8.61 mg/dL, with no significant differences between these three experimental scaffold compositions (Figure 5.9).

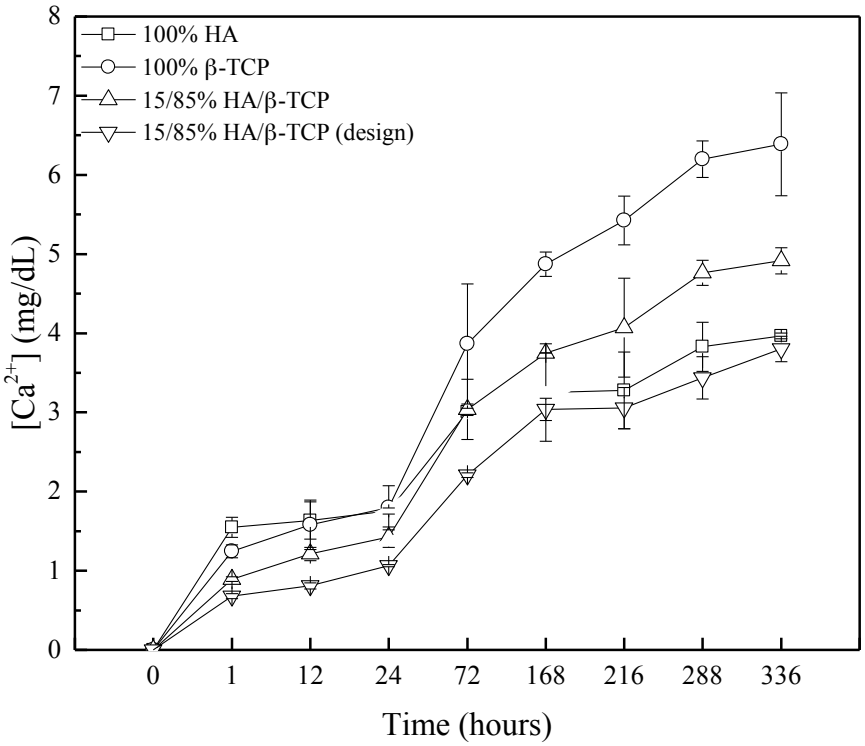

Figure 5.8: Ca^{2+} concentration in 0.05 mol/L Tris buffer after immersion of 100% HA, 100% β-TCP, 15/85% HA/β-TCP, and 15/85% HA/β-TCP (design) for time periods ranging from 1 hour to 336 hours (14 days).

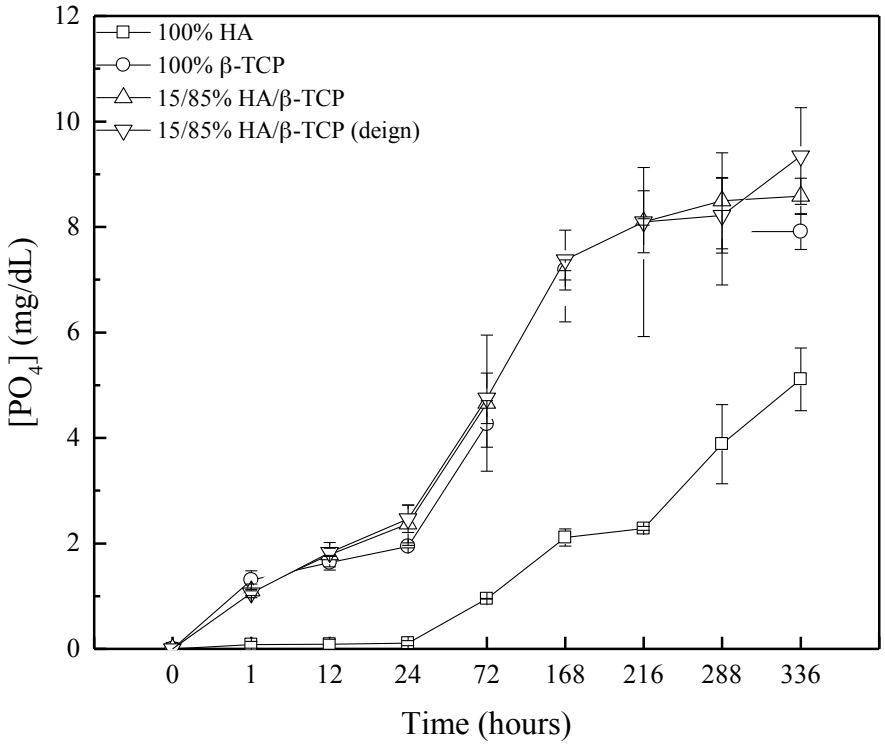

Figure 5.9: PO_4^{3-} concentration in 0.05 mol/L Tris buffer after immersion of 100% HA, 100% β-TCP, 15/85% HA/β-TCP, and 15/85% HA/β-TCP (design) for time periods ranging from 1 hour to 336 hours (14 days).

Group	Element(s)	Time (hour(s))							
		1	12	24	72	168	216	288	336
Monophasic									
HA	Ca^{2+}	1.864	1.971	2.015	3.874	2.463	3.659	4.540	4.469
		(0.13)	(0.24)	(0.04)	(0.05)	(0.62)	(0.48)	(0.31)	(0.04)
	$(PO_4)^{3-}$	0.079	0.089	0.108	0.952	2.112	2.284	3.882	5.112
		(0.06)	(0.09)	(0.05)	(0.00)	(0.17)	(0.04)	(0.75)	(0.59)
β-TCP	Ca^{2+}	1.485	2.015	2.256	5.250	5.675	6.129	7.349	7.632
		(0.08)	(0.31)	(0.28)	(0.76)	(0.15)	(0.31)	(0.23)	(0.65)
	$(PO_4)^{3-}$	1.304	1.636	1.939	4.265	7.183	7.525	7.912	7.912
		(0.18)	(0.14)	(0.03)	(0.44)	(0.19)	(1.59)	(0.34)	(1.01)
Biphasic									
HA/β-TCP	Ca^{2+}	1.044	1.318	1.606	3.601	4.245	4.621	5.510	5.947
		(0.03)	(0.08)	(0.13)	(0.38)	(0.03)	(0.62)	(0.16)	(0.16)
	$(PO_4)^{3-}$	1.099	1.788	2.367	4.659	6.685	8.097	8.496	8.581
		(0.13)	(0.23)	(0.36)	(1.29)	(0.48)	(0.06)	(0.91)	(0.34)
HA/β-TCP (design)	Ca^{2+}	0.770	0.914	1.215	2.555	3.465	3.426	4.038	4.437
		(0.03)	(0.04)	(0.01)	(0.03)	(0.14)	(0.26)	(0.27)	(0.16)
	$(PO_4)^{3-}$	1.056	1.830	2.468	4.752	7.373	8.097	8.221	9.346
		(0.05)	(0.08)	(0.26)	(0.48)	(0.57)	(0.59)	(0.72)	(0.92)

Table 5.8: Ca^{2+} and $\left(PO_4^{3-}\right)$ mean concentration (mg/dL) as released from the mono- and bi-phasic scaffold groups, the standard deviations (S.D.) are noted in parentheses.

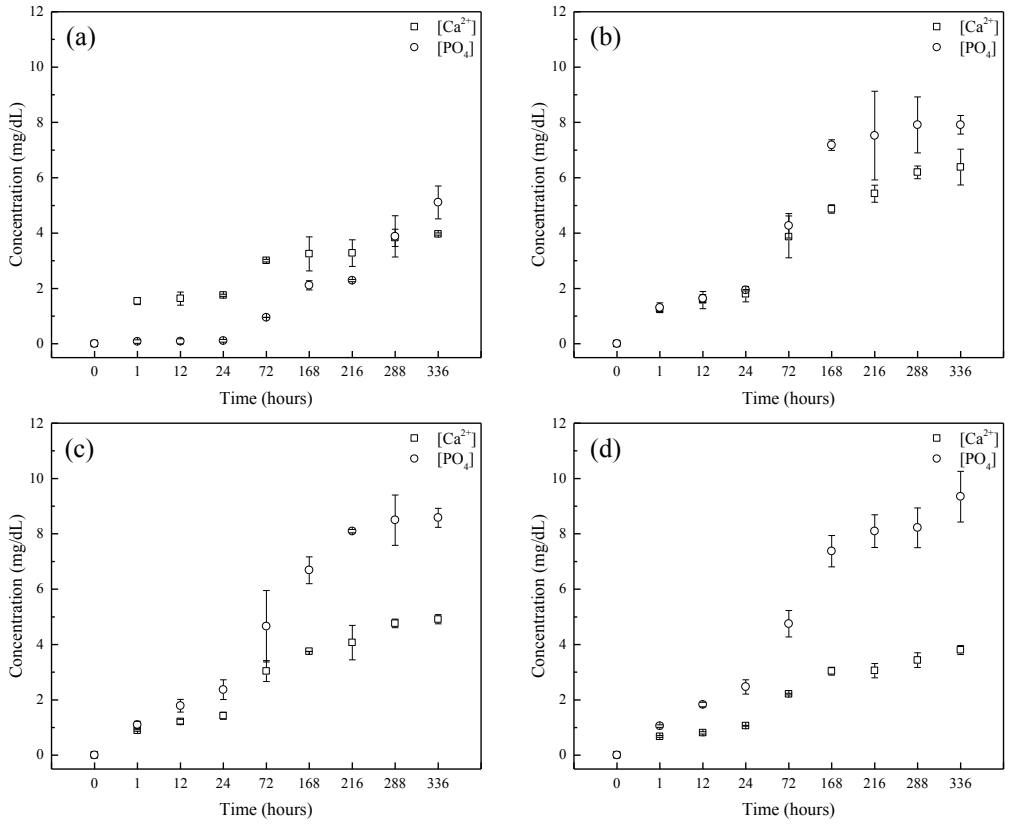

Figure 5.10: Comparing the Ca^{2+} and PO_4^{3-} concentration in 0.05 mol/L Tris buffer after immersion for time periods ranging from 1 hour to 336 hours (14 days) for (a) 100% HA, (b) 100% β-TCP, (c) 15/85% HA/β-TCP, and (d) 15/85% HA/β-TCP (design).

The kinetic rate law for dissolution is:

$$\frac{dC}{dt} = k_D \left[\frac{K_{SO}\text{-}IP}{K_{SO}}\right]^n \qquad (5.4.1)$$

C = molar quantity being dissolved

t = time

k_D = a constant

n = kinetic rate order

$\frac{K_{SO}\text{-}IP}{K_{SO}}$ = relative under saturation

But the dissolution has been found to be easier when simplified to the equation as follows:

$$\log[Ca] = A_0 + A_1 \log t \tag{5.4.2}$$

This equation is related to the rate equation:

$$\frac{d[Ca]}{dt} = k \cdot t^m \tag{5.4.3}$$

$[Ca] = Ca^{2+}$ concentration in solution

k = constant

m = effective order of the reaction

To followed by the equation:

$$[Ca] = \left(k/m + 1\right) \cdot t^{m+1} \tag{5.4.4}$$

Or

$$\log[Ca] = \log\left(k/m + 1\right) + (m+1) \cdot \log t \tag{5.4.5}$$

$$A_0 = \log\left(k/m + 1\right)$$

$$A_1 = (m+1)$$

5.4.4 Scaffold Morphology and Schwann cell growth (in collaboration with Stanford University)

Cell alignment data showed a correlation between cell orientation and the scaffold at two time points (7 and 14 days *in vitro*). Cell directionality was derived from the angle of the cell nuclei measured in relation to the strut (Figure 5.11b). It was found that the majority of cells on the scaffold grew at an angle between 0° and 30° off-parallel from the struts. This parallelism with the scaffold's internal configuration was seen to have a tight connection at day 7 and 14, where ~30% of cells were within 10° of parallel with the strut and nearly 55% of cells are within 20° (Figure 5.13). By day 14, the effect on directionality was still apparent by the scaffolds with the percentages within a similar range in comparison to the two time points. The data (Figure 5.13) and images (Figure 5.12) suggest that the struts of the 3D printed scaffolds facilitate the movement of the cells along the surface.

The cytotoxicity assay results (Figure 5.12) indicated that the Schwann cells (SCs) propagated on the individual struts of the scaffold with a negligible amount of dead cells present

at the indicated time points *in vitro*, in comparison to the control group. While the staining for S100-β and $p75^{LNGR}$ proteins (Figure 5.14) presented positive results for both of the proteins. The positive results suggest that the β-TCP does not affect the Schwann cells, ultimately meaning that these cells are capable of growing along the β-TCP struts, while still executing their functions [154].

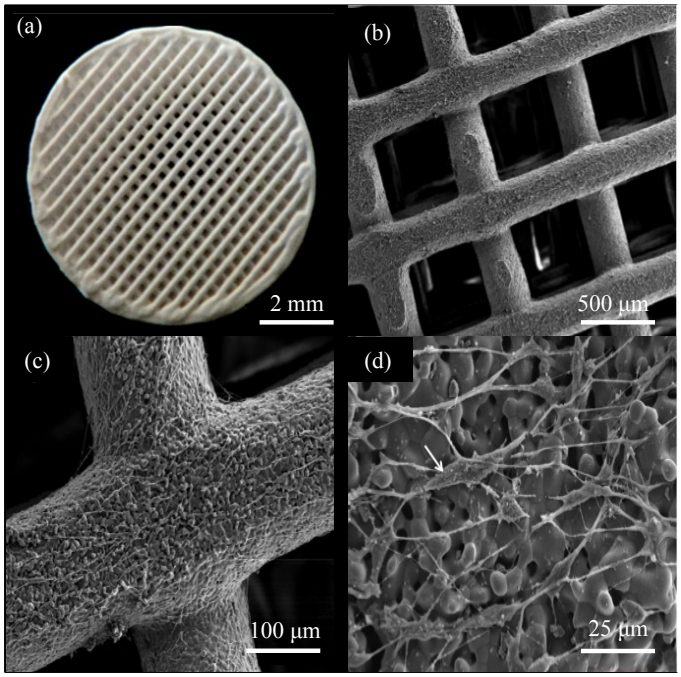

Figure 5.11: (a and b) Digital image and SEM image, respectively, of a scaffold used for the cell directionality study. (c and d) images which show intersection struts at 100 µm level and the surface at 25 µm level, respectively.

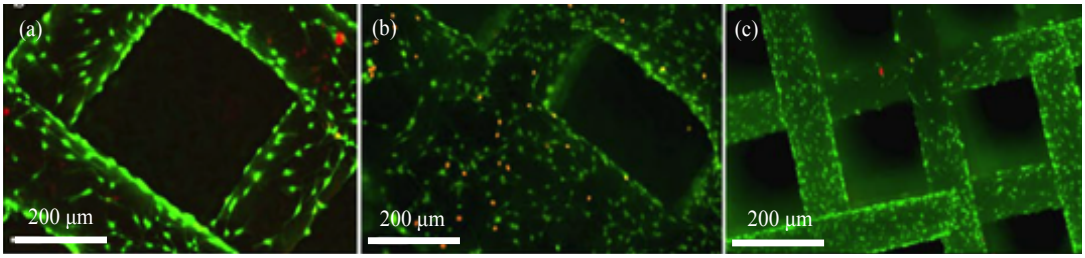

Figure 5.12: Fluorescent images of the cytotoxicity assay at (a) 3 days, (b) 7 days, and (c) 14 days. The staining indicated directed cell growth along the struts and in some areas clustered growth.

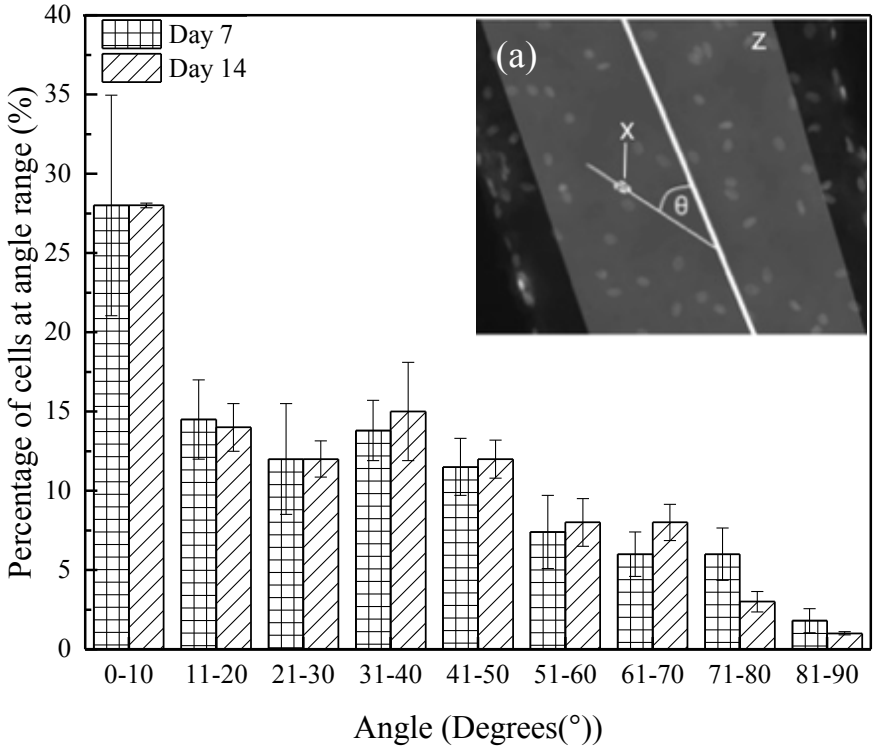

Figure 5.13: Results show the mean percentage of cells (and standard deviations) at a given range within a degree of the parallel scaffold struts. Insert (a) gives an example of the method of measuring the angle between the cell axis in relation to strut [154].

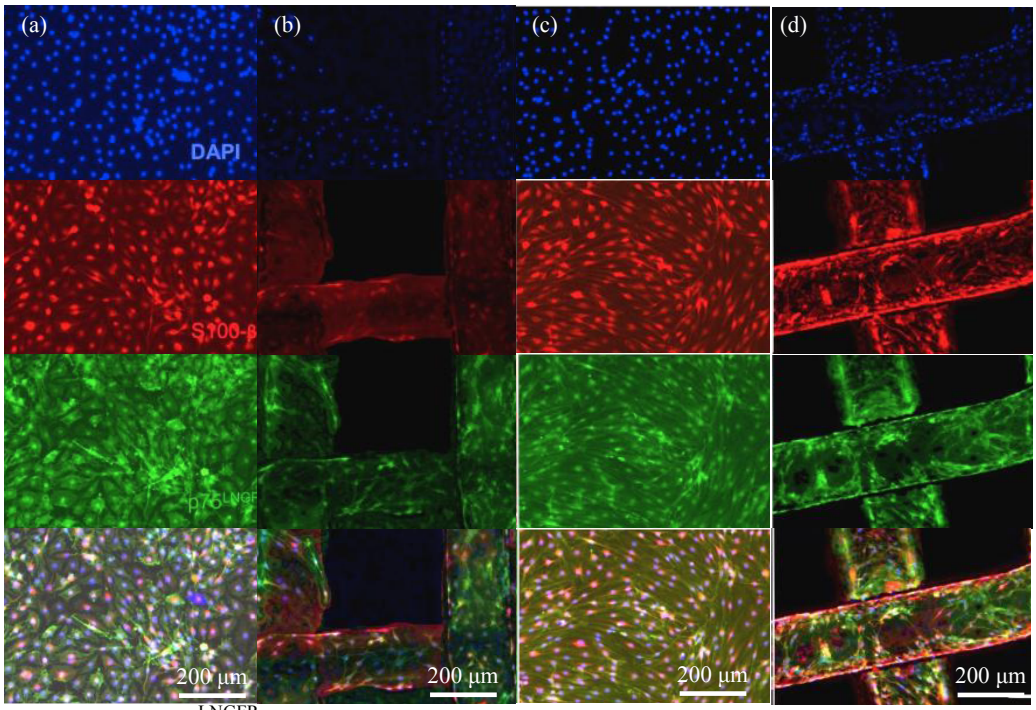

Figure 5.14: The $p75^{LNGFR}$ was stained green and the S100-β in red. Columns (a) and (b) are for the control and 100% β-TCP scaffold at 7 days, while (c) and (d) are at 14 days, respectively.

5.4.5 Preliminary In Vivo Work (in collaboration with New York University)

Reconstructed microCT (μCT 40, Scanco Medical, Switzerland) images of the scaffolds of the scaffolds at various time points *in vivo*, were used to examine for new bone formation. Images found in Figure 5.15, are representative of scaffolds found at 2 weeks (Figure 5.15a) and 24 weeks (Figure 5.15b) *in vivo*, respectively. From the reconstructed image it is seen that there is a greater amount of bone formation, remodeling, and integration at the longer time point, 24 weeks, in comparison to the 2 week time point.

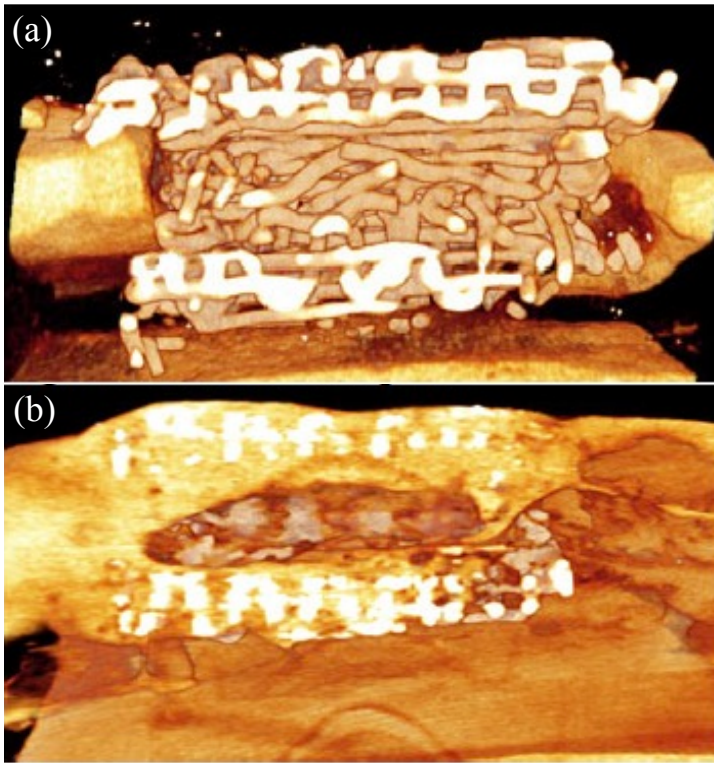

Figure 5.15: 3D microCT scans of 100% β-TCP scaffold at two time points *in vivo:* (a) 2 weeks and (b) 24 weeks.

5.5 Conclusion

The data and results from the aforementioned sections, as well as specific aim #1, with respect to dissolution results of the four experimental groups can vary. It should be noted that the study of these ceramic scaffolds have been used in a variety of biological studies, and not always does the *in vitro* result directly translate into the *in vivo* condition. The limitations of the *in vitro* testing should be reviewed and compared to the differences, which may be encountered in an *in vivo* environment since these *in vitro* experiments are modeled and constructed to simulate physiological conditions of the potential *in vivo* environment.

The data from the *in vitro* portion of this specific aim is in agreement with the findings in the overall scope of the dissertation. Taking the 100% HA and 100% β-TCP as controls and the two 15/85% HA/β-TCP groups as the experimental, the results are similar to what was expected. Literature indicates the bulk or pressed powder properties of this two materials, but does not present the biphasic mixture release for Ca^{2+} or PO_4 in an *in vitro* setting. The results indicate the trend which, the rate of calcium and phosphate ion release should fall greater than 100% HA but beloe 100% β-TCP. This can be seen when looking at the results and further identified with the extrapolation of data from previous bulk property results.

The *in vitro* analysis of ion release in a SBF solution also has been collaborated with work done along with Yang et al, with regards to cytotoxicity. The cytotoxicity assay results indicated that the 100% β-TCP material which is most commonly used did not have a significant effect or do much altering to the Schwann cells *in vitro*, nor did it have any negatively alter the expression of the $p75^{LNGFR}$ or S100-β proteins in those Schwann cells. These findings lead to the conclusion that the 100% β-TCP material of which the scaffolds are fabricated from as a capable material to facilitate the stimulation of nerve related functionality into a ceramic bone scaffold. In addition the alignment data displays the scaffolds individualized struts ability to direct the Schwann cells along its surface with results yielding that nearly 10% of the cells are within 10° of being parallel with the strut.

With the ability of the material (100% β-TCP) to support the alignment of the Schwann cells, in conjunction with its nearly nonexistent cytotoxicity, permitted for the next step of an *in vivo* experiment. The alignment of the cells gives the evidence that when a scaffold is placed in a long bone critical sized defect model, the cells will move longitudinally from one end to the other and facilitate the bone growth process. The ceramic phosphate based scaffolds needed to exhibit and mimic cellular regeneration as well as mechanical properties of the host to lead to a successful bone healing [2]. Scaffolds, which were implanted, showed minimal new bone formation at earlier time points *in vivo*, while longer time points (i.e. 24 weeks) showed moderate bone formation and integration. These long bone scaffolds implanted as is showed promising results at their respective time points, but in the future these scaffolds can be either coated or filled with different components, which can be slowly released, such as a growth factor. The combined results from the *in vitro* and *in vivo* portions give a better interpretation of the possibilities that can be achieved with utilization of 3D printed long bone scaffolds used with Schwann cells. The alignment provided by the struts and in combination with the benefits of Schwann cells has the potential to advance the vascularization of calcium phosphate based scaffolds, in turn providing a quicker and more established angiogenesis [154].

CHAPTER 6
CONCLUSIONS

Calcium phosphate based scaffolds composed of hydroxyapatite (HA), β-tri-calcium phosphate (β-TCP), or a combination of both (HA/β-TCP) were investigated as materials for three-dimensional printing process to create layer-by-layer structures for use as bone regeneration scaffolds. Commercially available ceramic powders were beneficiated and combined with commercially available process additives to produce colloidal gels/inks. These inks were printed and sintered to produce scaffolds.

Chapter 1 of this dissertation introduced three research questions:

1. Is the composition and spatial distribution of the materials in the sintered ceramic scaffold able to be controlled?
2. Do the details of printing (i.e., pre-mixed composition ink, two-tip deposition of different ink compositions or blending inks with a mixing chamber while printing) affect the in vitro response of the scaffold on the macroscopic scale?
3. Can 3D printing be used to tailor the scaffold to induce bone healing in long-bone defects, in addition to control of dissolution kinetics?

Chapter 2 reviewed the literature relevant to selection of ceramic materials used for potential bone regenerative scaffolds. The standard of medical care in the use of hydroxyapatite and β-TCP includes implant of porous, friable scaffolds. As-such, current bone repair scaffolds are non-load bearing but do provide a microenvironment suitable for osteogenesis and resorption of the scaffolds. HA and β-TCP have also been blended to create biphasic calcium phosphates, which have shown intermediate solubility between the solubility of the two components.

Chapter 3 addressed an important, fundamental step in design of printable inks for the robocasting process. Namely, does the beneficiation of the commercial powders and the subsequent processing change the physicochemical properties of the sintered ceramic parts? The XRD and FT-IR spectra results show that indeed the final ceramic scaffolds have the same crystal structure and functional groups, respectively, as one would expect if simply blending the raw powders together at the same ratio. There was some small deviation from the expected which

occurred in the BCP (15/85% HA/β-TCP) experimental group with the finding of trivial amounts of calcium pyrophosphate (CPP), which was confirmed with XRD and FT-IR analysis. The CPP phase, although not detrimental to the host in small quantities, does have a speedy dissolution rate, which is greater than that of β-TCP. With a faster dissolution such as that associated with CPP, the Ca2+ and PO4 ion release will occur at a faster rate. The CPP phase is not present in the 100% HA or 100% β-TCP scaffolds, leading to the conclusion that a reaction between the two phases at the higher heating temperatures leads to this by-product. Therefore, it can be concluded that the robocasting process does not impact the physicochemical properties of these particular ceramics.

Chapter 4 focused on the ability to adapt the 3D printing process and the colloidal pastes to create tailored scaffolds. The primary focus of the chapter was the 'mixedness' of the materials, further looking into the powder mixing, which offers the ability to use multiple materials in a 'pre-blended' fashion. In this part, alumina and zirconia, had to be substituted in place of hydroxyapatite and β-TCP, to allow for the imaging analysis, as HA and β-TCP are composed of the similar basic components there would be a difficulty in differentiation. The results from the colloidal gels mixed in powder form, which yielded the pre-blended paste, were more evenly distributed across the sample area when compared to those mixed in their paste through the mixer prior to deposition. The radial distribution function (RDF) confirmed what was visualized in the backscatterd SEM images. Even though the RDF results indicated poor mixing and particle distribution the refinement results were found to be promising, the ratios were within 5% of their designed ratio. These two approaches to fabricating the scaffold ((1) nozzle array and (2) mixing nozzle) offer further ability to tailor these scaffolds and print intricate designs to facilitate with the bone remodeling process. The dispersion of the two basic materials to create a biphasic model allows for the tailoring of the dissolution of the material (HA<<TCP) in addition to the mechanical integrity (HA>>β-TCP).

Chapter 5 merged the results from characterization and in vitro investigation while including some preliminary in vivo data. The in vitro data with regards to the calcium (Ca2+) and (PO4) results were in agreement with literature where β-TCP dissolves at a faster rate in comparison to HA. These results of calcium and phosphate release were different and more apparent than the in vitro weight loss done in chapter 3, indicating that weight loss in a SBF is not a sufficient enough method to determine the overall success for in vivo. Additionally the cytotoxicity assay results indicated that the CaP based materials which are most commonly used did not have a significant effect to the Schwann cells (SCs) in vitro, nor did it negatively alter the expression of the p75LNGFR or S100-β proteins in those Schwann cells. These Ca2+/PO4 along

the cytotoxicity results in conjunction with the ability for the struts of the scaffold to conduct the cells nearly parallel along the surface gives the potential to successfully transport cells from one end of the scaffold to the other. This promising result can narrow the gap and lead to numerous possibilities when it comes to fixing critical sized defects. With the combination of the preliminary in vitro data and previous in vivo work, lead to the initial attempt of a critical sized long bone defect. The primary histology and microCT data have shown bone formation along the surface of the long bone replacement scaffold as early as 4 weeks with significant bone growth at the 24 weeks in vivo.

The work done within the scope of this dissertation and its aim to answer the three primary research questions, indicates that robocasting is a viable tool for the designing and fabrication of calcium phosphate based ceramic scaffolds to facilitate in the bone replacement process. In conclusion this particular research led to an increase in knowledge in biological, chemical and scientific areas and provides a solid basis for future development and direction to further explore novel ideas in the area of 3D printing scaffolds for bone regeneration.

CHAPTER 7

FUTURE RECOMMENDATIONS

Although the work done for the completion of the degree was thorough, a continued investigation is highly encouraged to further evolve the adaptability of this method and its materials. The work done was a step in the right direction, with regards to the *in vitro* and preliminary *in vivo* study. The results showed promise and also at the same time opened doors to other possibilities. At the time more work needs to be completed into the mixing nozzle, as is evident in the RDF and SEM images, the mixing although quantitatively is there with two phases, while the mixing of particles is far from ideal. It is of significance to further explore the mixing paddle, chamber, speed of printing, and potentially the properties of the colloidal gels. This 'mixedness' may be sufficient in its current state or possibly detrimental, a study focusing on comparing the current state of mixing *in vitro* with that of the powder mixing would give crucial information and direction with regards to the area of its future, while possibly leading to further realization of addressing the potential capability for angiogenesis.

CHAPTER 8

REFERENCES

1. Cowin SC. Bone mechanics handbook. 2001.

2. Bose S, Vahabzadeh S, Bandyopadhyay A. Bone tissue engineering using 3D printing. Materials Today. 2013;16(12):496-504.

3. Bandyopadhyay A, Bose S. Characterization of biomaterials: Newnes; 2013.

4. Albrektsson T, Johansson C. Osteoinduction, osteoconduction and osseointegration. European Spine Journal. 2001;10(2):S96-S101.

5. Buckwalter J, Glimcher M, Cooper R, Recker R. Bone biology. J Bone Joint Surg Am. 1995;77(8):1256-75.

6. Precheur HV. Bone graft materials. Dental Clinics of North America. 2007;51(3):729-46.

7. Mouriño V, Boccaccini AR. Bone tissue engineering therapeutics: controlled drug delivery in three-dimensional scaffolds. Journal of the Royal Society Interface. 2009:rsif20090379.

8. Jones AC, Arns CH, Sheppard AP, Hutmacher DW, Milthorpe BK, Knackstedt MA. Assessment of bone ingrowth into porous biomaterials using MICRO-CT. Biomaterials. 2007;28(15):2491-504.

9. Seitz H, Rieder W, Irsen S, Leukers B, Tille C. Three‐dimensional printing of porous ceramic scaffolds for bone tissue engineering. Journal of Biomedical Materials Research Part B: Applied Biomaterials. 2005;74(2):782-8.

10. Witek L, Smay J, Silva NR, Guda T, Ong JL, Coelho PG. Sintering effects on chemical and physical properties of bioactive ceramics. Journal of Advanced Ceramics. 2013;2(3):274-84.

11. Salgado AJ, Coutinho OP, Reis RL. Bone tissue engineering: state of the art and future trends. Macromolecular bioscience. 2004;4(8):743-65.

12. Lundgren D, Nyman S, Mathisen T, Isaksson S, Klinge B. Guided bone regeneration of cranial defects, using biodegradable barriers: an experimental pilot study in the rabbit. Journal of Cranio-Maxillofacial Surgery. 1992;20(6):257-60.

13. Fialkov J, Holy C, Antonyshyn O. Strategies for bone substitutes in craniofacial surgery. Bone Engineering 1st ed Toronto, Ontario, Canada: Em Squared Inc. 2000:548-56.

14. Mastrogiacomo M, Muraglia A, Komlev V, Peyrin F, Rustichelli F, Crovace A, et al. Tissue engineering of bone: search for a better scaffold. Orthodontics & craniofacial research. 2005;8(4):277-84.

15. Schieker M, Seitz H, Drosse I, Seitz S, Mutschler W. Biomaterials as scaffold for bone tissue engineering. European journal of trauma. 2006;32(2):114-24.

16. Moore WR, Graves SE, Bain GI. Synthetic bone graft substitutes. ANZ journal of surgery. 2001;71(6):354-61.

17. Russias J, Saiz E, Deville S, Gryn K, Liu G, Nalla R, et al. Fabrication and in vitro characterization of three‐dimensional organic/inorganic scaffolds by robocasting. Journal of Biomedical Materials Research Part A. 2007;83(2):434-45.

18. Karageorgiou V, Kaplan D. Porosity of 3D biomaterial scaffolds and osteogenesis. Biomaterials. 2005;26(27):5474-91.

19. Hench LL. Introduction to bioceramics. Adv Ser Ceram. 1993;1:1-24.

20. Cesarano J, Dellinger JG, Saavedra MP, Gill DD, Jamison RD, Grosser BA, et al. Customization of Load‐Bearing Hydroxyapatite Lattice Scaffolds. International Journal of Applied Ceramic Technology. 2005;2(3):212-20.

21. Stocum DL. Regenerative biology and engineering: strategies for tissue restoration. Wound Repair and Regeneration. 1998;6(4):276-90.

22. Kivrak N, Taş AC. Synthesis of Calcium Hydroxyapatite‐Tricalcium Phosphate (HA‐TCP) Composite Bioceramic Powders and Their Sintering Behavior. Journal of the American Ceramic Society. 1998;81(9):2245-52.

23. Currey J. Biomaterials: sacrificial bonds heal bone. Nature. 2001;414(6865):699-.

24. LeGeros RZ. Properties of osteoconductive biomaterials: calcium phosphates. Clinical orthopaedics and related research. 2002;395:81-98.

25. Ripamonti U, Ma S, Reddi A. The critical role of geometry of porous hydroxyapatite delivery system in induction of bone by osteogenin, a bone morphogenetic protein. Matrix. 1992;12(3):202-12.

26. Barralet J, Fleming G, Campion C, Harris J, Wright A. Formation of translucent hydroxyapatite ceramics by sintering in carbon dioxide atmospheres. Journal of materials science. 2003;38(19):3979-93.

27. Fathi M, Hanifi A, Mortazavi V. Preparation and bioactivity evaluation of bone-like hydroxyapatite nanopowder. Journal of materials processing technology. 2008;202(1):536-42.

28. LeGeros R, editor Variability of HAP/b-TCP ratios in sintered apatites. Journal of Dental Research; 1986: AMER ASSOC DENTAL RESEARCH 1619 DUKE ST, ALEXANDRIA, VA 22314.

29. Legeros RZ. Biodegradation and bioresorption of calcium phosphate ceramics. Clinical materials. 1993;14(1):65-88.

30. Bouler J-M, LeGeros RZ, Daculsi G. Biphasic calcium phosphates: influence of three synthesis parameters on the HA/ß-TCP ratio. J Biomed Mater Res. 2000;51(4):680-4.

31. Daculsi G, LeGeros R, Nery E, Lynch K, Kerebel B. Transformation of biphasic calcium phosphate ceramics in vivo: ultrastructural and physicochemical characterization. Journal of biomedical materials research. 1989;23(8):883-94.

32. Julien M, Khairoun I, LeGeros RZ, Delplace S, Pilet P, Weiss P, et al. Physico-chemical–mechanical and in vitro biological properties of calcium phosphate cements with doped amorphous calcium phosphates. Biomaterials. 2007;28(6):956-65.

33. Yaszemski MJ, Payne RG, Hayes WC, Langer R, Mikos AG. Evolution of bone transplantation: molecular, cellular and tissue strategies to engineer human bone. Biomaterials. 1996;17(2):175-85.

34. Rey C, Combes C, Drouet C, Grossin D. Bioactive ceramics: physical chemistry. Comprehensive Biomaterials. 2011;1:187-221.

35. El-Ghannam A, Ducheyne P. Bioactive Ceramics. Comprehensive Biomaterials. Metallic, Ceramic and Polymeric Biomaterials, Charlotte. 2011:157-79.

36. Kannan S, Goetz‐Neunhoeffer F, Neubauer J, Ferreira J. Ionic Substitutions in Biphasic Hydroxyapatite and β‐Tricalcium Phosphate Mixtures: Structural Analysis by Rietveld Refinement. Journal of the American Ceramic Society. 2008;91(1):1-12.

37. Saiz E, Gremillard L, Menendez G, Miranda P, Gryn K, Tomsia AP. Preparation of porous hydroxyapatite scaffolds. Materials Science and Engineering: C. 2007;27(3):546-50.

38. Miranda P, Saiz E, Gryn K, Tomsia AP. Sintering and robocasting of β-tricalcium phosphate scaffolds for orthopaedic applications. Acta biomaterialia. 2006;2(4):457-66.

39. Dorozhkin SV. Biphasic, triphasic and multiphasic calcium orthophosphates. Acta biomaterialia. 2012;8(3):963-77.

40. Hutmacher DW. Scaffolds in tissue engineering bone and cartilage. Biomaterials. 2000;21(24):2529-43.

41. Leong K, Cheah C, Chua C. Solid freeform fabrication of three-dimensional scaffolds for engineering replacement tissues and organs. Biomaterials. 2003;24(13):2363-78.

42. Li W-J, Cooper JA, Mauck RL, Tuan RS. Fabrication and characterization of six electrospun poly (α-hydroxy ester)-based fibrous scaffolds for tissue engineering applications. Acta biomaterialia. 2006;2(4):377-85.

43. GRAFTS IB. Three-dimensionally engineered hydroxyapatite ceramics with interconnected pores as a bone substitute and tissue engineering scaffold. Biomaterials in orthopedics. 2004:287.

44. Liao CJ, Chen CF, Chen JH, Chiang SF, Lin YJ, Chang KY. Fabrication of porous biodegradable polymer scaffolds using a solvent merging/particulate leaching method. Journal of biomedical materials research. 2002;59(4):676-81.

45. Nam YS, Park TG. Biodegradable polymeric microcellular foams by modified thermally induced phase separation method. Biomaterials. 1999;20(19):1783-90.

46. Shi D. Introduction to biomaterials: World Scientific; 2006.

47. Kalita SJ, Bose S, Hosick HL, Bandyopadhyay A. Development of controlled porosity polymer-ceramic composite scaffolds via fused deposition modeling. Materials Science and Engineering: C. 2003;23(5):611-20.

48. Chen Z, Li D, Lu B, Tang Y, Sun M, Xu S. Fabrication of osteo-structure analogous scaffolds via fused deposition modeling. Scripta materialia. 2005;52(2):157-61.

49. Bellini A, Shor L, Guceri SI. New developments in fused deposition modeling of ceramics. Rapid Prototyping Journal. 2005;11(4):214-20.

50. Griffith ML, Halloran JW. Freeform fabrication of ceramics via stereolithography. Journal of the American Ceramic Society. 1996;79(10):2601-8.

51. Smay JE, Gratson GM, Shepherd RF, Cesarano J, Lewis JA. Directed colloidal assembly of 3D periodic structures. Advanced Materials. 2002;14(18):1279-83.

52. Smay JE, Nadkarni SS, Xu J. Direct writing of dielectric ceramics and base metal electrodes. International journal of applied ceramic technology. 2007;4(1):47-52.

53. Zhu C. Shape Evolution of 3d Periodic Structure Fabricated by Direct-write Assembly of Concentrated Colloidal Gels: Oklahoma State University; 2010.

54. Lewis JA, Smay JE, Stuecker J, Cesarano J. Direct Ink Writing of Three‐Dimensional Ceramic Structures. Journal of the American Ceramic Society. 2006;89(12):3599-609.

55. Lewis JA, Gratson GM. Direct writing in three dimensions. Materials today. 2004;7(7):32-9.

56. Lewis JA. Direct-write assembly of ceramics from colloidal inks. Current Opinion in Solid State and Materials Science. 2002;6(3):245-50.

57. Bruneaux J, Therriault D, Heuzey M-C. Micro-extrusion of organic inks for direct-write assembly. Journal of Micromechanics and Microengineering. 2008;18(11):115020.

58. Simon JL, Michna S, Lewis JA, Rekow ED, Thompson VP, Smay JE, et al. In vivo bone response to 3D periodic hydroxyapatite scaffolds assembled by direct ink writing. Journal of Biomedical Materials Research Part A. 2007;83(3):747-58.

59. Nadkarni SS, Smay JE. Concentrated barium titanate colloidal gels prepared by bridging flocculation for use in solid freeform fabrication. Journal of the American Ceramic Society. 2006;89(1):96-103.

60. Lawrence BJ, Madihally SV. Cell colonization in degradable 3D porous matrices. Cell adhesion & migration. 2008;2(1):9-16.

61. Mamidwar SS, Arena C, Kelly S, Alexander H, Ricci J. In vitro characterization of a calcium sulfate/PLLA composite for use as a bone graft material. Journal of Biomedical Materials Research Part B: Applied Biomaterials. 2007;81(1):57-65.

62. Cornell CN, Lane JM. Current understanding of osteoconduction in bone regeneration. Clinical orthopaedics and related research. 1998;355:S267-S73.

63. Ripamonti U. Smart biomaterials with intrinsic osteoinductivity: Geometric control of bone differentiation. bone engineering. 2000:215-22.

64. Ko C, Kohn D, Hollister S. Micromechanics of implant/tissue interfaces. The Journal of oral implantology. 1991;18(3):220-30.

65. Simmons C, Pilliar R. A biomechanical study of early tissue formation around bone-interfacing implants: the effect of implant surface geometry. Bone engineering Toronto: EM Squared Incorporated. 2000:369-80.

66. De Bruijn J, Yuan H, Dekker R, Layrolle P, De Groot K, Van Blitterswijk C. Osteoinductive biomimetic calcium-phosphate coatings and their potential use as tissue-engineering scaffolds. Bone engineering Toronto: em squared Inc. 2000:421-31.

67. Klawitter J, Hulbert S. Application of porous ceramics for the attachment of load bearing internal orthopedic applications. Journal of Biomedical Materials Research. 1971;5(6):161-229.

68. Schliephake H, Neukam F, Klosa D. Influence of pore dimensions on bone ingrowth into porous hydroxylapatite blocks used as bone graft substitutes: A histometric study. International journal of oral and maxillofacial surgery. 1991;20(1):53-8.

69. Pilliar R. Powder metal-made orthopedic implants with porous surface for fixation by tissue ingrowth. Clinical orthopaedics and related research. 1983;176:42-51.

70. Coelho PG, Coimbra ME, Ribeiro C, Fancio E, Higa O, Suzuki M, et al. Physico/chemical characterization and preliminary human histology assessment of a β-TCP particulate material for bone augmentation. Materials Science and Engineering: C. 2009;29(7):2085-91.

71. LeGeros RZ. Calcium phosphates in oral biology and medicine. Monographs in oral science. 1990;15:1-201.

72. Kokubo T. Bioceramics and their clinical applications: Elsevier; 2008.

73. Kokubo T, Takadama H. How useful is SBF in predicting in vivo bone bioactivity? Biomaterials. 2006;27(15):2907-15.

74. Rey C, Combes C, Drouet C, Grossin D. 1.111 - Bioactive Ceramics: Physical Chemistry. In: Ducheyne P, editor. Comprehensive Biomaterials. Oxford: Elsevier; 2011. p. 187-221.

75. Szpalski C, Nguyen PD, Vasiliu CEC, Chesnoiu-Matei I, Ricci JL, Clark E, et al. Bony engineering using time-release porous scaffolds to provide sustained growth factor delivery. Journal of Craniofacial Surgery. 2012;23(3):638-44.

76. Vasiliu CEC. Assembly of hydroxy apatite: beta tricalcium phosphate: Calcium sulfate bone engineering scaffolds: ProQuest; 2008.

77. Guda T, Walker JA, Singleton BM, Hernandez JW, Son J-S, Kim S-G, et al. Guided bone regeneration in long-bone defects with a structural hydroxyapatite graft and collagen membrane. Tissue Engineering Part A. 2012;19(17-18):1879-88.

78. Mijares D. Synthetic Bone Mineral (SBM): Prevention of Bone Loss Induced by Estrogen Deficiency in a Rat Model. New York: NYU College of Dentistry; 2009.

79. Taylor JC, Hinczak I. Rietveld made easy: a practical guide to the understanding of the method and successful phase quantifications: Sietronics Pty Limited; 2006.

80. Rietveld HM. The Rietveld method. The Early Days: a Retrospective View. The Rietveld Method Oxford University Press, Oxford, New York. 1993:39-42.

81. Nilen R, Richter P. The thermal stability of hydroxyapatite in biphasic calcium phosphate ceramics. Journal of Materials Science: Materials in Medicine. 2008;19(4):1693-702.

82. Houmard M, Fu Q, Genet M, Saiz E, Tomsia AP. On the structural, mechanical, and biodegradation properties of HA/β‐TCP robocast scaffolds. Journal of Biomedical Materials Research Part B: Applied Biomaterials. 2013;101(7):1233-42.

83. Daculsi G. Biphasic calcium phosphate concept applied to artificial bone, implant coating and injectable bone substitute. Biomaterials. 1998;19(16):1473-8.

84. Amera A, Abudalazez AM, Ismail RA, Razak AHN, Masudi MS, Kasim RS, et al. Synthesis and characterization of porous biphasic calcium phosphate scaffold from different porogens for possible bone tissue engineering applications. Science of Sintering. 2011;43(2):183-92.

85. Berzina-Cimdina L, Borodajenko N. Research of calcium phosphates using Fourier transform infrared spectroscopy: INTECH Open Access Publisher; 2012.

86. Ślósarczyk A, Paluszkiewicz C, Gawlicki M, Paszkiewicz Z. The FTIR spectroscopy and QXRD studies of calcium phosphate based materials produced from the powder precursors with different CaP ratios. Ceramics International. 1997;23(4):297-304.

87. Greiner-Wronowa E, Paluszkiewicz C, Stoch L. Applying FTIR spectroscopy in the study of archeometric sensor glasses. Journal of molecular structure. 1999;511:199-204.

88. Filgueiras MRT, La Torre G, Hench LL. Solution effects on the surface reactions of three bioactive glass compositions. Journal of biomedical materials research. 1993;27(12):1485-93.

89. Zhou J, Zhang X, Chen J, Zeng S, De Groot K. High temperature characteristics of synthetic hydroxyapatite. Journal of materials science: materials in medicine. 1993;4(1):83-5.

90. Wang PE, Chaki T. Sintering behaviour and mechanical properties of hydroxyapatite and dicalcium phosphate. Journal of Materials Science: Materials in Medicine. 1993;4(2):150-8.

91. Ramesh S, Tan C, Bhaduri S, Teng W, Sopyan I. Densification behaviour of nanocrystalline hydroxyapatite bioceramics. Journal of materials processing technology. 2008;206(1):221-30.

92. Liu H, Chin T, Lai L, Chiu S, Chung K, Chang C, et al. Hydroxyapatite synthesized by a simplified hydrothermal method. Ceramics International. 1997;23(1):19-25.

93. Trombe J, Montel G. Some features of the incorporation of oxygen in different oxidation states in the apatitic lattice—I On the existence of calcium and strontium oxyapatites. Journal of Inorganic and Nuclear Chemistry. 1978;40(1):15-21.

94. Raynaud S, Champion E, Bernache-Assollant D, Thomas P. Calcium phosphate apatites with variable Ca/P atomic ratio I. Synthesis, characterisation and thermal stability of powders. Biomaterials. 2002;23(4):1065-72.

95. Hench LL. Introduction to Bioceramics. Adv Ser Ceramic. 1993;1:1-24.

96. Coelho PG, Coimbra ME, Ribeiro C, Fancio E, Higa O, Suzuki M, et al. Physico/chemical characterization and preliminary human histology assessment of a [beta]-TCP particulate material for bone augmentation. Materials Science and Engineering: C. 2009;29(7):2085-91.

97. Bottino MC, Coelho PG, Henriques VA, Higa OZ, Bressiani AH, Bressiani JC. Processing, characterization, and in vitro/in vivo evaluations of powder metallurgy processed Ti‐13Nb‐13Zr alloys. Journal of Biomedical Materials Research Part A. 2009;88(3):689-96.

98. LeGeros RZ, Lin S, Rohanizadeh R, Mijares D, LeGeros JP. Biphasic calcium phosphate bioceramics: preparation, properties and applications. Journal of Materials Science: Materials in Medicine. 2003;14(3):201-9. doi: 10.1023/A:1022872421333.

99. Urist MR. Bone: Formation by Autoinduction. Science. 1965;150(3698):893-9. doi: 10.1126/science.150.3698.893.

100. Kenley RA, Yim K, Abrams J, Ron E, Turek T, Marden LJ, et al. Biotechnology and bone graft substitutes. Pharmaceutical research. 1993;10(10):1393-401.

101. Reddi AH. Morphogenesis and tissue engineering of bone and cartilage: inductive signals, stem cells, and biomimetic biomaterials. Tissue engineering. 2000;6(4):351-9.

102. Kuboki Y, Takita H, Kobayashi D, Tsuruga E, Inoue M, Murata M, et al. BMP‐induced osteogenesis on the surface of hydroxyapatite with geometrically feasible and nonfeasible structures: topology of osteogenesis. Journal of biomedical materials research. 1998;39(2):190-9.

103. Tressler J, Alkoy S, Dogan A, Newnham R. Functional composites for sensors, actuators and transducers. Composites Part A: Applied Science and Manufacturing. 1999;30(4):477-82.

104. Lee YJ, Braun PV. Tunable inverse opal hydrogel pH sensors. Advanced Materials. 2003;15(7‐8):563-6.

105. Van Blaaderen A, Ruel R, Wiltzius P. Template-directed colloidal crystallization. Nature. 1997;385(6614):321-4.

106. Therriault D, White SR, Lewis JA. Chaotic mixing in three-dimensional microvascular networks fabricated by direct-write assembly. Nature materials. 2003;2(4):265-71.

107. Joannopoulos JD, Villeneuve PR, Fan S. Photonic crystals: putting a new twist on light. Nature. 1997;386(6621):143-9.

108. Xie B, Parkhill RL, Warren WL, Smay JE. Direct Writing of Three‐Dimensional Polymer Scaffolds Using Colloidal Gels. Advanced Functional Materials. 2006;16(13):1685-93.

109. Sun W, Lal P. Recent development on computer aided tissue engineering—a review. Computer methods and programs in biomedicine. 2002;67(2):85-103.

110. Leukers B, Gülkan H, Irsen SH, Milz S, Tille C, Schieker M, et al. Hydroxyapatite scaffolds for bone tissue engineering made by 3D printing. Journal of Materials Science: Materials in Medicine. 2005;16(12):1121-4.

111. Iyer S. Design and Assembly of 3 Dimensional Hydroxyapatitie and β Tricalcium Phosphate Scaffolds with varied meso-pores: New York University; 2011.

112. Chen ZC, Ring TA, Lemaitre J. Stabilization and processing of aqueous BaTiO3 suspension with polyacrylic acid. Journal of the American Ceramic Society. 1992;75(12):3201-8.

113. Napper DH. Polymeric stabilization of colloidal dispersions: Academic Press London; 1983.

114. Cesarano J, Aksay IA, Bleier A. Stability of Aqueous α‐Al2O3 Suspensions with Poly (methacrylic acid) Polyelectrolyte. Journal of the American Ceramic Society. 1988;71(4):250-5.

115. Cesarano J, Aksay IA. Processing of Highly Concentrated Aqueous α‐Alumina Suspensions Stabilized with Polyelectrolytes. Journal of the American Ceramic Society. 1988;71(12):1062-7.

116. Michna S, Wu W, Lewis JA. Concentrated hydroxyapatite inks for direct-write assembly of 3-D periodic scaffolds. Biomaterials. 2005;26(28):5632-9.

117. Tovar N, Jimbo R, Witek L, Anchieta R, Yoo D, Manne L, et al. The physicochemical characterization and in vivo response of micro/nanoporous bioactive ceramic particulate bone graft materials. Materials Science and Engineering: C. 2014;43:472-80. doi: http://dx.doi.org/10.1016/j.msec.2014.07.048.

118. Clarke AR, Eberhardt CN. Microscopy techniques for materials science: Woodhead Publishing; 2002.

119. Reimer L. Scanning electron microscopy: physics of image formation and microanalysis. Measurement Science and Technology. 2000;11(12):1826.

120. Krinsley DH, Pye K, Boggs Jr S, Tovey NK. Backscattered scanning electron microscopy and image analysis of sediments and sedimentary rocks: Cambridge University Press; 2005.

121. Egerton R. Physical principles of electron microscopy: an introduction to TEM, SEM, and AEM: Springer Science & Business Media; 2006.

122. Grynpas MD, Bonar LC, Glimcher MJ. Failure to detect an amorphous calcium-phosphate solid phase in bone mineral: a radial distribution function study. Calcified tissue international. 1984;36(1):291-301.

123. LeGeros R, Parsons JR, Daculsi G, Driessens F, Lee D, Liu S, et al. Significance of the Porosity and Physical Chemistry of Calcium Phosphate Ceramics Biodegradation‐Bioresorption. Annals of the New York Academy of Sciences. 1988;523(1):268-71.

124. Heughebaert M, LeGeros R, Gineste M, Guilhem A, Bonel G. Physicochemical characterization of deposits associated with HA ceramics implanted in nonosseous sites. Journal of biomedical materials research. 1988;22(S14):257-68.

125. Ducheyne P, Radin S, King L. The effect of calcium phosphate ceramic composition and structure on in vitro behavior. I. Dissolution. Journal of biomedical materials research. 1993;27(1):25-34.

126. Duheyne P, Beight J, Cuckler J, Evans B, Radin S. Effect of calcium phosphate coating characteristics on early post-operative bone tissue ingrowth. Biomaterials. 1990;11(8):531-40.

127. Ducheyne P, Cuckler JM. Bioactive ceramic prosthetic coatings. Clinical orthopaedics and related research. 1992;276:102-14.

128. Radin S, Ducheyne P. Plasma spraying induced changes of calcium phosphate ceramic characteristics and the effect onin vitro stability. Journal of materials science: Materials in medicine. 1992;3(1):33-42.

129. de Groot K, Klein C, Wolke J, de Blieck-Hogervorst J. Plasma-sprayed coatings of calcium phosphate. CRC handbook of bioactive ceramics. 1990;2:133-42.

130. Babensee JE, McIntire LV, Mikos AG. Growth factor delivery for tissue engineering. Pharmaceutical research. 2000;17(5):497-504.

131. Oldham J, Lu L, Zhu X, Porter B, Hefferan T, Larson D, et al. Biological activity of rhBMP-2 released from PLGA microspheres. Journal of biomechanical engineering. 2000;122(3):289-92.

132. Damien CJ, Parsons JR, Prewett AB, Rietveld DC, Zimmerman MC. Investigation of an organic delivery system for demineralized bone matrix in a delayed‐healing cranial defect model. Journal of biomedical materials research. 1994;28(5):553-61.

133. Sheridan M, Shea L, Peters M, Mooney D. Bioabsorbable polymer scaffolds for tissue engineering capable of sustained growth factor delivery. Journal of Controlled Release. 2000;64(1):91-102.

134. Simon JL. Investigation into the Effects of Scaffold Architecture and Material Surface Texture on Bone Ingrowth: Rutgers University; 2004.

135. Saito N, Takaoka K. New synthetic biodegradable polymers as BMP carriers for bone tissue engineering. Biomaterials. 2003;24(13):2287-93.

136. Barralet J, Grover L, Gaunt T, Wright A, Gibson I. Preparation of macroporous calcium phosphate cement tissue engineering scaffold. Biomaterials. 2002;23(15):3063-72.

137. Karp JM, Rzeszutek K, Shoichet MS, Davies JE. Fabrication of precise cylindrical three-dimensional tissue engineering scaffolds for in vitro and in vivo bone engineering applications. Journal of Craniofacial Surgery. 2003;14(3):317-23.

138. Boontheekul T, Mooney DJ. Protein-based signaling systems in tissue engineering. Current Opinion in Biotechnology. 2003;14(5):559-65.

139. Kempen DH, Creemers LB, Alblas J, Lu L, Verbout AJ, Yaszemski MJ, et al. Growth factor interactions in bone regeneration. Tissue Engineering Part B: Reviews. 2010;16(6):551-66.

140. Kofron MD, Laurencin CT. Bone tissue engineering by gene delivery. Advanced drug delivery reviews. 2006;58(4):555-76.

141. Gaasbeek A, Meinders AE. Hypophosphatemia: an update on its etiology and treatment. The American journal of medicine. 2005;118(10):1094-101.

142. Razzaque MS. The FGF23–Klotho axis: endocrine regulation of phosphate homeostasis. Nature Reviews Endocrinology. 2009;5(11):611-9.

143. Iotti S, Lodi R, Gottardi G, Zaniol P, Barbiroli B. Inorganic Phosphate Is Transported into Mitochondria in the Absence of ATP Biosynthesis: Anin Vivo 31 P NMR Study in the Human Skeletal Muscle. Biochemical and biophysical research communications. 1996;225(1):191-4.

144. Hutson SM, Williams GD, Berkich DA, LaNoue KF, Briggs RW. A phosphorus-31 NMR study of mitochondrial inorganic phosphate visibility: effects of calcium (2+) and manganese (2+) and the pH gradient. Biochemistry. 1992;31(5):1322-30.

145. Razzaque M. Phosphate toxicity: new insights into an old problem. Clinical science. 2011;120:91-7.

146. Fukagawa M, Hamada Y, Nakanishi S, Tanaka M. The kidney and bone metabolism: Nephrologists' point of view. Journal of bone and mineral metabolism. 2006;24(6):434-8.

147. Razzaque MS. Therapeutic potential of klotho-FGF23 fusion polypeptides: WO2009095372. Expert opinion on therapeutic patents. 2010;20(7):981-5.

148. Dorozhkin SV. Biocomposites and hybrid biomaterials based on calcium orthophosphates. Biomatter. 2011;1(1):3-56.

149. Dorozhkin S. Calcium orthophosphates in nature, biology and medicine. Materials 2009; 2: 399-498. Caracterización preclínica de las espumas de hidroxiapatita autofraguables in situ. 297:300.

150. Marraffa JM, Hui A, Stork CM. Severe hyperphosphatemia and hypocalcemia following the rectal administration of a phosphate-containing Fleet® pediatric enema. Pediatric emergency care. 2004;20(7):453-6.

151. Martin RR, Lisehora GR, Braxton M, Barcia PJ. Fatal poisoning from sodium phosphate enema: case report and experimental study. Jama. 1987;257(16):2190-2.

152. Heinonen JK, Lahti RJ. A new and convenient colorimetric determination of inorganic orthophosphate and its application to the assay of inorganic pyrophosphatase. Analytical biochemistry. 1981;113(2):313-7.

153. Chen J, Xu L, Chen S, Yang J, Jiang H. Transcriptional regulation of platelet-derived growth factor-B chain by thrombin in endothelial cells: involvement of Egr-1 and CREB-binding protein. Molecular and cellular biochemistry. 2012;366(1-2):81-7.

154. Sweet L, Kang Y, Czisch C, Witek L, Shi Y, Smay J, et al. Geometrical versus Random β-TCP Scaffolds: Exploring the Effects on Schwann Cell Growth and Behavior. PloS one. 2015;10(10):e0139820.

155. Livak KJ, Schmittgen TD. Analysis of relative gene expression data using real-time quantitative PCR and the 2− ΔΔCT method. methods. 2001;25(4):402-8.

156. Schneider CA, Rasband WS, Eliceiri KW. NIH Image to ImageJ: 25 years of image analysis. Nature methods. 2012;9(7):671-5.

157. Rueb C, Zukoski C. Viscoelastic properties of colloidal gels. Journal of Rheology (1978-present). 1997;41(2):197-218.

158. Ramirez AG, Sinclair R, Harkins CG, Lin AR. The effects of slider material on the gasification of carbon. Journal of tribology. 2002;124(4):771-4.

159. Miano F, Bailey A, Luckham PF, Tadros TF. Adsorption of nonyl phenol propylene oxide—ethylene oxide surfactants on carbon black and the rheology of the resulting dispersions. Colloids and Surfaces. 1992;62(1–2):111-8. doi: http://dx.doi.org/10.1016/0166-6622(92)80042-Z.

160. Rueb CJ, Zukoski CF. Viscoelastic properties of colloidal gels. J Rheol. 1997;41(2):197-218. PubMed PMID: ISI:A1997WL62600002.

APPENDIX A CIRCULAR SCAFFOLD

```
;<HEAD>

;MultiTip=False

;<Syringe0Properties>, skip

;syringe diam = 9.54, skip

;backoff dist = 1.3, skip

;Tip diam = 0.33, skip

;Tip pos = (-13.752, 3.331, -8.964), skip

#define v0 SY0Speed

#define v10 SY0Stroke

#define v11 T0X

#define v12 T0Y

#define v13 T0Z

;</Syringe0Properties>;skip

;<Syringe1Properties>, skip

;syringe diam = 9.59, skip

;backoff dist = 1, skip

;Tip diam = 0.33, skip
```

```
;Tip pos = (-44.05, 3.48, -8.945), skip

#define v1 SY1Speed

#define v20 SY1Stroke

#define v21 T1X

#define v22 T1Y

#define v23 T1Z

;</Syringe1Properties>;skip

;<Syringe2Properties>, skip

;syringe diam = 9.59, skip

;backoff dist = 2, skip

;Tip diam = 0.33, skip

;Tip pos = (0, 0, 0), skip

#define v2 SY2Speed

#define v30 SY2Stroke

#define v31 T2X

#define v32 T2Y

#define v33 T2Z

;</Syringe2Properties>;skip

;Define variables for tip change motion

#define v1 TM0

#define v2 TM1

#define v3 TM2

BO1;

PL1; PLANE 1 is motion plane
```

```
PR ME UN UN/SE;

VELOCITY OFF;

CM0; Modal, contour mode 0

AC PL=300; Limit accel per plane to 300 mm/s^2

RA 50; Set accel time to 50 ms

EN X Y Z U;

EN A;

EN C;

ER A,0,0; Turn off Error checking on stepper

ER C,0,0; Turn off Error checking on stepper

BO 2; setup board 2

PR ME UN UN/SE;

RA 50; Set accel time to 50 ms

EN X Z;

BO 1;

;<Tip0da_Position>

T0X = -13.752

T0Y = 3.331

T0Z = -8.964

;</Tip0da_Position>

;<Tip1da_Position>

T1X = -44.05
```

```
T1Y = 3.48

T1Z = -8.945

;</Tip1da_Position>

;<Tip2da_Position>

T2X = 0

T2Y = 0

T2Z = 0

;</Tip2da_Position>

;</HEAD>

;<BODY>

;Initial Point=(0.247399, -4.993876, 0)

;Initial Speed=10

;<Layer 0>

;<Ink On> skip

        ;COMP=(1, 0, 0, 0, 0, 0)

        ;Print Length= 156.137931 skip

        ;Write Speed= 10 skip

        SU :SY0PlungerDown ; skip

        SY0Speed = 0.011966; skip

        SY0Stroke = -0.185248; skip

        SU :SY0Start ; skip

;</End Ink On> skip
```

CCW X-0.247398 Y-0.006124 I-0.247399 J4.993876 F10;

LI X-0.000001 Y0.2508 Z0 F10; (SMALL CONN LINE)

CCW X4.7492 Y4.7492 I0 J4.7492 F10;

;<Filled Arc: ToCenter=(-4.7492, 0, 0), ToEnd=(-9.4984, 0, 0), d_InRad=0, n_Dir=1, Speed=10, [FillOptions: FillType=Raster, FillDir=In, FillPeriodicity=Uniform, WindingDir=CCW, RW=0.6785, SpaceInCenter=False]>

VELOCITY ON; skip

CCW X-0.678457 Y2.446212 I-4.7492 J0 F10;

LI X0 Y-4.892424 Z0 F10;

CW X-0.678456 Y-0.877535 I-4.070743 J2.446212 F10;

LI X0 Y6.647495 Z0 F10;

CCW X-0.678456 Y0.573691 I-3.392286 J-3.323748 F10;

LI X0 Y-7.794879 Z0 F10;

CW X-0.678455 Y-0.393499 I-2.713829 J3.89744 F10;

LI X0 Y8.581879 Z0 F10;

CCW X-0.678459 Y0.26029 I-2.035371 J-4.29094 F10;

LI X0 Y-9.102458 Z0 F10;

CW X-0.678459 Y-0.14926 I-1.356914 J4.551229 F10;

LI X0 Y9.400978 Z0 F10;

CCW X-0.678458 Y0.048711 I-0.678457 J-4.700489 F10;

LI X0 Y-9.4984 Z0 F10;

CW X-0.678457 Y0.048711 I0 J4.7492 F10;

LI X0 Y9.400978 Z0 F10;

```
                CCW X-0.678456 Y-0.14926 I0.678457 J-4.700489 F10;

                LI X0 Y-9.102458 Z0 F10;

                CW X-0.678456 Y0.260289 I1.356914 J4.551229 F10;

                LI X0 Y8.581879 Z0 F10;

                CCW X-0.678455 Y-0.393499 I2.035371 J-4.29094 F10;

                LI X0 Y-7.794879 Z0 F10;

                CW X-0.678459 Y0.573694 I2.713829 J3.89744 F10;

                LI X0 Y6.647495 Z0 F10;

                CCW X-0.678458 Y-0.877537 I3.392286 J-3.323748 F10;

                LI X0 Y-4.892424 Z0 F10;

                VELOCITY OFF; skip

                CW X-0.678457 Y2.446213 I4.070743 J2.446212 F10;

        ;</End Filled Arc>

;</End Layer 0>

;<Layer 1>

;<Ink On> skip

        ;COMP=(1, 0, 0, 0, 0, 0)

        ;Print Length= 156.571817 skip

        ;Write Speed= 10 skip

        SY0Speed = 0.011966; skip

        SY0Stroke = -0.185767; skip

        SU :SY0Start ; skip
```

;</End Ink On> skip

LI X-0.244676 Y-0.247399 Z0.2592 F10; (SMALL CONN LINE)

CCW X-0.006124 Y0.247386 I4.993876 J0.247399 F10;

LI X0.2508 Y0.000013 Z0 F10; (SMALL CONN LINE)

CCW X4.7492 Y-4.7492 I4.7492 J0 F10;

;<Filled Arc: ToCenter=(0, 4.7492, 0), ToEnd=(0, 9.4984, 0), d_InRad=0, n_Dir=1, Speed=10, [FillOptions: FillType=Raster, FillDir=In, FillPeriodicity=Uniform, WindingDir=CCW, RW=0.6785, SpaceInCenter=False]>

VELOCITY ON; skip

CCW X2.446212 Y0.678457 I0 J4.7492 F10;

LI X-4.892424 Y0 Z0 F10;

CW X-0.877537 Y0.678458 I2.446212 J4.070743 F10;

LI X6.647495 Y0 Z0 F10;

CCW X0.573691 Y0.678456 I-3.323748 J3.392286 F10;

LI X-7.794879 Y0 Z0 F10;

CW X-0.393501 Y0.678459 I3.89744 J2.713829 F10;

LI X8.581879 Y0 Z0 F10;

CCW X0.260289 Y0.678458 I-4.29094 J2.035371 F10;

LI X-9.102458 Y0 Z0 F10;

CW X-0.14926 Y0.67846 I4.551229 J1.356914 F10;

LI X9.400978 Y0 Z0 F10;

CCW X0.048711 Y0.678447 I-4.700489 J0.678457 F10;

LI X-9.4984 Y0 Z0 F10;

```
                CW X0.048711 Y0.678457 I4.7492 J0 F10;
                LI X9.400978 Y0 Z0 F10;
                CCW X-0.149263 Y0.678467 I-4.700489 J-0.678457 F10;
                LI X-9.102458 Y0 Z0 F10;
                CW X0.260288 Y0.678455 I4.551229 J-1.356914 F10;
                LI X8.581879 Y0 Z0 F10;
                CCW X-0.3935 Y0.678456 I-4.29094 J-2.035371 F10;
                LI X-7.794879 Y0 Z0 F10;
                CW X0.573691 Y0.678456 I3.89744 J-2.713829 F10;
                LI X6.647495 Y0 Z0 F10;
                CCW X-0.877537 Y0.678458 I-3.323748 J-3.392286 F10;
                LI X-4.892424 Y0 Z0 F10;
                VELOCITY OFF; skip
                CW X2.446211 Y0.678457 I2.446212 J-4.070743 F10;
        ;</End Filled Arc>
;</End Layer 1>
;<Layer 2>
;<Ink On> skip
        ;COMP=(1, 0, 0, 0, 0, 0)
        ;Print Length= 156.571817 skip
        ;Write Speed= 10 skip
        SY0Speed = 0.011966; skip
```

SY0Stroke = -0.185767; skip

SU :SY0Start ; skip

;</End Ink On> skip

LI X-0.247399 Y0.244676 Z0.2592 F10; (SMALL CONN LINE)

CCW X0.247398 Y0.006124 I0.247399 J-4.993876 F10;

LI X0.000001 Y-0.2508 Z0 F10; (SMALL CONN LINE)

CCW X-4.7492 Y-4.7492 I0 J-4.7492 F10;

;<Filled Arc: ToCenter=(4.7492, 0, 0), ToEnd=(9.4984, 0, 0), d_InRad=0, n_Dir=1, Speed=10, [FillOptions: FillType=Raster, FillDir=In, FillPeriodicity=Uniform, WindingDir=CCW, RW=0.6785, SpaceInCenter=False]>

VELOCITY ON; skip

CCW X0.678457 Y-2.446212 I4.7492 J0 F10;

LI X0 Y4.892424 Z0 F10;

CW X0.678456 Y0.877535 I4.070743 J-2.446212 F10;

LI X0 Y-6.647495 Z0 F10;

CCW X0.678456 Y-0.573691 I3.392286 J3.323748 F10;

LI X0 Y7.794879 Z0 F10;

CW X0.678455 Y0.393499 I2.713829 J-3.89744 F10;

LI X0 Y-8.581879 Z0 F10;

CCW X0.678459 Y-0.26029 I2.035371 J4.29094 F10;

LI X0 Y9.102458 Z0 F10;

CW X0.678459 Y0.14926 I1.356914 J-4.551229 F10;

LI X0 Y-9.400978 Z0 F10;

```
                CCW X0.678458 Y-0.048711 I0.678457 J4.700489 F10;
                LI X0 Y9.4984 Z0 F10;
                CW X0.678457 Y-0.048711 I0 J-4.7492 F10;
                LI X0 Y-9.400978 Z0 F10;
                CCW X0.678456 Y0.14926 I-0.678457 J4.700489 F10;
                LI X0 Y9.102458 Z0 F10;
                CW X0.678456 Y-0.260289 I-1.356914 J-4.551229 F10;
                LI X0 Y-8.581879 Z0 F10;
                CCW X0.678455 Y0.393499 I-2.035371 J4.29094 F10;
                LI X0 Y7.794879 Z0 F10;
                CW X0.678459 Y-0.573694 I-2.713829 J-3.89744 F10;
                LI X0 Y-6.647495 Z0 F10;
                CCW X0.678458 Y0.877537 I-3.392286 J3.323748 F10;
                LI X0 Y4.892424 Z0 F10;
                VELOCITY OFF; skip
                CW X0.678457 Y-2.446213 I-4.070743 J-2.446212 F10;
        ;</End Filled Arc>
;</End Layer 2>
;<Layer 3>
;<Ink On> skip
        ;COMP=(1, 0, 0, 0, 0, 0)
        ;Print Length= 156.571817 skip
```

;Write Speed= 10 skip

SY0Speed = 0.011966; skip

SY0Stroke = -0.185767; skip

SU :SY0Start ; skip

;</End Ink On> skip

LI X0.244676 Y0.247399 Z0.2592 F10; (SMALL CONN LINE)

CCW X0.006124 Y-0.247386 I-4.993876 J-0.247399 F10;

LI X-0.2508 Y-0.000013 Z0 F10; (SMALL CONN LINE)

CCW X-4.7492 Y4.7492 I-4.7492 J0 F10;

;<Filled Arc: ToCenter=(0, -4.7492, 0), ToEnd=(0, -9.4984, 0), d_InRad=0, n_Dir=1, Speed=10, [FillOptions: FillType=Raster, FillDir=In, FillPeriodicity=Uniform, WindingDir=CCW, RW=0.6785, SpaceInCenter=False]>

VELOCITY ON; skip

CCW X-2.446212 Y-0.678457 I0 J-4.7492 F10;

LI X4.892424 Y0 Z0 F10;

CW X0.877537 Y-0.678458 I-2.446212 J-4.070743 F10;

LI X-6.647495 Y0 Z0 F10;

CCW X-0.573691 Y-0.678456 I3.323748 J-3.392286 F10;

LI X7.794879 Y0 Z0 F10;

CW X0.393501 Y-0.678459 I-3.89744 J-2.713829 F10;

LI X-8.581879 Y0 Z0 F10;

CCW X-0.260289 Y-0.678458 I4.29094 J-2.035371 F10;

LI X9.102458 Y0 Z0 F10;

```
                CW X0.14926 Y-0.67846 I-4.551229 J-1.356914 F10;
                LI X-9.400978 Y0 Z0 F10;
                CCW X-0.048711 Y-0.678447 I4.700489 J-0.678457 F10;
                LI X9.4984 Y0 Z0 F10;
                CW X-0.048711 Y-0.678457 I-4.7492 J0 F10;
                LI X-9.400978 Y0 Z0 F10;
                CCW X0.149263 Y-0.678467 I4.700489 J0.678457 F10;
                LI X9.102458 Y0 Z0 F10;
                CW X-0.260288 Y-0.678455 I-4.551229 J1.356914 F10;
                LI X-8.581879 Y0 Z0 F10;
                CCW X0.3935 Y-0.678456 I4.29094 J2.035371 F10;
                LI X7.794879 Y0 Z0 F10;
                CW X-0.573691 Y-0.678456 I-3.89744 J2.713829 F10;
                LI X-6.647495 Y0 Z0 F10;
                CCW X0.877537 Y-0.678458 I3.323748 J3.392286 F10;
                LI X4.892424 Y0 Z0 F10;
                VELOCITY OFF; skip
                CW X-2.446211 Y-0.678457 I-2.446212 J4.070743 F10;
        ;</End Filled Arc>
;</End Layer 3>
;<Layer 4>
;<Ink On> skip
```

;COMP=(1, 0, 0, 0, 0, 0)

;Print Length= 156.571817 skip

;Write Speed= 10 skip

SY0Speed = 0.011966; skip

SY0Stroke = -0.185767; skip

SU :SY0Start ; skip

;</End Ink On> skip

LI X0.247399 Y-0.244676 Z0.2592 F10; (SMALL CONN LINE)

CCW X-0.247398 Y-0.006124 I-0.247399 J4.993876 F10;

LI X-0.000001 Y0.2508 Z0 F10; (SMALL CONN LINE)

CCW X4.7492 Y4.7492 I0 J4.7492 F10;

;<Filled Arc: ToCenter=(-4.7492, 0, 0), ToEnd=(-9.4984, 0, 0), d_InRad=0, n_Dir=1, Speed=10, [FillOptions: FillType=Raster, FillDir=In, FillPeriodicity=Uniform, WindingDir=CCW, RW=0.6785, SpaceInCenter=False]>

VELOCITY ON; skip

CCW X-0.678457 Y2.446212 I-4.7492 J0 F10;

LI X0 Y-4.892424 Z0 F10;

CW X-0.678456 Y-0.877535 I-4.070743 J2.446212 F10;

LI X0 Y6.647495 Z0 F10;

CCW X-0.678456 Y0.573691 I-3.392286 J-3.323748 F10;

LI X0 Y-7.794879 Z0 F10;

CW X-0.678455 Y-0.393499 I-2.713829 J3.89744 F10;

LI X0 Y8.581879 Z0 F10;

CCW X-0.678459 Y0.26029 I-2.035371 J-4.29094 F10;

LI X0 Y-9.102458 Z0 F10;

CW X-0.678459 Y-0.14926 I-1.356914 J4.551229 F10;

LI X0 Y9.400978 Z0 F10;

CCW X-0.678458 Y0.048711 I-0.678457 J-4.700489 F10;

LI X0 Y-9.4984 Z0 F10;

CW X-0.678457 Y0.048711 I0 J4.7492 F10;

LI X0 Y9.400978 Z0 F10;

CCW X-0.678456 Y-0.14926 I0.678457 J-4.700489 F10;

LI X0 Y-9.102458 Z0 F10;

CW X-0.678456 Y0.260289 I1.356914 J4.551229 F10;

LI X0 Y8.581879 Z0 F10;

CCW X-0.678455 Y-0.393499 I2.035371 J-4.29094 F10;

LI X0 Y-7.794879 Z0 F10;

CW X-0.678459 Y0.573694 I2.713829 J3.89744 F10;

LI X0 Y6.647495 Z0 F10;

CCW X-0.678458 Y-0.877537 I3.392286 J-3.323748 F10;

LI X0 Y-4.892424 Z0 F10;

VELOCITY OFF; skip

CW X-0.678457 Y2.446213 I4.070743 J2.446212 F10;

;</End Filled Arc>

;</End Layer 4>

SU :SY0Stop ; skip

SU :SY1Stop ; skip

SU :SY2Stop ; skip

SU :SY0PlungerUp ; skip

M2; signals the end of the program.

;</BODY>

;<TAIL>

:SY0PlungerDown

WA ON; skip

LI U-1.3 F25; skip

WA ON; skip

DW 10; skip

RETURN

:SY0PlungerUp

WA ON; skip

LI U1.3 F25; skip

WA ON; skip

RETURN

:SY0Start

PL 2

LI U SY0Stroke F

SY0Speed ;skip

```
PL 1

RETURN

:SY0Stop

WA ON; skip

FR U0; skip

RETURN

:SY1PlungerDown

WA ON; skip

BO 2; skip

LI X-1 F10; skip

WA ON; skip

BO 1; skip

RETURN

:SY1PlungerUp

WA ON; skip

BO 2; skip

LI X1 F10; skip

WA ON; skip

BO 1; skip

RETURN

:SY1Start

BO 2; skip
```

```
PL 2

LI X SY1Stroke F

SY1Speed ;skip

BO 1; skip

PL 1

RETURN

:SY1Stop

WA ON; skip

BO 2; skip

FR X0; skip

BO 1; skip

RETURN

:SY2PlungerDown

WA ON; skip

BO 2; skip

LI Z-2 F30; skip

WA ON; skip

BO 1; skip

RETURN

:SY2PlungerUp

WA ON; skip

BO 2; skip
```

```
LI Z2 F30; skip

WA ON; skip

BO 1; skip

RETURN

:SY2Start

BO 2; skip

PL 2

LI Z SY2Stroke F

SY2Speed ;skip

BO 1; skip

PL 1

RETURN

:SY2Stop

WA ON; skip

BO 2; skip

FR Z0; skip

BO 1; skip

RETURN

;</TAIL>
```

APPENDIX B SHRINKAGE

The scaffolds were placed in a desiccator for a 24-hour period before being placed into the high temperature furnace electric furnace (Model LHT 02/17, Nabertherm GmbH, Lilienthal, Germany). The furnace was programmed for three different firing protocols with maximum sintering temperatures of 900°C, 1100°C, and 1250°C for 4 hours. Shrinkage due to sintering was measured by means of micro calipers (Mitutoyo, Tokyo, Japan) for each rod at pre- and post-sintering conditions (n=10 per group). The cylinder formula

$$V=\pi \cdot r^2 \cdot h \tag{B.1}$$

where, V is the volume, r the radius, and h the height of the scaffold was used to calculate the pre- and post-sintering volume. Scaffold volume was calculated, pre and post sintering, using two different methods: (1) using microcalipers (Coolant Proof IP66, Mitutoyo America Corporation, IL, USA) and (2) Archimedes' method. For the later method the samples were weighed in air and subsequently in a liquid medium (EtOH), and derived using the following formula, where the correction factor for apparatus, α, was equal to 0.99985:

$$Vol=\alpha\left(\frac{W_{air}-W_{liquid}}{\rho_{air}-\rho_{liquid}}\right) \tag{B.2}.$$

The pre- and post-sintering volumes were utilized to calculate the shrinkage percentage as:

$$\text{Percent Shrinkage} = \frac{(Vol_{\text{Green State}})-(Vol_{\text{Sintered}})}{(Vol_{\text{Green State}})} \tag{B.3}.$$

Statistical analysis showed that both calcination and sintering temperatures presented a significant effect on shrinkage (both $p<0.001$) (Table B.1 and Figure B.1). Significantly higher shrinkage (mean ± 95% confidence interval) was observed for scaffolds made of materials calcined at 975°C (18.58% ± 1.00) relative to 800°C (14.96% ± 1.05). Concerning the different sintering temperatures, scaffolds sintered to 1100°C presented significantly higher shrinkage

relative to the ones sintered to 900°C and 1250°C at values of 22.25% ± 1.44, 14.48% ± 1.3, and 13.58% ± 1.3, respectively.

Calcination Temp. ➔	800°C			975°C		
Sintering Temp. ⬇	Mean	Lower Limit	Upper Limit	Mean	Lower Limit	Upper Limit
900°C	13.87[b]	11.32	16.42	15.20[b]	12.91	17.49
1100°C	20.01[a,b]	16.91	23.11	24.38[a]	20.16	28.60
1250°C	11.12[c]	9.51	12.73	16.11[b]	13.90	18.32

Table B.1: Percent shrinkage means ± 95% confidence interval for the different groups. The letters

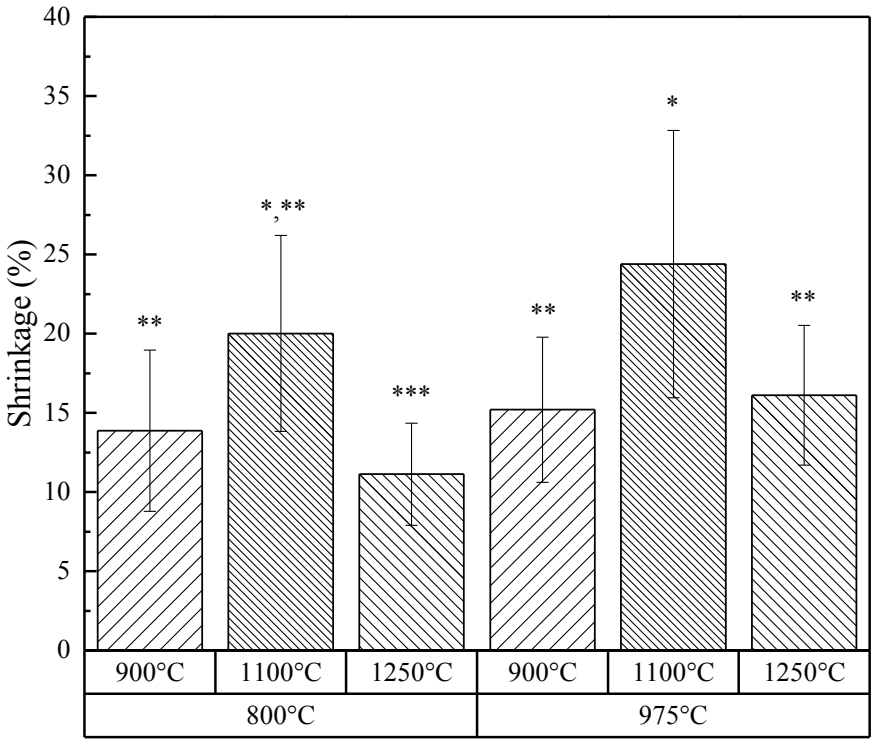

Figure B.1: Percent shrinkage means ± 95% confidence interval for the different groups. The number of asterisks depicts statistically homogeneous groups.

APPENDIX C RADIAL DISTRUTION FUNCTION

```
macro "Radial Distribution Function [f5]" {

	run("Select None");

	doStack=false;

	//User dialog

	Dialog.create('RDF Options');

	Dialog.setInsets(0,0,0)

	Dialog.addMessage("Radial Distribution Function Macro \nby Michael Schmid & Ajay Gopal \n(v.2011-08-21)");

	if (nSlices()>1) {

		Dialog.addMessage("Selected file is a stack. \nUncheck below to analyze \nonly the current slice.");

		Dialog.addCheckbox("Use all slices in stack?", true);

	}

	Dialog.addMessage("Particle Detection Noise Threshold \nHint: test image/s first with \nImageJ>Process>Find Maxima \nto verify that below threshold \ngives accurate particle centers.");

	Dialog.addNumber("Noise Threshold", 10);

	Dialog.addMessage("Default output is RDF plot with \noptions to list, save & copy data. \nCheck below to output extra \nwindow with RDF data table.");

	Dialog.addCheckbox("Output RDF data table ", false);
```

```
Dialog.show;
        //Preliminary checks
        if (nSlices()>1) doStack _ Dialog.getCheckbox;
        noiseThr = Dialog.getNumber;
        showList = Dialog.getCheckbox;
        setBatchMode(true);
        firstSlice=getSliceNumber();
        lastSlice=getSliceNumber();
        if (doStack) {
                firstSlice=1;
                lastSlice=nSlices();
        }
        width=getWidth;
        height=getHeight;
        //maxRadius may be modified, should not be larger than 0.3*minOf(width, height);
        maxRadius=0.3*minOf(width, height);
        minFFTsize=1.3*maxOf(width, height);
        title=getTitle();
        size=4;
        while(size<minFFTsize) size*=2;
        //Main processing loop
        for (slice=firstSlice; slice<=lastSlice; slice++) {
```

```
//Make autocorrelation of particle positions
if (doStack) setSlice(slice);
run("Find Maxima...", "noise="+noiseThr+" output=[Single Points] light exclude");
tempID=getImageID();
tempTitle="temp-"+random();
rename(tempTitle);
run("Canvas Size...", "width="+ size+" height="+ size+" position=Center zero");
run("FD Math...", "image1=["+tempTitle+"] operation=Correlate image2=["+tempTitle+"] result=AutoCorrelation do");
psID=getImageID();
selectImage(tempID);
close();
//Make autocorrelation reference to correct finite image size effects
newImage("frame", "8-bit White", width, height, 1);
run("Set...", "value=255");
tempID=getImageID();
rename(tempTitle);
run("Canvas Size...", "width="+ size+" height="+ size+" position=Center zero");
run("FD Math...", "image1=["+tempTitle+"] operation=Correlate image2=["+tempTitle+"] result=AutoCorrReference do");
refID=getImageID();
imageCalculator("Divide", psID,refID);
```

```
selectImage(refID);

close();

selectImage(tempID);

close();

//Prepare normalized power spectrum for radial averaging

selectImage(psID);

makeRectangle(size/2, size/2, 1, 1);

run("Set...", "value=0");

run("Select None");

circleSize=2*floor(maxRadius)+1;

run("Specify...", "width="+circleSize+" height="+circleSize+" x="+(size/2+0.5)+" y="+(size/2+0.5)+" oval centered");

getRawStatistics(nPixels, mean);

run("Select None");

run("Divide...", "value="+mean);

run("Specify...", "width="+circleSize+" height="+circleSize+" x="+(size/2+0.5)+" y="+(size/2+0.5)+" oval centered");

run("Radial Profile", "x="+(size/2+0.5)+" y="+(size/2+0.5)+" radius="+floor(maxRadius)-1);

rename("RDF of "+title);

rdfID=getImageID();

selectImage(psID);

close();
```

```
		//Averaging of RDFs for stacks
		if (doStack) {
			selectImage(rdfID);
			Plot.getValues(x, y);
			if (slice==firstSlice) ySum = newArray(y.length);
			for (i=0; i<y.length; i++)
			ySum[i]+ = y[i] / lastSlice;
			close();
		}
}//End Processing Loop


//Create output plots with annotated titles and options
if (doStack) {
		Plot.create("RDF of "+title+" (stack)", "Distance (pixels)", "RDF", x, ySum);
		if (showList) {
			run("Clear Results");
			for (i=0; i<x.length; i++) {
				setResult("R", i, x[i]);
				setResult("RDF", i, ySum[i]);
			}
			updateResults();
		}
```

```
        }
        else {
                selectImage(rdfID);
                Plot.getValues(x, y);
               Plot.create("RDF of "+title+" (slice"+lastSlice+")", "Distance (pixels)", "RDF", x,
y);
                if (showList) {
                        run("Clear Results");
                        for (i=0; i<x.length; i++) {
                                setResult("R", i, x[i]);
                                setResult("RDF", i, y[i]);
                        }
                        updateResults();
                }
                close();
        }//End Output
        setBatchMode("exit and display");// Comment this out if you get duplicate RDF outputs
} //End Macro
```

APPENDIX D CARBON BLACK OPTIMIZATION

Dispersion of carbon black (CB) powder and its rheological behaviors have been extensively studied in organic solvents and polymer melts. Rheological properties of aqueous carbon black dispersions have been investigated to a lesser extent; typically, with surfactants composed of hydrophobic anchoring groups and stabilizing polymeric chains [159]. The concentration of the colloidal gels used in this study is well above what has previously been reported in the literature for aqueous processing. The materials involved are commercially available and easily obtained at low cost.

The carbon black gel (CBG) formulation used an anionic dispersant in combination with a cationic flocculant molecule to control gel strength. Carbon black (CB) (Monarch 120, Cabot Corporation, Billerica, MA) with manufacturer specified particle density in the range of 1.8 g/cm^3 and specific surface area of 31.25 m^2/g, was selected for the particulate phase and was used without modification.

For fabrication of the CBG, sulfonated naphthalene condensate, ammonium salt (NSC4AL) (AGNIQUE NSC4AL, Cognis, Cincinnati, OH), a 44% by weight of an ammonium neutralized derivative of sulfonic acid, containing a naphthalene functional unit, is used as an ionic dispersant to stabilize carbon black in water. Nonlinear poly(ethylenimine) (ICN Biomedical, Aurora, OH) with M_w = 50 to 100 kDa ($PEI_{50\sim100K}$) is prepared in aqueous stock solutions with 10% by weight polymer and is used as a flocculent. While the DI water had a nominal conductivity 5×10^{-4} $(\Omega\cdot cm)^{-1}$.

To determine an ideal CBG formulation two series were fabricated. The 'A series' gel did not incorporate the flocculent, cationic polyelectrolyte, poly(ethylenimine) (PEI). 'A series' varied the weight % of the viscosifier, polyethylene glycol (PEG), with [PEG] = 0%, 2%, 6%, and 10%. While the 'B Series' kept the [PEG] constant at 5%, the $M_{[PEI]}/M_{[NSC]}$, was varied, in 0.1 increments, such that the ratios tested were 0.7, 0.8, and 0.9.

The initial dispersion, 'A series', of CBG, has a relatively low viscosity and this behavior is evident in comparison to the 'B series' where the flocculent, PEI, is a component.

Figure D.1(a) shows the oscillatory and steady flow behavior of the 'A series' CBG, comparing the 4 varying amounts of [PEG]. In Figure D.1(a), the elastic modulus (G') is graphed as a function of applied shear stress (τ_y) for each of the four groups. The magnitude of G' for the A2 and A3 materials were comparable to each other, whereas the A0 CBG was significantly lower across the entire stress amplitude range. The A1 CBG was slightly lower than A2 and A3 but significantly greater than the A0 CBG which at no [PEG] and PEI. Three parameters were used for comparison of the data: the plateau eleastic shear modulus (G'_{eq}) is representative of the elastic nature of the colloidal gel network prior to rupture of the gel, the yield stress (τ_y) defined as the stress amplitude where G'/G'_{eq} =0.9 and the yield strain (γ_y) defined as the strain amplitude when G'/G'_{eq} =0.9 [160]. The G'/G'_{eq} was a more accurate representation of the process happening in robocasting where the CBG goes from rest in a reservoir and is extruded through a tip. These parameters with corresponding values are reported in Table D.1. The yield stress in the 'A series' increases when the amount [PEG] is increased from 2% to 6%, but when increasing the [PEG] to 10% a slight decrease is observed in the yield stress (Figure C.1(b)). After analyzing the 'A series' data, the ideal amount of [PEG] was chosen to be 5%, and for the 'B series' the [PEG] was held constant while the $M_{[PEI]}/M_{[NSC]}$ ratio was varied ([PEI]/[NSC] = 0.7, 0.8, 0.9 for B1, B2, and B3 respectively). As can be seen in Figure D.2(a) and Table D.1, the carbon black samples A2 and B1 not only have similar yield stress values (τ_y) but elastic shear modulus (G'_{eq}) values. When comparing the 'A series' the similarity only is between A1-A3 and B1, the other two CBGs, B2 and B3, have values have properties an order of magnitude greater. Figure D.2(b) indicates the relation of the "B series' and the linear increase in shear stress (τ_y) when increasing the $M_{[PEI]}/M_{[NSC]}$ ratio. The final CBG formulation was based on the B3 values with a few modifications, with the results reported in 5.4.1 Rheological properties of CB gel found on page 101.

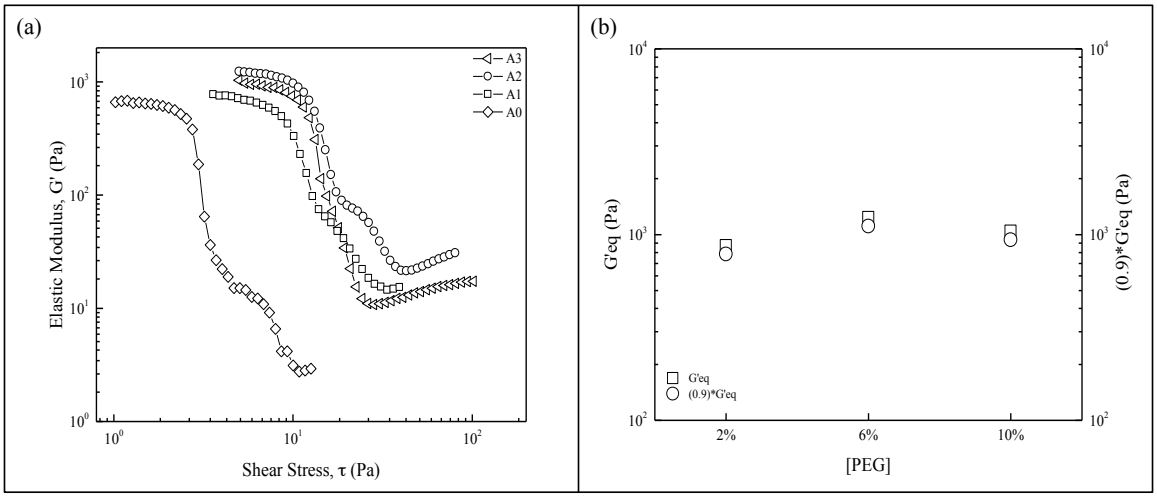

Figure D.1: (a) Rheology of 'A series' component CB gels, compared to each other with varying [PEG] amounts, describing the shear modulus as a function of shear stress. (b) Graph comparing the G'_{eq} and $0.9 \cdot G'_{eq}$, of the three 'A series' gels.

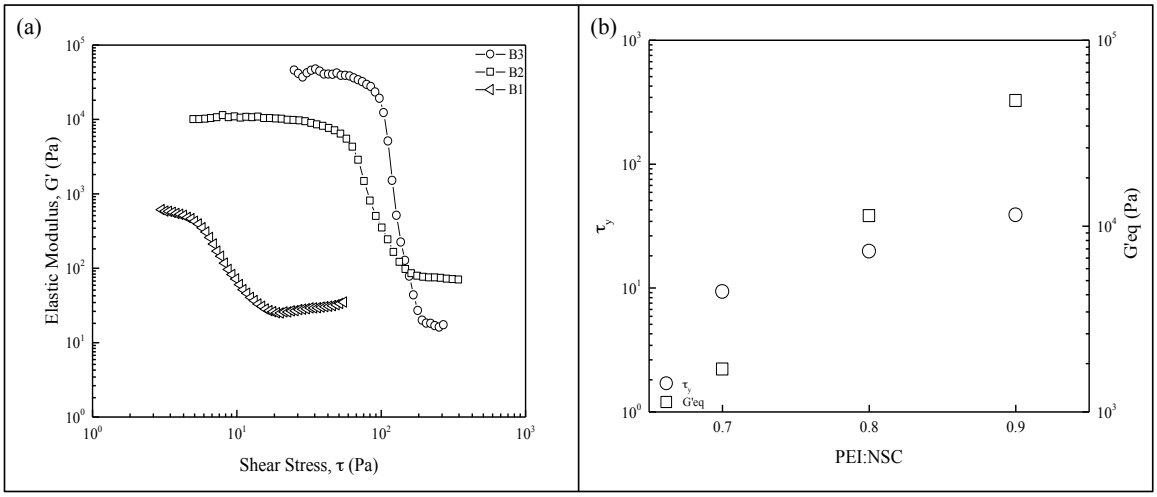

Figure D.2: (a) Rheology of 'B series' component CB gels, compared to each other with varying the ratio of $M_{[PEI]}/M_{[NSC]}$, amounts, describing the shear modulus as a function of shear stress. (b) Graph comparing the τ_y and G'_{eq}, of the three 'B series' gels.

Series	Sample	G'_{eq} (Pa)	$(0.9)G'_{eq}$ (Pa)	τ_y	[PEG]	$\frac{M_{[PEI]}}{M_{[NSC]}}$	ϕ_{solids}
A	1	871.0	783.9	2.81	2%	-	37.0%
	2	1233.0	1109.7	8.14	6%	-	37.0%
	3	1040.0	936.0	6.55	10%	-	37.0%
B	1	1697.9	1528.1	9.35	5%	0.7	37.0%
	2	11360.0	10224.0	19.74	5%	0.8	36.9%
	3	47303.0	42572.7	38.75	5%	0.9	36.9%

Table D.1: Summary of results interpreted from Figure D.1 and Figure D.2, giving numerical values to go along with graphical representations.

VITA

LUKASZ WITEK

Candidate for the Degree of

Doctor of Philosophy

Thesis: EXTRUSION-BASED, THREE-DIMENSIONAL PRINTING OF CALCIUM-PHOSPHATE SCAFFOLDS

Major Field: Chemical Engineering

Biographical:

Personal:
Born in Rome, Italy to Lucyna Witek and Tadeusz Witek on October 16, 1985. Accepted a Postdoctoral Research Associate position at New York University College of Dentistry in New York, New York beginning November 2, 2015.

Education:
Completed the requirements for the Doctor of Philosophy in Chemical Engineering at Oklahoma State University, Stillwater, Oklahoma in December 2015.

Completed the requirements for the Master of Science in Biomaterials and Biomimetics at New York University, New York, New York in January 2011.

Completed the requirements for the Bachelor of Science in Biology at Temple University, Philadelphia, Pennsylvania in August 2008.

Experience:
Research Assistant, School of Chemical Engineering, Oklahoma State University, Stillwater, Oklahoma: August 2011 – November 2015

Teaching Assistant, School of Materials Science and Engineering, Oklahoma State University, Tulsa, Oklahoma: August 2014 – May 2015

Teaching Assistant, School of Chemical Engineering, Oklahoma State University, Stillwater, Oklahoma: August 2008 – May 2014

Professional Memberships: Society for Biomaterials (SFB)
American Association for Dental Research (AADR)
International Association for Dental Research (IADR)